CONSTITUENT-SPECIFIC MODELING OF LEFT VENTRICLE AND URINARY BLADDER MECHANICAL BEHAVIOR

By

Marissa Rae Grobbel

A DISSERTATION

Submitted to
Michigan State University
in partial fulfillment of the requirements
for the degree of

Mechanical Engineering – Doctor of Philosophy

2021

ABSTRACT

CONSTITUENT-SPECIFIC MODELING OF LEFT VENTRICLE AND URINARY BLADDER MECHANICAL BEHAVIOR

By

Marissa Rae Grobbel

Most organs in the human body have a unique mechanical function, which depends on the pressures and forces exerted onto the organ, as well as its comprising tissues' composition and mechanical behavior. However, pathological conditions can cause inflammation, over-pressurization, or over-distension, resulting in remodeling of the tissues' constituents, such as cell hypertrophy or fibrosis, which in turn alters the mechanical behavior of the tissue and, ultimately, whole organ function. For this reason, it is crucial to understand the mechanical behavior of both healthy and pathologically remodeled biological tissues. The focus of this dissertation will be on developing constituent-specific, descriptive constitutive models for the left ventricle and urinary bladder under healthy and pathological conditions.

Many constitutive models have been proposed for soft tissues, including the left ventricle and the urinary bladder. These models include descriptions of the mechanical behavior of these tissues with regard to characteristics such as general non-linear behavior, fiber orientation and dispersion, and viscoelastic behavior, for both healthy and pathological conditions. Techniques for developing and validating these models typically include fitting the models' parameters to experimental data. The following chapters will focus on uniaxial data as well as opening angle tests, and an isotropic, exponential constitutive model. Additionally, a novel model for the left ventricle is introduced that includes a term that quantifies inter-constituent mechanical interaction.

Furthermore, this work aims to quantify the changes in soft tissues associated with pathology. As disease progresses in the left ventricle and urinary bladder, tissue remodeling can cause significant changes to the mechanical behavior, such as stiffening or softening of the organ walls—which can further progress disease, creating a positive feedback loop. In the left ventricle, hypertension has been studied in regard to mechanical behavior and composition of the tissue as well as residual

stress (via opening angle tests). However, no current studies have shown how these changes affected the constituents' individual mechanical behaviors and stress-states. In the urinary bladder, while some studies have focused on mechanical behavior of the remodeled type I diabetic bladder, no studies have reported whether these changes are consistent with type II diabetes. The pathologies of interest in the following chapters are: hypertension in the left ventricle, type II diabetes in the urinary bladder, and radiation cystitis in the urinary bladder (as this pathology has not been previously studied for its effect on bladder wall mechanical behavior).

The goals of this dissertation are to: (1) establish the need for a left ventricle constitutive model that includes a term for a mechanical inter-constituent interaction, (2) characterize the changes to the residual stress distribution of the isolated constituents in a hypertensive model of the left ventricle, (3) determine the effect of type II diabetes—both with and without the presence of obesity—on urinary bladder mechanical behavior, and (4) measure mechanical parameters and stiffness alterations to urinary bladder tissue that has undergone radiation treatment.

ACKNOWLEDGEMENTS

I would like to acknowledge my colleagues, friends, and family for their support during my PhD. First, I would like to thank my PhD advisor, Dr. Sara Roccabianca, for not only being the first to encourage me to attend graduate school, but for her continued mentorship throughout my undergraduate and PhD. I have become a better writer, researcher, student, and overall scientist thanks to her. I would also like to thank my committee members, Dr. Lik Chuan Lee, Dr. Christina Chan, and Dr. Tamara Reid Bush, for their collaborations and advice over the years. I would like to acknowledge my labmates (past and present) who have helped me work through problems, and I thank them for their continued friendship: Dr. Sheng Chen, Dr. Mayank Sinha, Dr. Tyler Tuttle, Eli Broemer, Laura Nye, Yuheng Wang, Manoj Ghosh, and Dillon McClintock.

I am also extremely thankful for my family, especially my parents, Steven and Robin Grobbel, for always believing in me and being encouraging of my aspirations. I also want to acknowledge my siblings Alex Grobbel and Brianne Bonifas, as well as their spouses Tracy and Blake, for always being there to support me. I would like to thank my sweet niece, Amelia, for being a constant source of joy in my life. I would also like to thank my boyfriend, Dr. Connor Boss, for always being supportive and understanding over the years, while we obtained our PhDs side-by-side.

TABLE OF CONTENTS

LIST O	F TABLES v	iii
LIST O	F FIGURES	ix
СНАРТ	ER 1 INTRODUCTION AND LITERATURE REVIEW	1
1.1	INTRODUCTION	1
1.2	LITERATURE REVIEW	3
	1.2.1 Anatomy and tissue composition	3
	1.2.2 Disease and remodeling	5
		7
1.3		11
СНАРТ	ER 2 CONTRIBUTION OF LEFT VENTRICULAR RESIDUAL STRESS BY	
	MYOCYTES AND COLLAGEN: EXISTENCE OF INTER-CONSTITUENT	
		14
2.1		14
		15
		16
		16
	2,	17
2.2	\boldsymbol{c}	24
		24
		- · 25
	•	26
2.3	1	31
		36
2.4		37
СНАРТ	ER 3 LEFT VENTRICULAR GEOMETRY, TISSUE COMPOSITION, AND	
		38
3.1	METHODS	38
	3.1.1 Sample preparation	
	1 1 1	39
		39
		39
		41
3.2	· · · · · · · · · · · · · · · · · · ·	44
		45
	C J	47
		49
2 2	· · · · · · · · · · · · · · · · · · ·	٠ ۲1

3.4	3.3.1 CON	Limitations
СНАРТ	FR 4	CHANGES IN BLADDER WALL MECHANICAL BEHAVIOR WITH
CIIAI I	LICT	TYPE II DIABETES
4.1	MET	HODS
4.1	4.1.1	
	4.1.1	1 1 1
	4.1.3	Mechanical testing
4.0	4.1.4	Constitutive modeling framework
4.2		JLTS
	4.2.1	Histology and microstructural analysis
	4.2.2	Mechanical testing
	4.2.3	Constitutive model parameters
4.3		SUSSION
	4.3.1	Limitations
4.4	CON	CLUSION
СНАРТ	TER 5	RADIATION CYSTITIS-INDUCED STIFFENING OF THE URINARY
		BLADDER
5.1	MET	HODS
	5.1.1	Bladder radiation treatment
	5.1.2	Void Spot Assay
	5.1.3	Tissue preparation
	5.1.4	Bladder ring radius measurement
	5.1.5	Mechanical testing and stress-stretch analysis
	5.1.6	Constitutive modeling framework
	5.1.7	Mechanical parameters and stiffness calculations
	5.1.8	Histology and tissue composition
5.2		JLTS
	5.2.1	Micturition patterns
	5.2.2	Changes to effective bladder wall radius
	5.2.3	Changes to stress-stretch curves and constitutive parameters
	5.2.4	Transition regimes and tissue stiffness
	5.2.5	Histology and tissue composition
5.3		USSION
5.5	5.3.1	
5.4		CLUSIONS
3.4	CON	CLOSIONS
СНАРТ	_	CONCLUSIONS AND FUTURE WORK
6.1		ATED LEFT VENTRICLE INTER-CONSTITUENT MECHANICAL IN-
		ACTION
6.2	INTE	R-CONSTITUENT MECHANICAL INTERACTION IN THE
	URIN	JARY BLADDER
6.3	CON	CLUDING REMARKS 97

APPENDIX		• • •	• •	 	 •	•	 	•	•	 •	•	•	 •	•	•	 •	•	•	•	 •	•	•	 9	9
RIBI IOGRAPH	Y																						10	7

LIST OF TABLES

Table 2.1:	Model parameters measured from experimental data	22
Table 3.1:	Best-fit material parameters values estimated for the model presented in Equation 3.1 for each group (avg. ± st.dev)	43
Table 4.1:	FBG levels and body weights of each group at time of euthanasia (avg. \pm st.dev.).	64
Table 4.2:	Geometry measurements taken for each group (avg. \pm st.dev.)	64
Table 4.3:	Area fractions of tissue constituents for each group (avg. ± st.dev.)	64
Table 4.4:	Estimated material parameter values for the model fit of each group (avg. \pm st.dev.). * - P < 0.05 compared to GK-C; no other comparisons were significant	66

LIST OF FIGURES

Figure 1.1:	Anatomy of the heart. Arrows represent direction of blood flow. Note: Picrosirius Red (PSR) images may be slightly distorted, and are intended for composition illustration only	4
Figure 1.2:	Anatomy of the urinary bladder. Arrows represent direction of urine flow. Note: Verhoeff Van Gieson (VVG) images may be slightly distorted, and are intended for composition illustration only.	5
Figure 1.3:	Schematics of types of mechanical tests	9
Figure 1.4:	Schematic of a classical opening angle test for soft biological tissues	9
Figure 2.1:	(a) Distribution of tissue samples. Definitions of the (b) opening angle and (c) inner and outer radius of the ring tissue samples	15
Figure 2.2:	Schematic representation of the configurations of interest in the CMMI modeling framework	18
Figure 2.3:	Fitting the strain energy density function parameters using uniaxial mechanical test data from (a) isolated myocyte[8] and (b) individual collagen fibril[131]. Dots: data points of the experimental measurements. Line: stress–strain relationship with the best-fit parameter values. Stress: first Piola Kirchhoff stress. Strain: Green-Lagrange strain. Tangent stiffness: $\frac{dPK1}{d\lambda}$ where λ is the stretch	23
Figure 2.4:	Changes in opening angle at different time points after the radial cut in the samples from male rats	24
Figure 2.5:	Comparison of opening angle between male and female rats	25
Figure 2.6:	Histology images of tissue samples from the male rats hearts. Top row: H&E (nuclei in purple and cytoplasm in pink); bottom row: Picrosirius red under polarized light (collagen fibers in red, yellow and green). Left: Intact samples, center: myocytes-only samples (collagenase-treated), and right: collagen-only samples (decellularized). Bar in each image represents 500 μm .	26
Figure 2.7:	SEM images of tissue samples from the male rats hearts. Left: myocyte-only samples (collagenase-treated) and right: collagen-only samples (decellularized). Bar in each image represents 10 µm	27

Figure 2.8:	Opening angle Φ as a function of the collagen mass fraction ϕ^c without interconstituent mechanical interaction. Φ^m , Φ^c , and Φ^* denote measured values of the opening angle for myocytes-only, collagen-only and untreated tissue, respectively. Inset: close-up view ($0 \le \phi^c \le 5\%$) showing that the measured mixture opening angle is recovered by the model when $\phi^c = 0.06\%$		28
Figure 2.9:	Effects of isotropic collagen compression on the mixture opening angle. Curves represent mixture opening angle Φ relationship with the collagen mass fraction ϕ^c at different compression level α^c . Φ^m , Φ^c , and Φ^* denote measured values of the opening angle for myocytes-only, collagen-only and untreated tissue, respectively. Note that the graph is truncated at $\phi^c = 10\%$ because all the curves plateau to a constant value when $\phi^c > 10\%$		29
Figure 2.10:	Effects of mixture opening angle caused by simultaneous collagen compression ($\alpha^c < 1.0$) and myocyte tension ($\alpha^m > 1.0$) in the interaction. Curves represent mixture opening angle Φ relationship with the collagen mass fraction ϕ^c with different combinations of α^c and α^m . Φ^m , Φ^c , and Φ^* denote measured values of the opening angle for myocytes-only, collagen-only and untreated tissue, respectively		30
Figure 2.11:	Effects of mixture opening angle caused by isotropic myocyte compression $(\alpha^m < 1.0)$. Collagen interaction parameter α^c determined so that $\Phi = \Phi^*$ at $\phi^c = 10\%$. Curves represent mixture opening angle Φ relationship with the collagen mass fraction ϕ^c at different combinations of α^c and α^m		31
Figure 2.12:	Comparison of the three different mechanical interactions considered. Myocytes and collagen interaction parameters, α^m and α^c , determined so that $\Phi = \Phi^*$ at $\phi^c = 10\%$. Curves represent myocytes stretch in the circumferential (black) and in the direction of the myocytes across the wall (gray)	•	32
Figure 2.13:	Summary of the effects of three different types of mechanical interactions on opening angle. Myocytes and collagen interaction parameters, α^m and α^c , determined so that $\Phi = \Phi^*$ at $\phi^c = 10\%$. Curves represent mixture opening angle Φ relationship with the collagen mass fraction ϕ^c at different combinations of α^c and α^m		35
Figure 3.1:	Schematic of mechanical testing set-up. Isolated myocytes from Sprague Dawley rat left ventricle used for illustrative purposes		40
Figure 3.2:	Cauchy stress vs. stretch experimental dataset (symbols) and model best-fit description (lines)		41
Figure 3.3:	Transmural residual stress distribution for one representative sample, showing stress points of interest	•	45

Figure 3.4:	ing stretch points of interest. Note: while the axial stretch assumes in most cases values close to 1, no plain strain assumption was made	46
Figure 3.5:	Cross-sectional area evaluated for all samples (avg. ± st. err.)	46
Figure 3.6:	(a-f) Images of picrosirius red stained slides of male (a-c) and female (d-f) left ventricle (a, d: NT; b, e: CD; c, f: HFD). (g) Collagen area fraction evaluated for all samples (avg. ± st. err.)	47
Figure 3.7:	Opening angle (deg) measured for all samples (avg. \pm st. err.). (a) Comparison between isolated myocytes, isolated collagen fibers, and intact tissue for both CD and HFD. (b) Comparison between CD and HFD (also included data for NT)	48
Figure 3.8:	Comparison between isolated myocytes, isolated collagen fibers, and intact tissue for both CD and HFD of the maximum value of (a) circumferential residual stress (t_{θ} , as identified in Figure 2) and (b) circumferential stretch (λ_{θ}) for all samples (avg. \pm st. err., note: the graphs have different vertical axes).	50
Figure 3.9:	Comparison between sex of the animal, including data for NT, of the maximum value of (a) circumferential residual stress (t_{θ} , as identified in Figure 3.3) and (b) circumferential stretch (λ_{θ} , as identified in Figure 3.4) for all samples (avg. \pm st. err., note: the graphs have different vertical axes)	51
Figure 3.10:	Non-dimensional radial location of the circumferential neutral axis in intact tissue for all for all samples (avg. \pm st. err.). Non-dimensional radius of 0 indicates the inner wall, while a value of 1 indicates the outer wall. Comparison between CD and HFD (also included data for NT)	52
Figure 4.1:	(a) Measurement locations for bladder sample geometry (GK-C bladder used for illustration). (b) Image of a stained slide taken on a desktop to measure the wall thickness, t_{wall} , and ring cross-sectional area, A_{ring}	59
Figure 4.2:	Representative mast cells and their scores from a ZDF diabetic bladder in t-blue stain	60
Figure 4.3:	Experimental set-up and sample geometry	61
Figure 4.4:	Left: NMCA score for each group, Right: mast cell density for each group. Error bars show standard error, \dagger - P < 0.1, * - P < 0.05	65

Figure 4.5:	Average stress-stretch curves for each test group (markers) and simulated stress-stretch curves from model (lines), for GK (left) and ZDF (right). White markers represent controls, and black markers represent diabetics. Error bars and shaded regions represent standard error of experimental stretch and standard error of model-predicted stretch, respectively. Significance values refer to mechanical data, * - P < 0.1, ** - P < 0.05	66
Figure 4.6:	Perturbations of a simulated stress-stretch curve through manipulation of c and k .	67
Figure 4.7:	Percentage changes from mean parameter stress through perturbation of material parameters. Shaded regions represent possible values in the range of parameters optimized in this study. Black star indicates the earliest value of stress where k sensitivity could overtake c sensitivity	68
Figure 5.1:	Protocol for estimating effective bladder radius	76
Figure 5.2:	Experimental set-up for uniaxial testing	78
Figure 5.3:	Transition regions and points of interest for a representative (control) stress-stretch model curve	80
Figure 5.4:	Changes in micturition behavior by radiation treatment and recovery time. Statistical symbols: *P < 0.1, compared to untreated, **P < 0.05, compared to untreated, \diamond P < 0.1, compared to 3 months, \diamond \diamond P < 0.05, compared to 3 months.	82
Figure 5.5:	Changes to effective bladder radius, caused by radiation treatment, recovery time, and decellularization (average +/- standard error). Statistical symbols: $^*P < 0.05$, compared to untreated, $^*P < 0.05$, compared to 3 months, $^*P < 0.05$, compared to intact tissue	83
	Average +/- standard error stress-stretch curves for all samples. *P < 0.1, **P < 0.05	83
Figure 5.7:	Average +/- standard error parameters from the constitutive model. *P < 0.1, **P < 0.05	84
Figure 5.8:	Average +/- standard error regime endpoints. **P < 0.05	85
Figure 5.9:	Average +/- standard error low and high stiffnesses of the consitutive model stress-stretch curves. ** $P < 0.05$	86
Figure 5.10:	Top: Elastin and collagen I content in the decellularized rings. Bottom: Total collagen area fraction of the non-decellularized, second cohort of bladders	87

Figure 6.1:	Observed mechanical data vs. material parameters obtained from literature for isolated collagen fibers [131] and isolated myocytes [8]. Shaded regions represent standard error model predictions
Figure 6.2:	Configurations of interest and deformation gradients for estimating urinary bladder inter-constituent interactions
Figure 6.3:	Opening angles obtained from three urinary bladder tissue compositions 97
Figure .4:	Configurations of interest for part 1 of the opening angle inter-constituent interaction model
Figure .5:	Configurations of interest for part 2 of the opening angle inter-constituent interaction model
Figure .6:	Configurations of interest for part 3 of the opening angle inter-constituent interaction model

CHAPTER 1

INTRODUCTION AND LITERATURE REVIEW

1.1 INTRODUCTION

Each organ has its own unique structure and tissue composition. The mechanical behavior of the organ and its tissues is dependent upon its structure and is crucial to its function. Further, diseases can affect mechanical properties of tissues and organs through remodeling, disrupting healthy function, and accelerating disease progression. Development of descriptive and accurate constitutive models of soft tissues is key in understanding both healthy and diseased organ mechanical behavior. Many of these models have been developed in regard to tissue structure (i.e. constituents such as collagen fibers, elastin fibers, and cells), and validated through mechanical data from experiments such as uniaxial, biaxial, or pressure-volume tests. The existence of such models could pave a path for predictive and patient-specific medicine. Patient-specific modeling-i.e. creating a 3D finite element model (FEM) based on patients' organs own geometries acquired through imaging-could be very useful in diagnostics or development of treatment plans. They are informed by constitutive models, either based on experimental results or optimized through simulation. Several previous studies have created FEMs based on human geometry of the heart, with focus on the left ventricle [80, 154, 41, 43, 113]. Human geometry-based bladder FEMs, on the other hand, are not as common. One study focused an FEM of the urinary bladder specifically to study radiation cystitis [11], while a few others have included the urinary bladder in multi-organ models of pelvic floor prolapse [13, 6, 78]. In order to be suitable for medical applications, it is important that these models are as descriptive as possible, in terms of constituent-specific parameters. Both left ventricle and urinary bladder FEMs would benefit from accurate, constituent-specific models of their comprising tissues, both in the healthy and pathological states.

There are several characteristics of soft biological tissues that pose challenges in developing constitutive models: (1) soft biological tissues exhibit highly nonlinear behavior as well as (2)

viscoelastic behaviors, and (3) it can be difficult to translate an in vivo loading configuration with respect to an *in vitro* experiment. The nonlinearity and viscoelasticity of soft biological tissues are the direct result of their constituents' structures. In the left ventricle, myocytes are tightly woven in a collagen fiber matrix while, in the urinary bladder, there are multiple layers consisting of smooth muscle cells, epithelial cells, collagen fibers, and elastin fibers. Generally, in both tissues, the nonlinearity is generated by the uncoiling and straightening of individual fibers (collagen and/or elastin) as the tissue is loaded. In disease-states, remodeling may take form in increased deposition or degradation of these fibers, resulting in altered mechanical behavior of the tissue. Viscoelasticity, on the other hand, may be a result of water contained within the tissue being redistributed as the tissue is loaded and unloaded. Similarly to the collagen and elastin fibers, viscoelasticity can also be affected by disease. Specifically, in an inflamed tissue, there may be an increase in edema (or swelling) of the tissue, thereby affecting the ability of the tissue to display healthy viscoelastic behavior. Finally, a challenge lies within determining what is the *in vivo* loading configuration of a tissue. This has been demonstrated by experiments showing residual stress residing in explanted tissues [103, 85] and determining in vivo axial stretches of arteries [56]. Additionally, studies have shown that with preconditioning and cyclic loading, one can obtain repeatable curves that do not display signs of viscoelasticity (i.e. loss of energy between loading and unloading) [15, 30, 65]. In order to address these issues, many constitutive models including nonlinear and viscoelastic behavior have been developed and validated [27, 117, 62, 61, 40]. A useful summary of commonly used constitutive models for soft biological tissues can be found in a review by Chagnon et. al. [10].

This dissertation aims to extend established constitutive models of the left ventricle and urinary bladder by accounting for interconstituent mechanical interactions, and use them to characterize altered mechanical behavior in pathologically remodeled tissue.

1.2 LITERATURE REVIEW

In the following sections, I will discuss the current state of the literature as it pertains to anatomy and tissue composition of the left ventricle and urinary bladder, diseases of these organs and associated remodeling, and, finally, mechanical testing and constitutive models of these tissues.

1.2.1 Anatomy and tissue composition

Both the left ventricle of the heart and urinary bladder function as pumps—the first for oxygenated blood distribution, and the second for urine excretion. However, the two are very different in their typical loading states. On one hand, the left ventricle has a loading-unloading cycle of 60-100 beats per minute, a pressure variation of 0-120mmHg (or 0-16kPa), and a volume range during its cycle of about 50-120mL [91, 67]. On the other hand, the urinary bladder has a loading-unloading cycle of about 8 voids per day, intravesicle pressure remains relatively constant during filling at around 37mmHg (or 4.9kPa), and an average volume fluctuation of 0-400mL [86, 79, 33, 37]. In other words, the heart has a fast, high-pressure, low strain deformation cycle, while the urinary bladder has a slow, low-pressure, high strain cycle. Previous studies show, however, that both tissues exhibit nonlinear, viscoelastic behavior [120, 59, 31, 25, 53, 97, 44, 149], controlled by their constituent structures.

The role of the left ventricle of the heart is to pump oxygenated blood through the aorta to be distributed throughout the body. Because the left ventricle has to pump blood at such a high pressure, it is a largely muscular organ. Among the many constituents found in the myocardium, myocytes and collagen fibers are arguably the two most prominent ones for the following reasons. First, myocytes account for the vast majority of the myocardial mass (nearly 90% of its dry weight [51]), see Fig. 1.1. Second, collagen fibers are significantly stiffer (when fully stretched) and form the extracellular matrix scaffold that provides strength for the myocardium. Collectively, these two constituents contribute to the myocardium's overall mechanical and functional behaviors found under physiological and pathophysiological conditions.

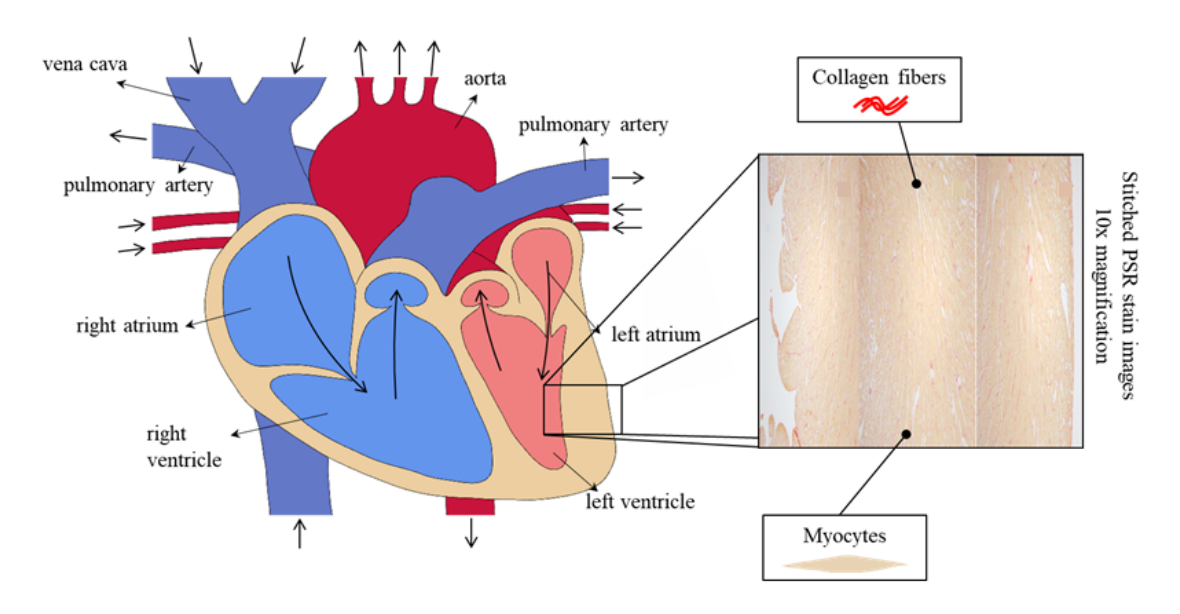


Figure 1.1: Anatomy of the heart. Arrows represent direction of blood flow. Note: Picrosirius Red (PSR) images may be slightly distorted, and are intended for composition illustration only.

The urinary bladder functions by passively filling with urine, then contracting to void. It is a multi-laminate organ containing 4 distinct layers, Fig. 1.2, starting from the lumen outward: (1) Urothelium, composed of urothelial (i.e., epithelial) cells, (2) Lamina Propria, composed primarily of collagen and elastin fibers, (3) Detrusor Muscle, composed of smooth muscle cells bounded by collagen and elastin fibers, and (4) Adventitia, composed of collagen and elastin fibers. The detrusor muscle accounts for the majority of the urinary bladder wall volume, followed by collagen fibers. Elastin fibers, though they only account for less than 3% of the dry weight or less than 1mg/g wet weight of the urinary bladder [96, 19], are a key contributor to the mechanical behavior of the urinary bladder. Unlike collagen, which is quite stiff when fully straightened, elastin fibers are quite deformable and exhibit highly elastic behavior. It is hypothesized that elastin may contribute to the strength of the urinary bladder, through maintaining the collagen fibers' waviness [149]. The high compliance of the urinary bladder, then, is attributable to the high waviness of the collagen fibers, which may be controlled in some amount by elastin fibers.

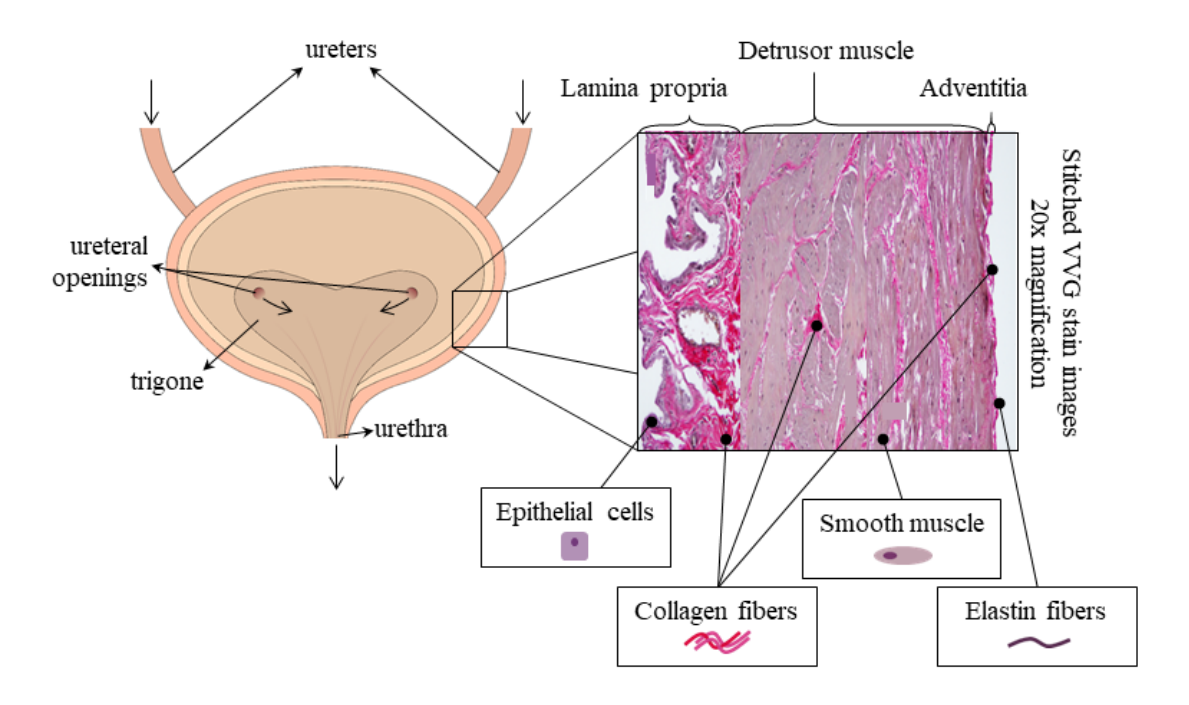


Figure 1.2: Anatomy of the urinary bladder. Arrows represent direction of urine flow. Note: Verhoeff Van Gieson (VVG) images may be slightly distorted, and are intended for composition illustration only.

1.2.2 Disease and remodeling

Left ventricular remodeling in hypertension: Cardiovascular disease has long been known to be the number 1 cause of death in the United States. It is estimated that by 2030, over 40% of the population will be affected by some form of cardiovascular disease and that this will cost the U.S. over \$818 billion annually in medical expenses [58]. Cardiovascular disease, specifically hypertension, has been shown to alter the left ventricle tissue structure, composition, and ultimately mechanical behavior [126, 105]. Exposed to high afterload over a prolonged period of time, pathological features emerge in the left ventricle, such as myocyte hypertrophy, fibrosis, and elevated resting tension of the myocytes, this is known as concentric hypertrophy globally [102, 139]. These microstructural pathological changes can also affect the residual stress/strain distribution in the left ventricle as shown in previous studies, which reported a larger opening angle in the intact hearts subjected to pressure overload by aortic banding [107] but a lower opening angle in the intact embryonic chick heart also subjected to pressure overload [135]. Characterization of residual

stress/strain is important as these quantities may affect the transmural sarcomere length distribution [125] that may in turn affect myocyte force generation [23]. Studies on changes of the residual stress/strain associated with pressure overload have, however, focused on the bulk tissue mechanical response and do not distinguish the contributions of the tissue constituents. Understanding the contribution of the constituents is important because novel therapies have been proposed to target key pathological features, such as attenuating myocardial fibrosis [155] and reducing myocyte titin stiffness [77]. Moreover, most studies were also performed without considering sex as a biological variable that may be important in hypertension. This is especially so given that there are observed sex-differences in this disease, such as its prevalence and mechanisms—specifically, that it is more prevalent in men, and therefore understudied in women [118].

Bladder remodeling in type II diabetes and radiation cystitis: In 2017, 23.1 million people have been diagnosed with diabetes, which cost a total of \$245 billion in health care expenses in the US [18]. Of this group, about 95% have type II diabetes. Bladder dysfunction of some kind has been reported in roughly 80% of individuals with diabetes and is the most common comorbidity with this disease [22]. Bladder dysfunction in diabetic patients (also known as diabetic cystopathy) has a complex, multifactorial pathophysiology. An important contributing factor is peripheral neuropathy, caused by prolonged altered blood glucose levels [151]. This causes disconnect between the bladder and the central nervous system, leading to increased time between voids and increased urine storage, leading to overall increases in bladder wall compliance. Symptoms associated with diabetic cystopathy may include feelings of urgency, incontinence, or insufficient voiding [36, 71, 72]. Through analysis of remodeling and mechanical behavior changes associated with this disease, we may develop a better understanding of the effect that diabetic cystopathy may have on urinary bladder function. Remodeling of the urinary bladder has been studied in type I diabetic animal models in terms of inflammation, extracellular matrix protein degradation/synthesis, muscle contractility, and mechanical behavior of the tissue (specifically, a decrease in tissue stiffness)[22, 83, 144, 16, 93, 138, 116, 84, 101, 114, 124, 49]. However, these changes to the urinary bladder as a result of diabetic cystopathy have been largely understudied

with respect to type II diabetes. Some studies have found that there are changes to the structure and content to the bladder wall such as thickening and edema [73, 39]. However, to our knowledge, no current studies have reported changes to the extracellular matrix protein content or mechanical properties of the tissue following type II diabetic onset.

A second pathology of interest in the urinary bladder is radiation cystitis. Radiation cystitis can develop when a patient undergoes radiation chemotherapy for pelvic organ cancer. The condition can develop over the first few weeks (acute phase) following treatment, but may lay dormant for months (latent phase) and eventually cause serious complications years later (late/chronic phase) [158]. It is known to cause, painful, frequent urination, incontinence, and blood in the urine. In the case of blood clot blockage of urine, radiation cystitis can also result in kidney failure [158]. Because this response to radiation is relatively rare—it occurs in only about 5-10% of patients undergoing radiation treatment of pelvic cancer [133]—it is often overlooked. However, this disease can be painful and debilitating, and can ultimately inhibit cancer patients' recoveries. With respect to tissue remodeling, it is known to cause inflammation, hypervascularization, thickened bladder walls, disruption to the urothelium, and increased collagen deposition [87, 69, 68, 70, 75, 60, 76]. Conversely to diabetic cystopathy, radiation cystitis has been shown to significantly increase the amount of collagen in the urinary bladder wall and cause a decrease in compliance of the bladder [156, 159, 70, 75, 76]. Currently, however, no studies have reported how this fibrosis may impact the mechanical behavior of the tissue.

1.2.3 Mechanical tests and constitutive models

In general, constitutive models of the urinary bladder and left ventricle are composed in the form of a strain energy density function, W, that defines the relationship between stress and deformation. In this dissertation, we will consider soft biological tissues to be incompressible, and so the relationship between W, the stress T, and the deformation gradient F (through the right Cauchy-Green tensor $C = F^T F$) is

$$W = -pI + 2F \frac{\partial W}{\partial C} F^{T}$$
(1.1)

where p is a Lagrange multiplier, and can be solved for using boundary conditions. Each unique definition of W will have its own set of material parameters that must be optimized through experimental data—i.e. uniaxial, biaxial, triaxial, or pressure-volume testing. A schematic of examples of these types of mechanical tests can be found in Fig. 1.3.

A uniaxial tensile test involves loading a tissue sample in one direction of interest (often circumferential for left ventricle and urinary bladder). Then, stress and stretch are calculated using the force in the loading direction, F_x , and deformation in the x-direction. Additionally, there is an assumption of zero stress boundary conditions in the transverse plane. A biaxial test, on the other hand, will involve stretching a sample in two directions (typically circumferential and longitudinal for the urinary bladder and left ventricle). Here, the loading forces F_x and F_y , along with deformations in the x- and y-directions, are used to calculate normal and shear stresses and stretches. In this case, the zero stress boundary condition would be applied in the z-direction only. Finally, a pressure-volume test involves filling a sample, e.g., bladder, left ventricle, or artery, with fluid, while measuring changes in intra-luminal pressure, P_r , and deformation of the radius and circumference. When applying stretch in the axial direction (for tube-shaped samples), this method is considered a triaxial test. Then, from P_r , F_z , stress, and stretch can be computed in the radial, circumferential, and axial directions.

A key mechanical feature of the myocardium is the existence of residual (or internal) stresses in the intact left ventricle. Residual stress refers to the stress that resides within a material after all external loads have been removed. In biological tissues, this often is observed in hollow, cylindrical organs such as arteries, [17], and the left ventricle [103]. The existence of residual stress in biological tissues has produced the need for a type of mechanical test known as the opening angle test. This type of experiment consists of producing a radial cut in a ring sample excised from the artery or ventricle which produces a sizable opening angle, Fig. 1.4. Currently, no published studies have concluded that the urinary bladder has residual stress.

Fung Model – One of the most commonly used strain energy functions for soft biological tissues was developed by Tong and Fung in 1976 with specific applications to skin [140]. The

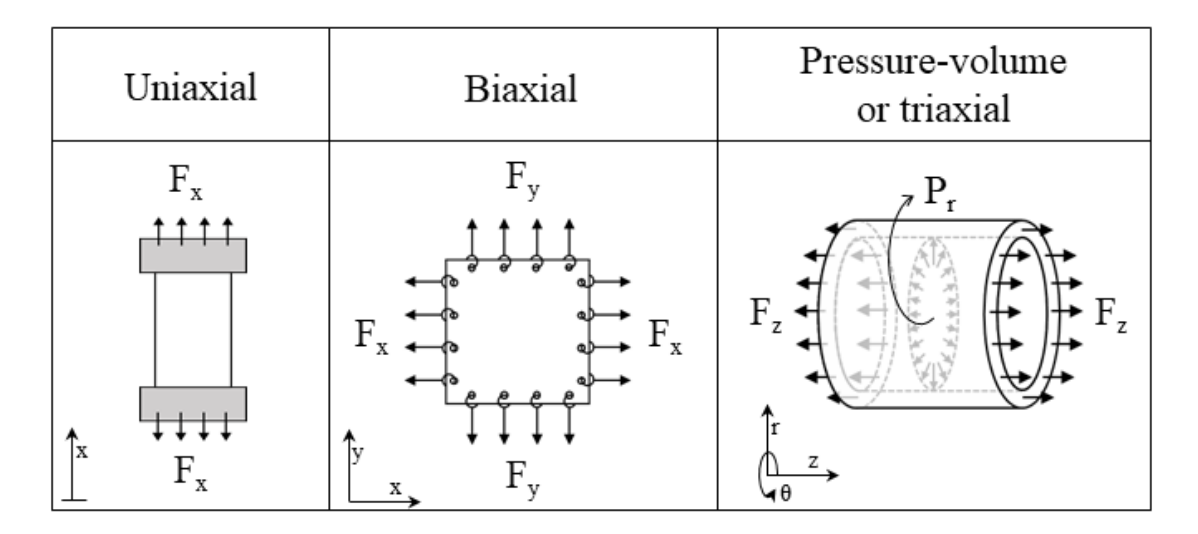


Figure 1.3: Schematics of types of mechanical tests.

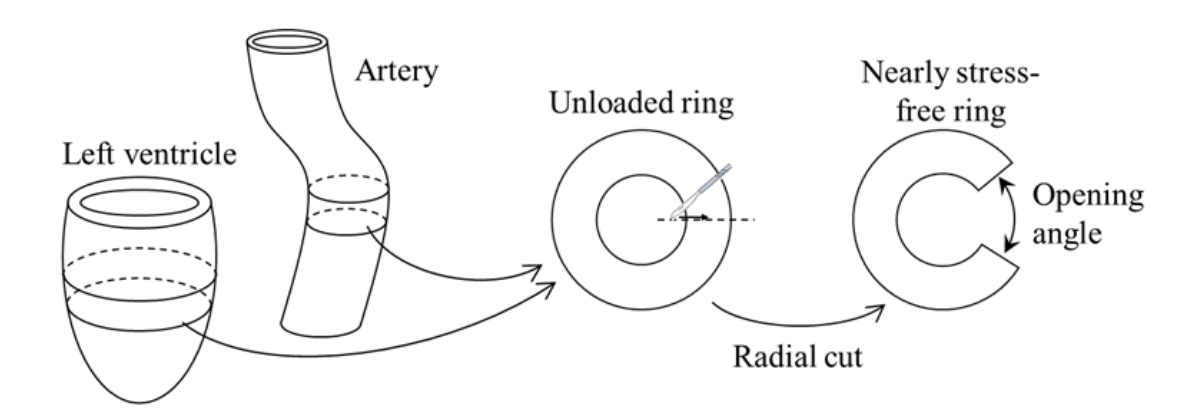


Figure 1.4: Schematic of a classical opening angle test for soft biological tissues.

general form of a Fung-type constitutive model is

$$W = \frac{c}{2} (e^Q - 1) \tag{1.2}$$

where Q is a function of the Green-Lagrange strain tensor, E, and varying numbers of material parameters. There are many forms of Q, and this material model has been fitted to describe left ventricle [150, 53, 104, 20] as well as urinary bladder [143] mechanical behavior.

Demiray Model – The model proposed by Demiray et. al. [26] is an exponential model derived as a general constitutive model for any soft biological tissue, under an isotropic assumption

$$W = \frac{c_1}{c_2} \left[e^{c_2(I_1 - 3)} - 1 \right],\tag{1.3}$$

where c_1 and c_2 are material parameters. Here, I_1 is the first invariant (trace) of the right Cauchy-Green deformation tensor, C, of the deformation gradient, F-i.e. $C = F^T F$. Though this constitutive model is technically in the form of a Fung-type material, and is the only isotropic material described here, I highlight it specifically, as this model will be used in each of the following chapters and acts as the base constitutive model for all of the work presented here.

Two-Fiber Family of Collagen Model – A model that is used to capture mechanics correlated with fiber direction is the two-fiber family of collagen model, originally proposed for arterial mechanics in 2000 [62]

$$W = \frac{c_1}{2} (I_1 - 2) + \sum_{k=1,2} \frac{c_1^k}{4c_2^k} \left[e^{\left\{ c_2^k ((\lambda^k)^2 - 1)^2 \right\}} - 1 \right]$$
 (1.4)

where

$$\lambda^{k} = \sqrt{\lambda_{\theta}^{2} sin^{2}(\alpha^{k}) + \lambda_{z}^{2} cos^{2}(\alpha^{k})}$$
(1.5)

and k denotes the number of families of collagen. Additionally, c_1 , c_1^k , and c_2^k are material parameters and α^k represents the orientation angle of each family of collagen. Like many Fungtype models, this allows for description of the material in orthotropic assumptions. However, rather than the basis being dependent only the strain in different directions, E, which is a direct result of the deformation applied, we now have a descriptor λ^k that provides information on the preferential directions of the material.

Holzapfel-Ogden – In 2009 G. A. Holzapfel and R. W. Ogden [63] developed a model specifically for the passive myocardium (i.e. left ventricle tissue), known as Holzapfel-Ogden model, of the form

$$W = \frac{a}{2b}e^{b(I_1-3)} + \sum_{i=f,s} \frac{a_i}{2b_i} \left[e^{b_i \left(I_{4i}-2 \right)^2} - 1 \right] + \frac{a_{fs}}{2b_{fs}} \left[e^{\left(b_{fs} I_{8fs}^2 \right)} - 1 \right], \tag{1.6}$$

where f and s refer to the directions in parallel and normal to the collagen fiber direction, respectively. The invariants I_{4f} , I_{4s} , and I_{8fs} are used to normalize the right Cauchy-Green deformation tensor, C, along these directions and are defined as

$$I_{4f} = f_0 \cdot (Cf_0), I_{4s} = s_0 \cdot (Cs_0)$$
(1.7)

$$I_{8fs}\Big(=I_{8sf}\Big)=f_{\mathbf{0}}\cdot(Cs_{\mathbf{0}})\tag{1.8}$$

where f_0 and s_0 are the unit vectors along the f and s directions, respectively. These directional parameters allow for estimations based on structural measurements of the tissue rather than all being based on mechanical data, and so, de-coupling some parameters and producing a more descriptive model. Several studies have since applied this model to mechanical data of the left ventricle [63, 38, 145, 100].

 $GOH\ Model$ – The GOH model can be viewed as an updated version of the two-fiber family of collagen model by Gasser, Ogden, and Holzapfel in 2006, [40], with an allowance for distribution for fibers (rather than assuming that all fibers are aligned perfectly in directions α^k)

$$W = \frac{c_1}{2} (I_1 - 2) + \sum_{k=1,2} \frac{c_1^k}{2c_2^k} \left[e^{\left\{ c_2^k E_k^2 \right\}} - 1 \right]$$
 (1.9)

where

$$E_2^k = \kappa I_1 + (1 - 3\kappa)(\lambda^k)^2 - 1 \tag{1.10}$$

and λ^k was defined in Equation (1.5) and the material parameters are the same as in the two-fiber family of collagen model as defined in equations 1.4 and 1.5, [62]. Here, κ represents a dispersion parameter that is bounded by $0 \le \kappa \le 1/3$. For $\kappa = 0$, the fibers are perfectly aligned along α^k (and the two-fiber family of collagen model is obtained) and for $\kappa = 1/3$, the fibers are completely randomly distributed, and the material is isotropic.

Additionally, there are many constitutive models that characterize viscoelasticity and fiber recruitement of the urinary bladder [96, 149, 98, 142, 122]. However, these will not be included as these topics are not a focus of this dissertation.

1.3 KNOWLEDGE GAPS AND MOTIVATION

Constitutive modeling of soft biological tissues has evolved from simply attempting to capture the non-linearity to understanding preferential directions of fiber matrices and viscoelasticity. While these advancements have been quite useful, there are still fields left unexplored in modeling of the left ventricle and urinary bladder mechanical behavior.

Though residual stress fields have been measured in the left ventricle of rats [103], canine [21], and embryonic chick [136], neither the relative contribution of myocytes and collagen fibers nor the sex effects on the resultant stress fields have been investigated. As such, there is currently a void in our understanding of how myocytes and collagen fibers individually affect the residual stress that plays an important role in left ventricle mechanics [99, 42]. Additionally, we currently have no measure of residual stress (either in intact tissue or individual constituents) in the urinary bladder.

In relation to this, the constrained mixture theory remains a useful (and popular) way to account for the separate contribution of myocytes and collagen fibers to soft tissue mechanical behavior. Application of the constrained mixture theory can be found in a number of microstructural models of ventricular mechanics [64, 2]. In these models, the myocardial tissue mechanical behavior is described based on the weighted sum of each constituent's strain energy density function that characterizes the constituent's mechanical behavior. That description implicitly assumes that each constituent contributes to the overall mechanics simply by their mere presence, without accounting explicitly for any physical or mechanical interactions between them. It is, however, very difficult to reconcile this assumption given that scanning electron microscopy images have revealed a tight physical connection between collagen fibers and myocytes in the myocardial tissue [147].

While it is fairly obvious that the extracellular matrix interacts mechanically with cells given that they are microstructurally enmeshed together in the tissue [88], to the best of our knowledge, little has been done to characterize the mechanical interactions between these constituents at the tissue level. Related works are mostly confined to in vitro characterization of the cell–cell and cell–matrix adhesion occurring at the microscopic level [7, 90], which are difficult to extrapolate macroscopically to the tissue level. Most related studies also focus on the biochemical signaling arising from inter-constituent mechanical interaction. Our knowledge of the direct mechanical and physical interaction between collagen fibers and cells, and how this interaction contributes to soft tissue mechanics therefore remains rudimentary.

Several papers have studied remodeling-related changes to the mechanical behavior of bladder tissue with respect to spinal cord injury [96, 97, 46, 141], and type I diabtic cystopathy [144, 16],

and have found that both of these pathologies result in remodeled bladder tissue as well as a decrease in bladder wall stiffness. However, little has been done to understand how diseases like type II diabetic cystopathy and radiation-induced cystopathy affect bladder tissue mechanical behavior. It is important to study the mechanical behavior of the healthy urinary bladder, as well as how it changes with these diseases in order to provide insight into remodeling and disease progression.

In regard to these gaps in knowledge, the main goals of the following chapters are to: (1) establish that there are separate contributions to residual stress in the left ventricle by the individual tissue constituents, (2) confirm that there is an inter-constituent mechanical interaction between the myocytes and collagen fibers in the left ventricle that cannot be ignored, (3) characterize the alterations to the constituent contributions to the left ventricle residual stress following hypertension (as well as highlight sex-related differences), (4) obtain mechanical properties of both healthy and type II diabetic bladder tissue in both lean and obese states, and (5) analyze radiation cystitis-affected urinary bladder tissue and provide insights into the relations between radiation dose, recovery time, and altered tissue mechanical behavior.

CHAPTER 2

CONTRIBUTION OF LEFT VENTRICULAR RESIDUAL STRESS BY MYOCYTES AND COLLAGEN: EXISTENCE OF INTER-CONSTITUENT MECHANICAL INTERACTION

As introduced in the Literature Review section, no current constitutive models of left ventricle tissue account for a mechanical interaction between myocytes and their surrounding collagen fiber matrix. To infer the existence of any direct mechanical interaction between the two constituents, we employed these measurements to inform a constrained mixture modeling framework that takes into account the contribution of myocytes and collagen fibers to the left ventricle mechanical behavior simply by their presence. Specifically, we seek to test the hypothesis that this modeling framework can reproduce the measured opening angle found in the left ventricle. The rationale is as follows: if the hypothesis is validated, it would imply that the myocyte–collagen mechanical interaction only has negligible effects (if any) on the myocardial tissue mechanics, while conversely, if the hypothesis is invalidated, it would imply that the resultant left ventricle mechanical behavior cannot be described by the constituent's mere presence. We show that our results imply the latter, suggesting the existence of myocyte–collagen mechanical interaction that cannot be ignored in describing left ventricle mechanics. We then propose and show that this discrepancy can be resolved in an extended constrained mixture formulation with the introduction of a mapping that is associated with the constituent's deformation arising from their interaction.

2.1 METHODS

For this study, healthy adult male (n=15) and female (n=15) Sprague Dawley rats (Charles River Breeding Laboratories, Portage, MI) were euthanized with pentobarbital (60–80 mg/kg i.p.), and their hearts were dissected. All animal protocols used in this study were approved by MSU Institutional Animal Care and Use Committee.

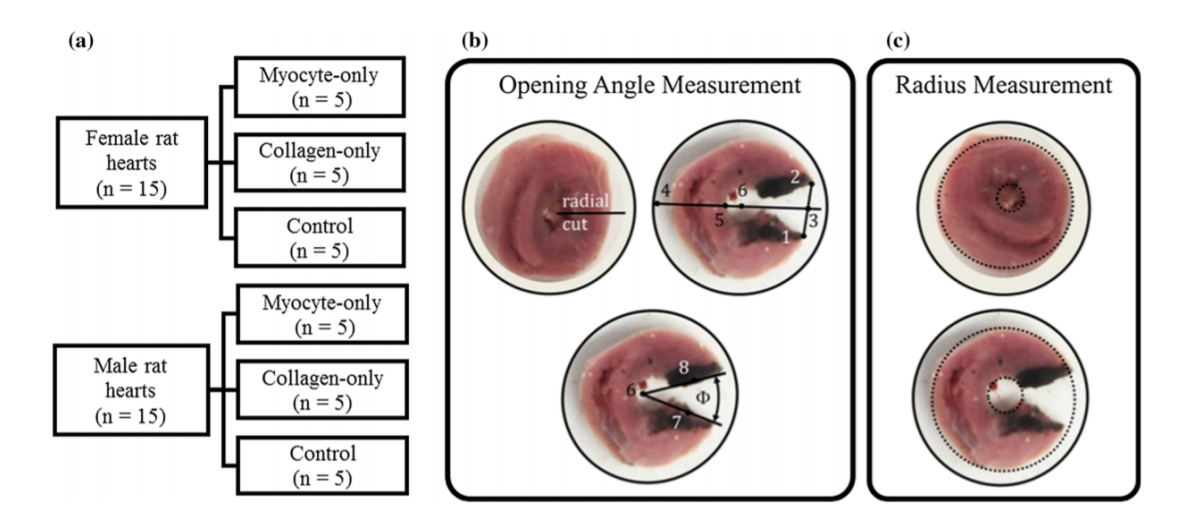


Figure 2.1: (a) Distribution of tissue samples. Definitions of the (b) opening angle and (c) inner and outer radius of the ring tissue samples

2.1.1 Sample preparation

Two lateral ring samples showing the left ventricle (LV) and right ventricle (RV) were excised from each heart with an approximate thickness of 4.4 mm. Ring samples obtained from each sex were subdivided equally into three test groups, which were the (1) myocyte-only (n = 5), (2) collagen-only (n = 5) and (3) control (intact tissue = myocytes + collagen) (n = 5) groups, Fig. 2.1.

Ring samples from the control group were soaked in a Krebs–Henseleit buffer solution containing 2,3-butanedione monoxime (BDM), a myosin inhibitor that inhibits cross-bridge formation [54] by interfering with Ca₂⁺ – troponin interaction [95]. On the other hand, ring samples in the myocyte-only group were first soaked in the same buffer + BDM for 15 min before being soaked for 96 hours in a buffer solution (10 mg/L Sigma-Aldrich Chemicals) containing CaCl₂ and crude bacterial collagenase, a collagen-disrupting enzyme that breaks down the collagen fiber network. The chemical CaCl₂ was added to the solution because collagenase requires calcium to activate the enzymatic degradation [89]. After the treatment (96 hours), the samples were moved back to a Krebs–Henseleit buffer solution containing BDM. Finally, ring samples in the collagen-only group were first soaked (for 15 min) in a heparinized saline solution before being transferred to and soaked for 96 hours in a 1% sodium-dodecyl sulfate solution to remove the cells and cellular

residua, leaving only the extracellular matrix scaffold. Thereafter, these samples were soaked in deionized water for 15 min and then in a 1% Triton X-100 solution for 30 min before testing [110]. The efficacy of these treatments has been validated via analysis of histological images; see Sect. 2.2.1.

2.1.2 Opening angle experiment

Of the two ring samples acquired from each heart, after soaking in their corresponding solution (96 hours to remove the collagen fibers and myocytes) as described in Sect. 2.1.1, one was fixed for histological analysis (see Sect. 2.1.3), while an opening angle test was performed on the other. The opening angle test consists of making a radial cut through the left ventricle lateral wall in the ring slices, which led to the samples opening up as they approach a near stress-free configuration. Pictures of the samples were taken immediately before and after the radial cut and at an interval of 3 min in the first 15 min after the cut. The interval was increased to 15 min for another 75 min before the test was terminated. The total test duration was 90 min and was based on a terminating criteria that the rate of change of the opening angle is less than 0.2° / min for all samples.

The opening angle was calculated from these pictures using ImageJ [130] and a method described in Omens and Fung (1990) [103] (Fig. 2.1b). First, a centerline (Line 3–4) extending through the RV was established using the middle of the opening line (Line 1–2). Then, this line was used, along with the inner radius measured from the pre-cut pictures to locate the left ventricle center (Points 5 and 6). From this center point, two lines (Lines 6–7 and 6–8) connecting the center to either side of the cut were created. The opening angle was defined to be the angle between these two lines. On the other hand, inner and outer radii were determined by inscribing a circle on the inner and outer surface of the cut and uncut ring samples, respectively (Fig. 2.1c).

2.1.3 Histology and microstructural analysis

Histological analyses were conducted on the ring samples from each test group. Specifically, the samples were fixed in a 10% formalin solution in an unloaded state for 3 days and then stored at

room temperature in 30% ethanol before being embedded in paraffin and sectioned. Picrosirius red staining was then applied to quantify the amount of collagen (in red) and myocytes (in yellow) [4]. We also applied and imaged H&E stains to verify the integrity of the cells in the control and myocytes-only samples. On the other hand, Picrosirius red-stained samples were imaged with polarized light to confirm that the collagen was intact in the control and collagen-only samples and was degraded in the myocytes-only samples. Area fractions of the myocytes and collagen fibers were quantified at four different regions that were located 90° from each other in each sample based on hue, saturation and lightness (HSL) thresholding with custom MATLAB routines [4, 5]. The constituent's mass fraction (ϕ^c , ϕ^m) in each experimental group was taken to be the average of the computed area fractions.

Finally, we performed scanning electron microscopy (SEM) imaging on both the decellularized and collagenase-treated samples using a modified version of the protocol described in MacKenna et al. (1994) [89]. Briefly, samples were fixed at 4°C for 1–2 hours in 4% glutaraldehyde buffered with 0.1M sodium phosphate at pH 7.4. Following a brief rinse in the buffer, samples were dehydrated in an ethanol series (25, 50, 75, 95%) for 1 hour at each gradation and with three 1 hour changes in 100% ethanol. Then, samples were mounted on aluminum stubs using adhesive tabs (M.E. Taylor Engineering, Brookville, MD) and coated with 60s of Iridium (roughly 5.5 nm thickness). Finally, samples were examined in a JEOL 6610LV (tungsten hairpin emitter) scanning electron microscope (JEOL Ltd., Tokyo, Japan). The purpose of this examination was to ensure no damage to constituents that were intended to be isolated.

2.1.4 Constitutive modeling framework

An extended version of the constrained mixture modeling framework with inter-constituent mechanical interactions was developed. We refer this as the constrained mixture with inter-constituent mechanical interaction (CMMI) modeling framework.

Kinematics – The kinematics associated with the CMMI modeling framework (Fig. 2.2) was defined by the following mappings.

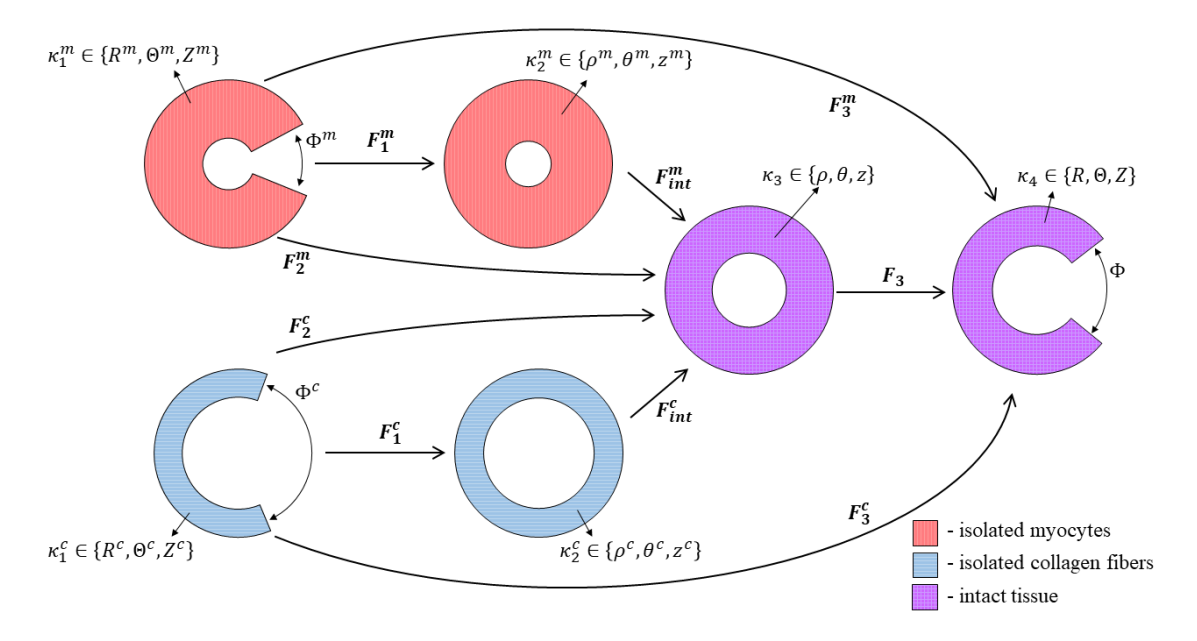


Figure 2.2: Schematic representation of the configurations of interest in the CMMI modeling framework.

1. $\kappa_1^{\xi} \to \kappa_2^{\xi}$: Maps between the cut, nearly stress-free configuration κ_1^{ξ} (with coordinates $R^{\xi}, \Theta^{\xi}, Z^{\xi}$) to the uncut, traction-free configuration κ_2^{ξ} (with coordinates $\rho^{\xi}, \theta^{\xi}, z^{\xi}$) of the myocyte-only $(\xi = m)$ and collagen-only $(\xi = c)$ tissue samples, respectively. The corresponding deformation gradient tensors are

$$\boldsymbol{F_{1}^{\xi}} = \begin{bmatrix} \frac{\partial \rho^{\xi}}{\partial R^{\xi}} & 0 & 0\\ 0 & \frac{\rho^{\xi}}{R^{\xi}} \frac{2\pi}{2\pi - \Phi^{\xi}} & 0\\ 0 & 0 & \lambda_{1}^{\xi} \end{bmatrix}, \ for \ \xi = m, c.$$
 (2.1)

2. $\kappa_2^{\xi} \to \kappa_3$: Maps between constituent-specific, uncut configurations κ_2^m and κ_2^c to the uncut, traction-free configuration of the mixture κ_3 . These maps are associated with a mechanical interaction between the constituents when combining them into a mixture. For simplicity, the deformation gradient tensors corresponding to these map were defined to be isotropic and

characterized by a prescribed interaction parameter α^{ξ} , i.e.,

$$\boldsymbol{F_{int}^{\xi}} = \alpha^{\xi} \begin{bmatrix} \frac{\partial \rho}{\partial \rho^{\xi}} & 0 & 0\\ 0 & \frac{\rho}{\rho^{\xi}} & 0\\ 0 & 0 & \lambda_{2}^{\xi} \end{bmatrix}. \tag{2.2}$$

Accordingly, the constituent ξ is stretched in the interaction when $\alpha^{\xi} > 1.00$ or is compressed in the interaction when $\alpha^{\xi} < 1.00$. On the other hand, when the myocytes and the collagen fiber network apply only negligible mechanical interaction on each other, the interactions parameters are $\alpha^m = \alpha^c = 1.00$. This specific case corresponds to the standard constrained mixture modeling framework. We also note that it is also possible to prescribe a non-homogeneous mechanical interaction where α^{ξ} depends on the radial coordinate ρ^{ξ} . To characterize such a non-homogeneous mechanical interaction will, however, require additional local measurements that are beyond the scope of our experimental setup.

3. $\kappa_3 \to \kappa_4$: A map between the mixture uncut, traction-free configuration κ_3 (with coordinates ρ, θ, z) to its cut and equilibrated configuration κ_4 (with coordinates R, Θ, Z). The corresponding deformation gradient tensor is

$$\boldsymbol{F_3} = \begin{bmatrix} \frac{\partial R}{\partial \rho} & 0 & 0\\ 0 & \frac{R}{\rho} \frac{2\pi - \Phi}{2\pi} & 0\\ 0 & 0 & \lambda_3 \end{bmatrix}. \tag{2.3}$$

By enforcing incompressibility in each kinematic mappings, the radial position of each configuration $(\kappa_1^{\xi}, \kappa_2^{\xi}, \kappa_3, \text{ and } \kappa_4)$ can be written in any of the coordinate sets.

Mechanical equilibrium conditions – Mechanical equilibrium was enforced in each of the non stress-free configurations to compute the mixture opening angle Φ with given interaction parameters α^{ξ} . To do so, Cauchy stress in each configuration was generalized as

$$t = -pI + \sum_{\xi = m, c} 2\phi^{\xi} \mathbf{F}^{\xi} \frac{\partial W^{\xi}}{\partial \mathbf{C}^{\xi}} (\mathbf{F}^{\xi})^{T}, \qquad (2.4)$$

where p is the Lagrange multiplier (for enforcing incompressibility), ϕ^{ξ} is the mass fraction for the constituents (collagen: $\xi = c$; myocytes: $\xi = m$), F^{ξ} is the mapping taken with respect to the constituent's stress-free configuration, $C = (F^{\xi})^T F^{\xi}$ is the corresponding right Cauchy–Green deformation tensor, and W^{ξ} is the prescribed strain energy density function of the constituents. Mechanical equilibrium was then enforced sequentially in each of the configurations detailed below to solve for the unknowns in the kinematic mappings.

1. κ_2^{ξ} : Force equilibrium equations in the radial and axial direction are given by

$$\int_{\rho_i^{\xi}}^{\rho_o^{\xi}} \frac{1}{\rho^{\xi}} (t_{\theta\theta}^{\xi} - t_{\rho\rho}^{\xi}) d\rho^{\xi} = 0$$
(2.5)

$$\int_{\rho_{i}^{\xi}}^{\rho_{o}^{\xi}} \rho^{\xi} [2t_{zz}^{\xi} - (t_{\theta\theta}^{\xi} + t_{\rho\rho}^{\xi})] d\rho^{\xi} = 0$$
 (2.6)

where $(t_{\rho\rho}^{\xi}, t_{\theta\theta}^{\xi}, t_{zz}^{\xi})$ are, respectively, the radial, circumferential and longitudinal components of the Cauchy stress tensor associated with the collagen-only configuration $t^{e} = t$ $(\phi^{m} = 0, \phi^{c} = 1)$ and myocyte-only configuration $t^{m} = t$ $(\phi^{m} = 1, \phi^{c} = 0)$. After substituting F_{1}^{ξ} for F^{ξ} in Eq. 2.4, these equations were solved for the internal radius R_{i}^{ξ} and axial stretch λ_{1}^{ξ} using opening angle Φ^{ξ} and closed inner and outer radius, ρ_{i}^{ξ} and ρ_{o}^{ξ} , measured experimentally in the collagen-only and myocytes-only samples. The reason for starting with experimental measurements from κ_{2}^{ξ} as the "known" geometry, then using its equilibrium to solve for the radius of κ_{1}^{ξ} is the irregularity of the open, ring-shaped samples. While we assume a perfect open ring-shape in the model, experimentally, these tend to be irregular and/or twisted shapes. Therefore, the experimental geometry of κ_{2}^{ξ} is a more reliable starting point.

2. κ_3 : Force equilibrium equations in the radial and axial direction are given by

$$\int_{\rho_i}^{\rho_o} \frac{1}{\rho} (t_{\theta\theta} - t_{\rho\rho}) d\rho = 0$$
 (2.7)

$$\int_{\rho_i}^{\rho_o} \rho [2t_{zz} - (t_{\theta\theta} + t_{\rho\rho})] d\rho = 0$$
 (2.8)

After substituting $F_2^{\xi} (=F_{int}^{\xi}F_1^{\xi})$ for F^{ξ} in Eq. 2.4, these equations, using incompressibility, were solved for the internal radius ρ_i and axial stretch λ_2^{ξ} in the uncut mixture traction-free configuration with prescribed interaction parameters α^{ξ} . In solving for these quantities, experimental measurements $(\rho_i^{\xi}, \rho_o^{\xi}, \Phi^{\xi})$ as well as quantities $(R_i^{\xi}, \lambda_1^{\xi})$ from the previous mechanical equilibrium solution of the κ_2^{ξ} configuration were used. We would like to point out that if $\alpha^{\xi} = 1$ (no mechanical interaction), then $\lambda_z = 1$, $\rho_i = \rho_i^{\xi}$, and $\rho_o = \rho_o^{\xi}$ (i.e., $F_{int}^{\xi} = I$) is the solution for this problem.

3. κ_4 : Force equilibrium equations in the radial and axial directions, as well as the bending moment equilibrium equation, are given by

$$\int_{R_i}^{R_O} \frac{1}{R} (t_{\Theta\Theta} - t_{RR}) dR = 0$$
 (2.9)

$$\int_{R_i}^{R_O} R[2t_{ZZ} - (t_{\Theta\Theta} + t_{RR})] dR = 0$$
(2.10)

$$\int_{R_i}^{R_O} Rt_{\Theta\Theta} dR = 0 \tag{2.11}$$

After substituting $F_3^{\xi} (= F_3 F_{int}^{\xi} F_1^{\xi})$ for F^{ξ} in Eq. 2.4, these equations, together with incompressibility, were solved for the internal radius, R_i , axial stretch, λ_3 , and opening angle, Φ , in the cut mixture configuration. These equations were solved using ρ_i^{ξ} , ρ_o^{ξ} , and Φ^{ξ} that were measured experimentally with R_i^{ξ} , λ_1^{ξ} , ρ_i , and λ_2^{ξ} computed from the two previous mechanical equilibrium solutions.

Constitutive relationship – Mechanical behaviors of the myocytes and collagen fibers were both prescribed by an exponential function of the first invariant of the right Cauchy–Green tensor C^{ξ} taken with respect to their natural stress-free configuration, i.e.,

$$W^{\xi} = c^{\xi} \left\{ exp\left[k^{\xi}(I_{1}(\mathbf{C}^{\xi}) - 3)\right] - 1\right\}, \ for \ \xi = m, c.$$
 (2.12)

This choice was based on previous uniaxial test measurements made on single myocyte [8], which showed that its stress–strain relationship is exponential. Our choice of using an exponential strain

Model Parameters	Experimental Measurements	Test Groups
$ ho_i^m, ho_i^c ho_o^m, ho_o^c ho_o^m, \Phi^c ho^c ho^* ho^m, \Phi^c$	Inner radius of uncut samples External radius of uncut samples Opening angle of cut samples Opening angle of cut samples Area fractions of constituents	Myocyte-only and collagen-only Myocyte-only and collagen-only Myocyte-only and collagen-only Intact tissue Intact tissue

Table 2.1: Model parameters measured from experimental data

energy function to describe the mechanical behavior of collagen fibers was, however, motivated by the observation that the fibers are wavy in the cardiac tissue [57] and has a linear stress–strain relationship upon fully straightened [131]. Collectively, the stress–strain relationship of collagen fibers having varying degree of waviness would then become exponential [64]. We also note that while the mechanical behavior of cardiac tissue is anisotropic with respect to the muscle fiber orientation that varies across the left ventricle wall, we have, as a first approximation, neglected this feature here.

Parameterization with experimental measurements – The CMMI framework was directly parameterized using geometrical and histological quantities measured in tissues with isolated collagen or myocytes $(\phi^{\xi}, \rho_i^{\xi}, \rho_o^{\xi}, \Phi^{\xi})$ as well as those from the tissue mixture (Φ^*) . A summary of the measurements used for parameterizing the framework is given in Table 2.1. Nonlinear regression was used to fit the parameters (c^c, k^c) and (c^m, k^m) in the constitutive relationship Eq. 2.12 to the previously published uniaxial mechanical test data on single myocyte [8] and isolated collagen fiber [131]. We note that strain E in the collagen fiber uniaxial test data was scaled by a straightening stretch of $\lambda_s = 1.2$ (i.e., $E \cong 12((2E+1)\lambda_s^2-1)$) to take into account of the fiber waviness found in the tissue [57]. The best-fit values were $c^c = 11090$ kPa, $c^m = 4.36$ kPa, and $k^c = 2.22$, $k^m = 3.71$, Fig. 2.3.

Types of mechanical interaction – We considered four different types of mechanical interaction, namely (a) no interaction ($\alpha^c = \alpha^m = 1.00$), (b) isotropic compression of the collagen fibers while keeping the myocytes undeformed ($\alpha^m = 1.00$, $\alpha^m < 1.00$), (c) simultaneous isotropic compression of the collagen fibers and tension of the myocytes with a constant overall volume ($\alpha^c < 1.00$, $\alpha^m = 1.00$).

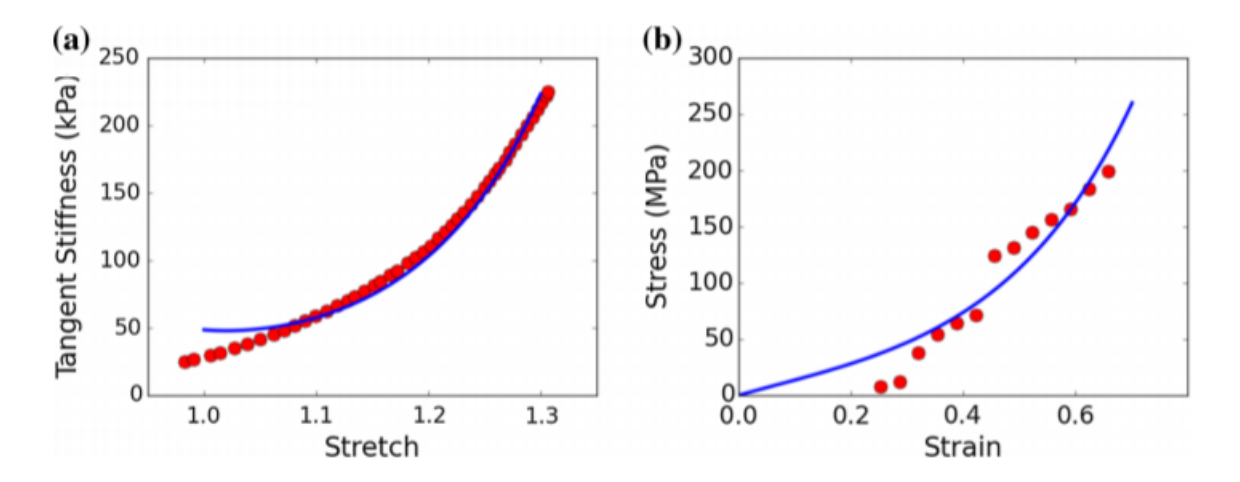


Figure 2.3: Fitting the strain energy density function parameters using uniaxial mechanical test data from (a) isolated myocyte[8] and (b) individual collagen fibril[131]. Dots: data points of the experimental measurements. Line: stress–strain relationship with the best-fit parameter values. Stress: first Piola Kirchhoff stress. Strain: Green-Lagrange strain. Tangent stiffness: $\frac{dPK1}{d\lambda}$ where λ is the stretch.

 $\frac{1}{\alpha^c} > 1.00$) and (d) isotropic compression of the myocytes ($\alpha^m < 1.00$). We note that interaction type (a) corresponds to the standard constrained mixture modeling framework, in which the collagen fibers and myocytes are not deformed when "combined" to form a mixture in the intact tissue. Correspondingly, should the standard constrained mixture modeling framework (parameterized with experimentally measured quantities) be able to reproduce the opening angle measured in the tissue mixture would suggest that any explicit inter-constituent mechanical interaction is negligible. Conversely, should the framework fail to reproduce the measured opening angle it would suggest the existence of an inter-constituent mechanical interaction that cannot be neglected when describing the mechanics of left ventricle. The opening angle of the intact tissue (Φ) is a key quantity computed from the described model. We considered the interaction parameters α^m and α^c be the "solution" when the computed opening angle in the cut, mixture configuration κ_4 assumes the value $\Phi = 57.88^\circ$ (= Φ^* , described in the following section) with a collagen mass fraction of 10% and myocyte mass fraction of 90% (measured experimentally). Appendix A describes, in detail, the steps used in solving the system and producing the geometry in κ_4 .

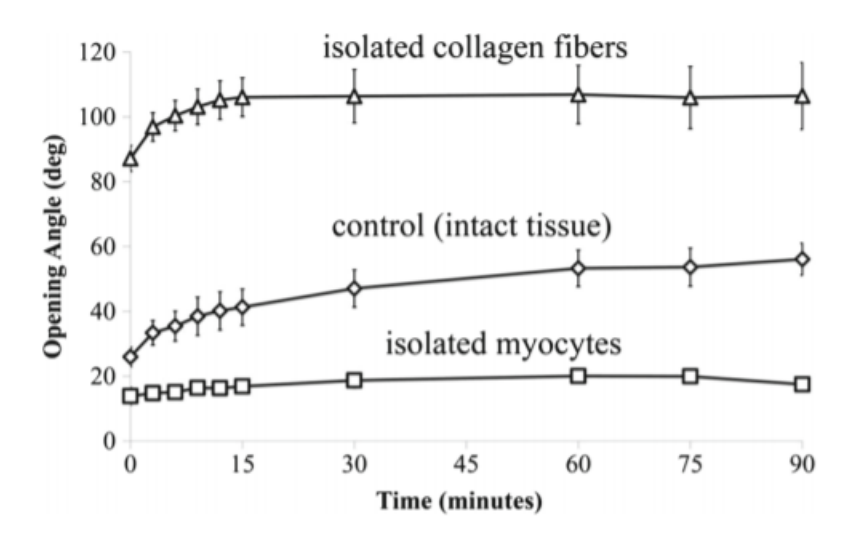


Figure 2.4: Changes in opening angle at different time points after the radial cut in the samples from male rats.

2.2 RESULTS

In this section, results of the study will be discussed in terms of the opening angle experiments, sample tissue composition, and the interaction model prediction.

2.2.1 Opening angle experiment

Our experiments showed that the opening angle increased with time and reached a steady state at about 15 min after the cut in the myocyte-only and collagen-only samples. The "control" samples took a longer time to reach steady state. Compared to the opening angle of the control samples taken from male rats ($\Phi^* = 57.88^{\circ} \pm 12.29^{\circ}$), the corresponding collagen-only samples have a larger opening angle ($\Phi^c = 106.45^{\circ} \pm 23.02^{\circ}$; p < 0.005), whereas the myocyte-only samples were found to possess a smaller opening angle ($\Phi^m = 21.00^{\circ} \pm 4.37^{\circ}$; p < 0.005), Fig. 2.4.

A similar behavior was also observed for the opening angle found in samples taken from the female rats. The only significant difference in the steady-state opening angle between the male and female rats was found in the myocyte-only group (female: $\Phi^m = 30.63^{\circ} \pm 1.50^{\circ}$ vs. male: $\Phi^m = 21.00^{\circ} \pm 4.37^{\circ}$, p < 0.005) (Fig. 2.5). Sex difference was not statistically significant in the

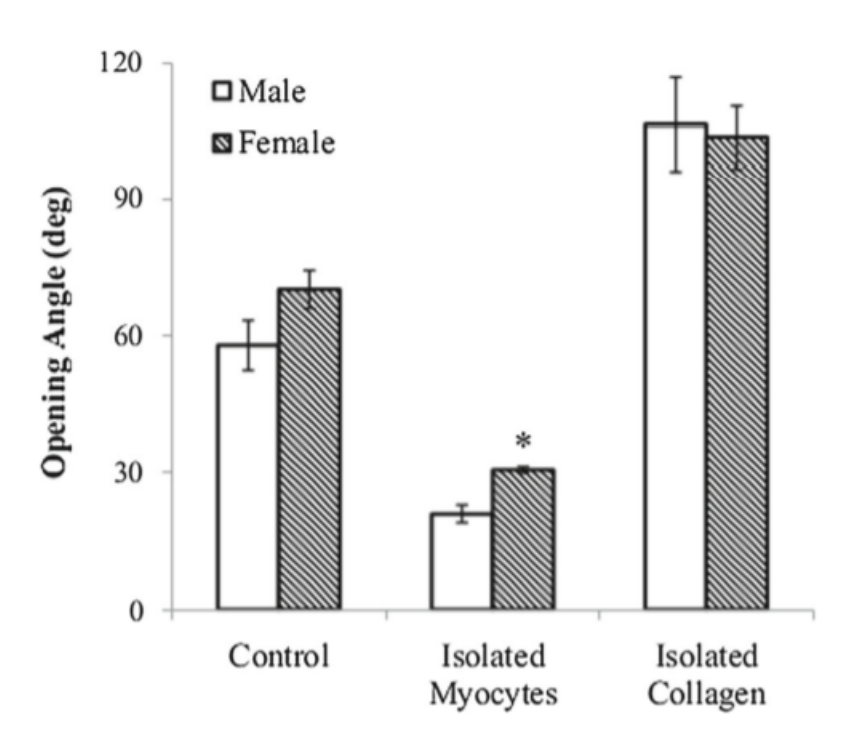


Figure 2.5: Comparison of opening angle between male and female rats.

collagen-only (female: $\Phi^c = 103.58^\circ \pm 15.43^\circ$ vs. male: $\Phi^c = 106.45^\circ \pm 23.02^\circ$) and intact tissue (female: $\Phi^* = 70.15^\circ \pm 9.30^\circ$ vs. male: $\Phi^* = 57.88^\circ \pm 12.29^\circ$) groups. These results therefore suggest that how collagen fibers and myocytes contribute to the left ventricle residual stress is not different across sex. For simplicity, results of the CMMI predictions will be discussed only in terms of the male opening angle and geometry.

2.2.2 Histology and microstructural analysis

Samples stained with Picrosirius red showed a substantial decrease in the collagen content (red) in the myocyte-only group, and myocytes (yellow) in collagen-only group when compared to the control. Specifically, collagen accounts for 3 and 10% of the total area in the myocyte-only and control group, respectively. Myocyte, on the other hand, accounts for 11 and 90% of the total area in the collagen-only and control group, respectively. Fig. 2.6 shows H&E samples and Picrosirius red under polarized light. The H&E-stained samples shows that myocytes are intact, in both control and collagenase-treated samples, while they are mostly digested in decellularized samples (Fig. 2.6,

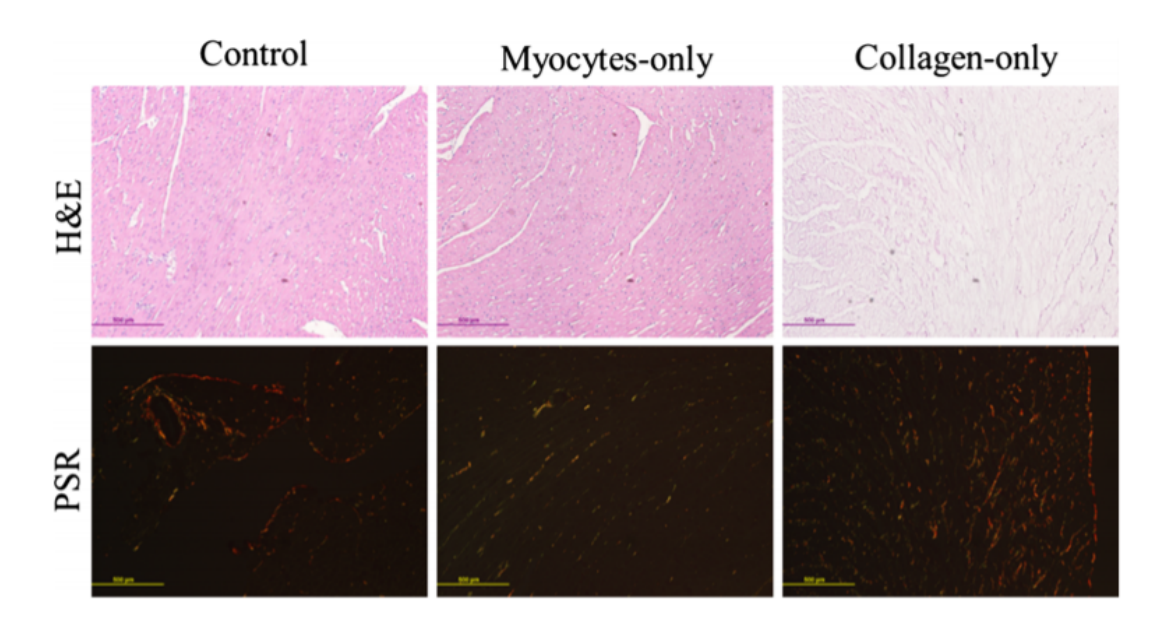


Figure 2.6: Histology images of tissue samples from the male rats hearts. Top row: H&E (nuclei in purple and cytoplasm in pink); bottom row: Picrosirius red under polarized light (collagen fibers in red, yellow and green). Left: Intact samples, center: myocytes-only samples (collagenase-treated), and right: collagen-only samples (decellularized). Bar in each image represents 500 µm.

top). The polarized light images of Picrosirius red-stained samples show intact fibers (red-yellow) in controls and decellularized samples, and degraded fibers (green-yellow) in collagenase-treated samples (Fig. 2.6, bottom). Fig. 2.7 shows the SEM images of both decellularized and collagenase-treated samples. The images confirm that the integrity of the myocytes and collagen network was not affected during collagenase treatment and decellularization, respectively.

2.2.3 Constitutive model prediction

The CMMI model was parameterized using only quantities measured in tissue samples from the male rats. The following section summarizes results from the different types of interactions discussed in the methods.

No mechanical interaction – Fig. 2.8 shows the model prediction of the mixture opening angle Φ as a function of collagen mass fraction ϕ^c without any inter-constituent interaction (i.e., $\alpha^c = \alpha^m = 1$). The model predicted an opening angle equal to that measured in the myocyte-only

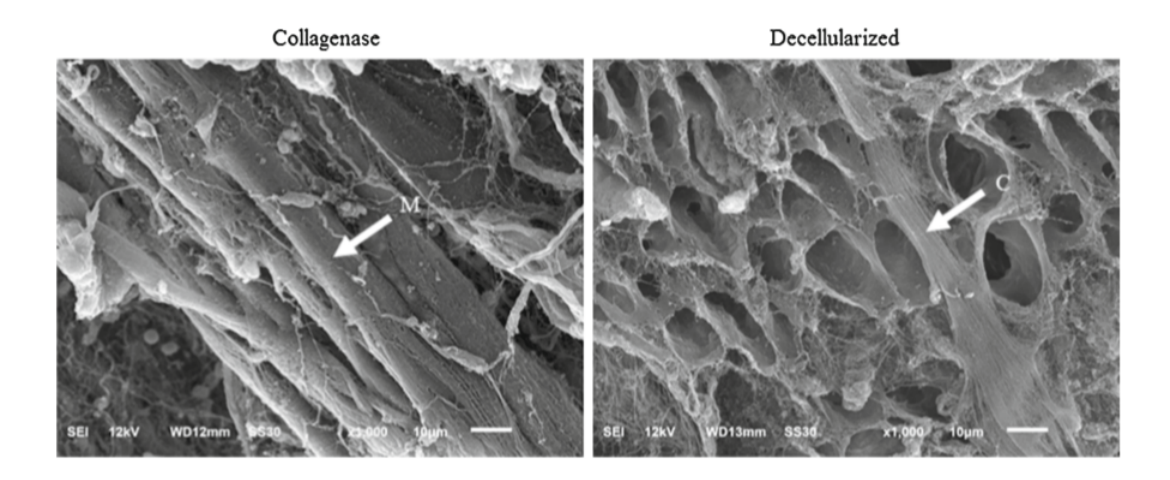


Figure 2.7: SEM images of tissue samples from the male rats hearts. Left: myocyte-only samples (collagenase-treated) and right: collagen-only samples (decellularized). Bar in each image represents $10 \, \mu m$

samples ($\Phi = \Phi^m$) when the tissue mixture does not contain any collagen ($\phi^c = 0$). At the other extreme when the mixture is composed entirely of collagen ($\phi^c = 100\%$), the predicted opening angle is equal to that measured in the collagen-only samples ($\Phi = \Phi^c$). With mass fractions ϕ^c and ϕ^m equal to the measured values (i.e., $\phi^c = 10\%$), the model predicted the tissue mixture opening angle to be 106.45° , a value that is significantly higher than the measured value (57.88°) and close to that in the collagen-only tissue samples. Only when $\phi^c = 0.06\%$ (i.e., collagen accounts for only 0.06% of the myocardium mass), did the model predict a tissue mixture opening angle equal to the measured value (i.e. $\Phi = 57.88^\circ$).

Compression of the collagen fibers only – Fig. 2.9 shows the effects on the relationship between the mixture opening angle Φ and the collagen mass fraction ϕ^c when the collagen fiber network is compressed isotropically (i.e., $\alpha^c < 1.00$) and the myocytes are undeformed ($\alpha^m = 1.00$) in the interaction. Correspondingly, when only myocytes are present ($\phi^c = 0$) in the mixture, the model predicted an opening angle equal to that measured in the myocyte-only samples (i.e., $\Phi = \Phi^m$). To recover the measured opening angle Φ^* , the values of the interaction parameters are $\alpha^c = 0.94$ and $\alpha^m = 1.00$.

Compression of collagen fibers and tension of myocytes – Fig. 2.10 shows the effects on the

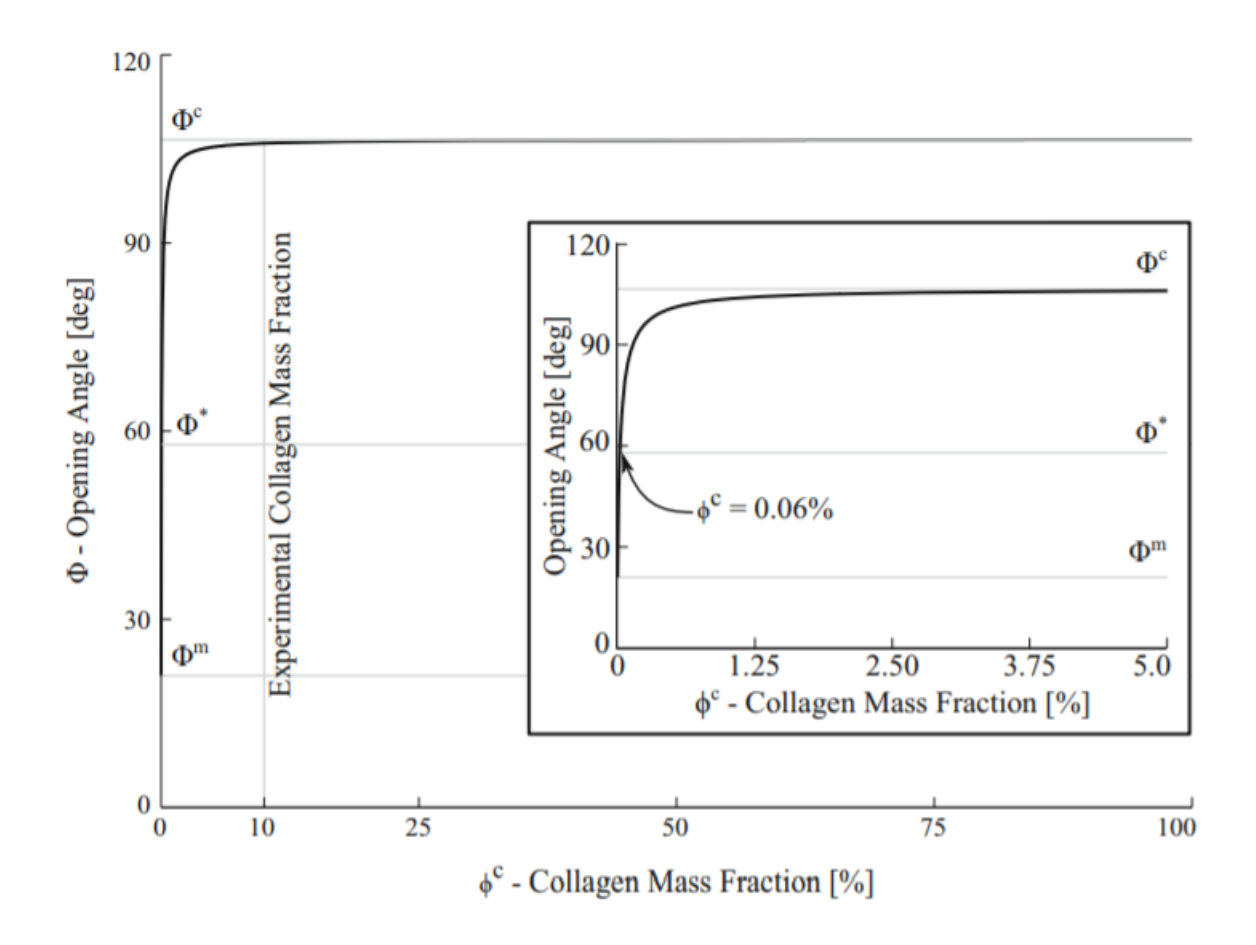


Figure 2.8: Opening angle Φ as a function of the collagen mass fraction ϕ^c without inter-constituent mechanical interaction. Φ^m , Φ^c , and Φ^* denote measured values of the opening angle for myocytes-only, collagen-only and untreated tissue, respectively. Inset: close-up view $(0 \le \phi^c \le 5\%)$ showing that the measured mixture opening angle is recovered by the model when $\phi^c = 0.06\%$.

relationship between the mixture opening angle Φ and the collagen mass fraction ϕ^c when the interaction led to an isotropic compression of the collagen fibers ($\alpha^c < 1.00$) and tension of the myocytes ($\alpha^m > 1.00$). To keep the overall mixture volume constant, the two interaction parameters were constrained by $\alpha^m \alpha^c = 1.00$. The model predicted that a mechanical interaction producing simultaneous increase in collagen fiber compression and myocyte tension will lead to a decrease in the mixture opening angle at high collagen mass fraction ϕ^c . Conversely, the mixture opening angle was increased at high myocyte mass fraction (low ϕ^c). To recover the measured opening angle Φ^* , the values of the interaction parameters are $\alpha^c = 0.89$ and $\alpha^m = 1.12$.

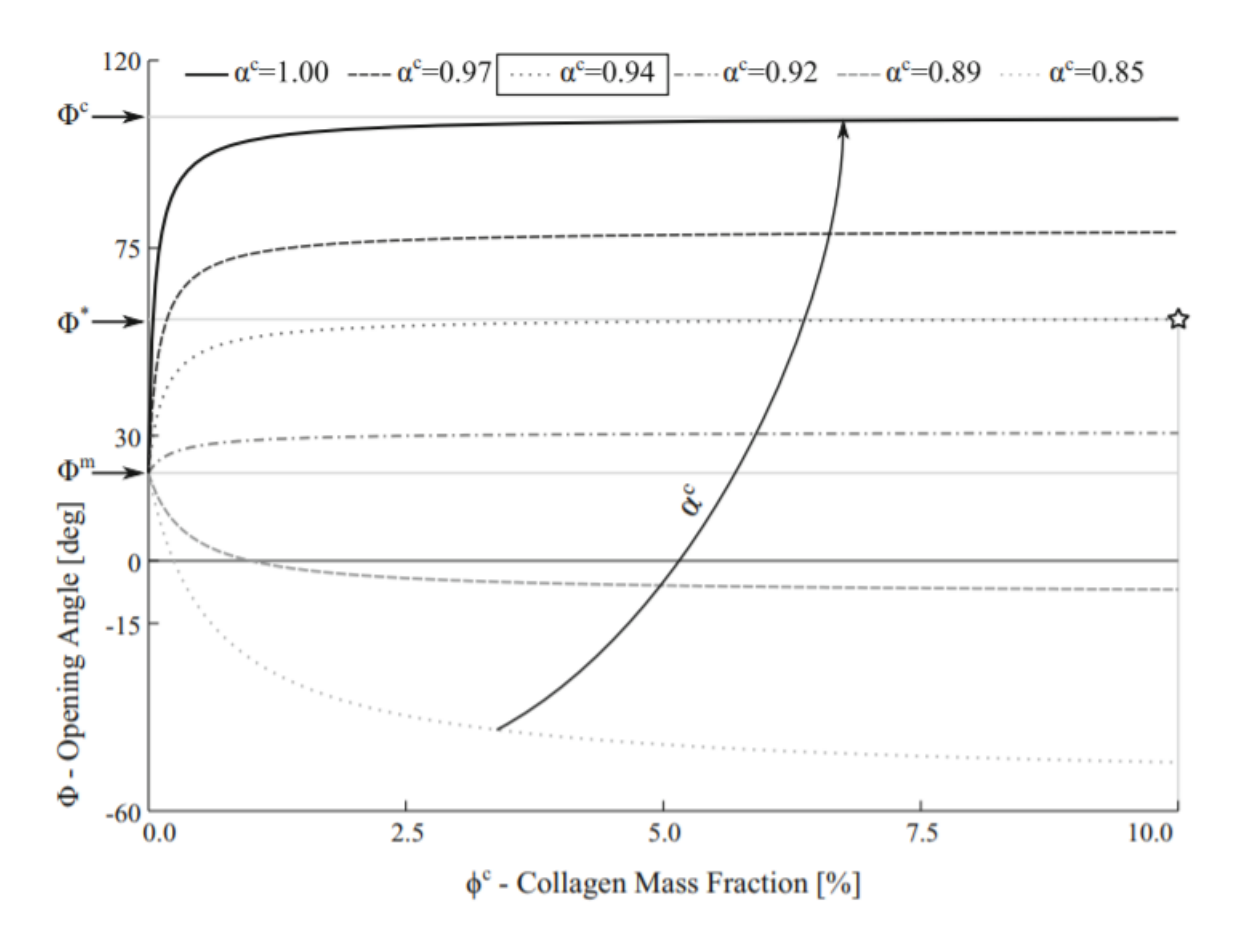


Figure 2.9: Effects of isotropic collagen compression on the mixture opening angle. Curves represent mixture opening angle Φ relationship with the collagen mass fraction ϕ^c at different compression level α^c . Φ^m , Φ^c , and Φ^* denote measured values of the opening angle for myocytes-only, collagen-only and untreated tissue, respectively. Note that the graph is truncated at $\phi^c = 10\%$ because all the curves plateau to a constant value when $\phi^c > 10\%$.

Isotropic compression of the myocytes – Fig. 2.11 shows the effects on the $\Phi - \phi^c$ relationship when the interaction led to an isotropic compression of the myocytes ($\alpha^m < 1.00$). Here, the value of α^c was found for each value of α^m so that the model recovers the measured mixture opening angle ($\Phi^* = 57.88^\circ$) at $\phi^c = 10\%$ (i.e., measured collagen mass fraction). Simply, all the curves found in this figure are solutions to the problem of finding interaction parameters that reproduces the measurements. Under this type of interaction, the model predicted that the collagen interaction parameter ϕ^c is constant at 0.94 over a wide range of myocyte compression (i.e., $\alpha^m = 1.0 - 0.4$). Only when the myocytes are severely compressed ($\alpha^m < 0.3$), did the model predict the collagen

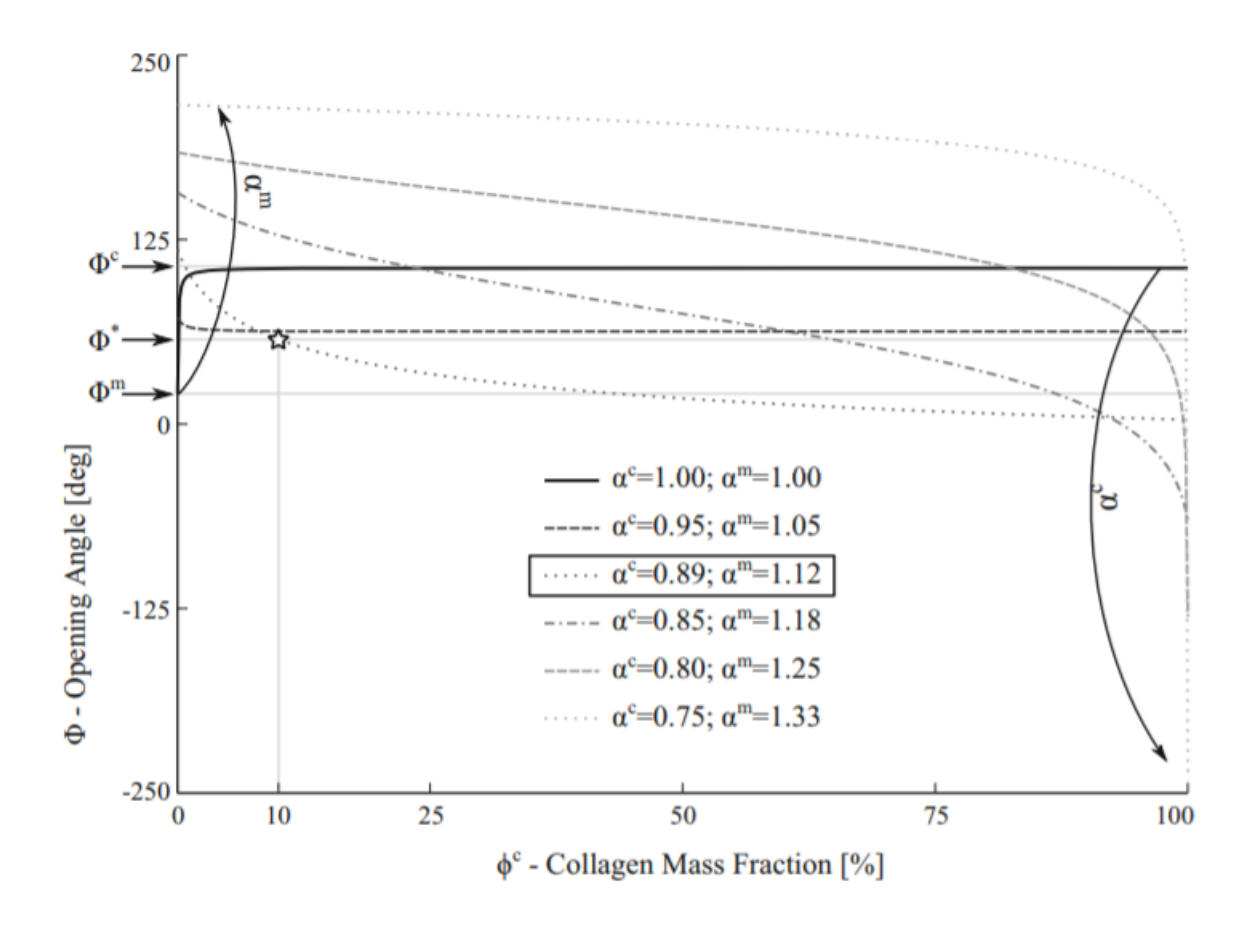


Figure 2.10: Effects of mixture opening angle caused by simultaneous collagen compression (α^c < 1.0) and myocyte tension (α^m > 1.0) in the interaction. Curves represent mixture opening angle Φ relationship with the collagen mass fraction ϕ^c with different combinations of α^c and α^m . Φ^m , Φ^c , and Φ^* denote measured values of the opening angle for myocytes-only, collagen-only and untreated tissue, respectively.

fibers to be in tension in order for the model to be consistent with the experiments.

Finally, Fig. 2.12 represents the values of the stretches in the myocytes across the wall in the intact tissue, uncut, traction-free configuration κ_3 . Black lines in the figure represent stretches in the circumferential direction, while gray lines represent stretches projected along the direction of the myocytes across the ventricular wall. The effects of the three different interactions are also represented in the figure.

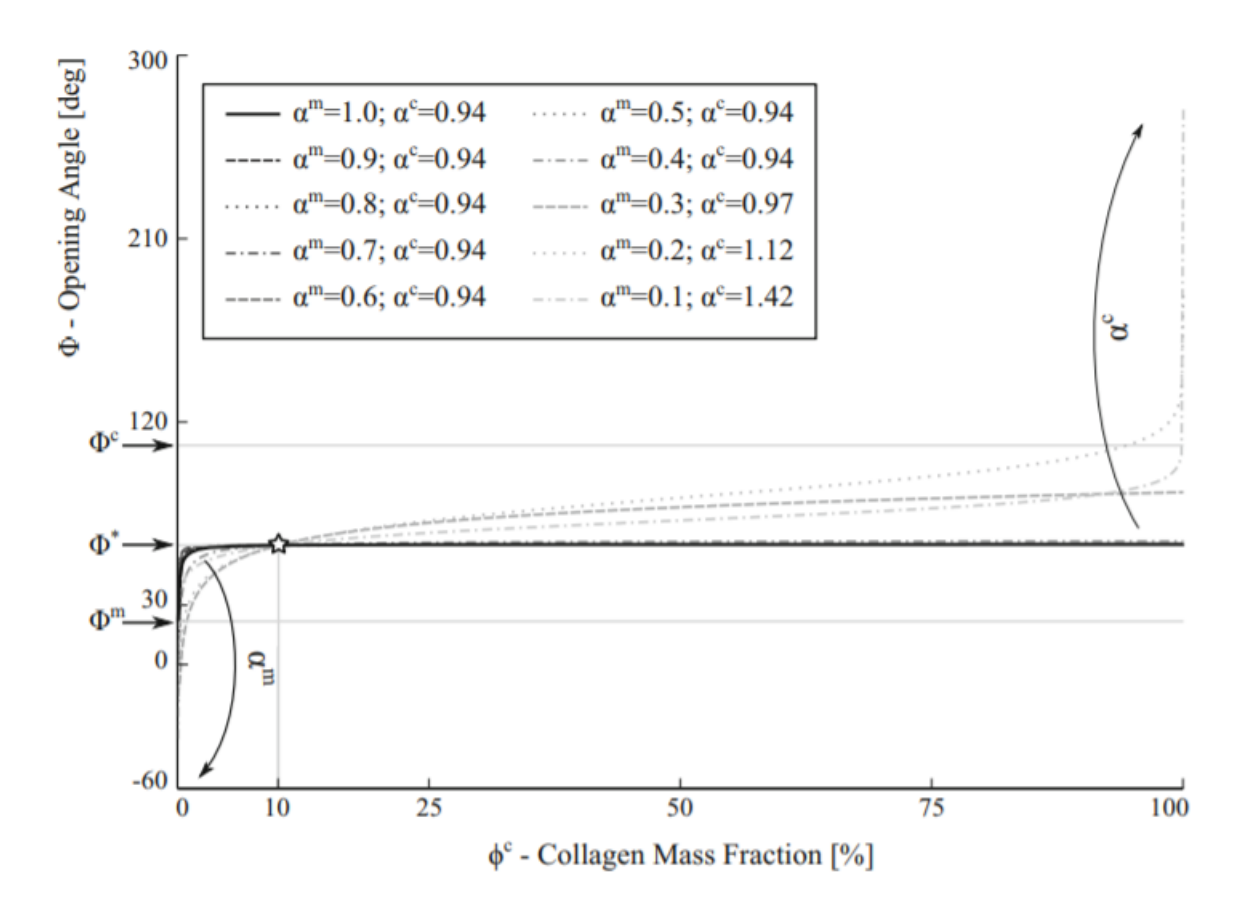


Figure 2.11: Effects of mixture opening angle caused by isotropic myocyte compression ($\alpha^m < 1.0$). Collagen interaction parameter α^c determined so that $\Phi = \Phi^*$ at $\phi^c = 10\%$. Curves represent mixture opening angle Φ relationship with the collagen mass fraction ϕ^c at different combinations of α^c and α^m .

2.3 DISCUSSION

While residual stress fields in the left ventricle have been measured across many species [108, 42, 103, 21, 136], none of these studies have, to the best of our knowledge, quantified those associated with the individual constituents of the left ventricle. Nor are there studies investigating sex difference in the residual stress fields. We have addressed these issues here. By performing opening angle experiments on tissues isolated with collagen fibers and myocytes, our results showed that the two constituents contribute disproportionately to the left ventricle residual stress fields. Measurements made on the tissue mixture containing these two constituents revealed an opening angle $\Phi^* = 57.88^{\circ}$ that is comparable to those measured in previous studies, namely Omens and

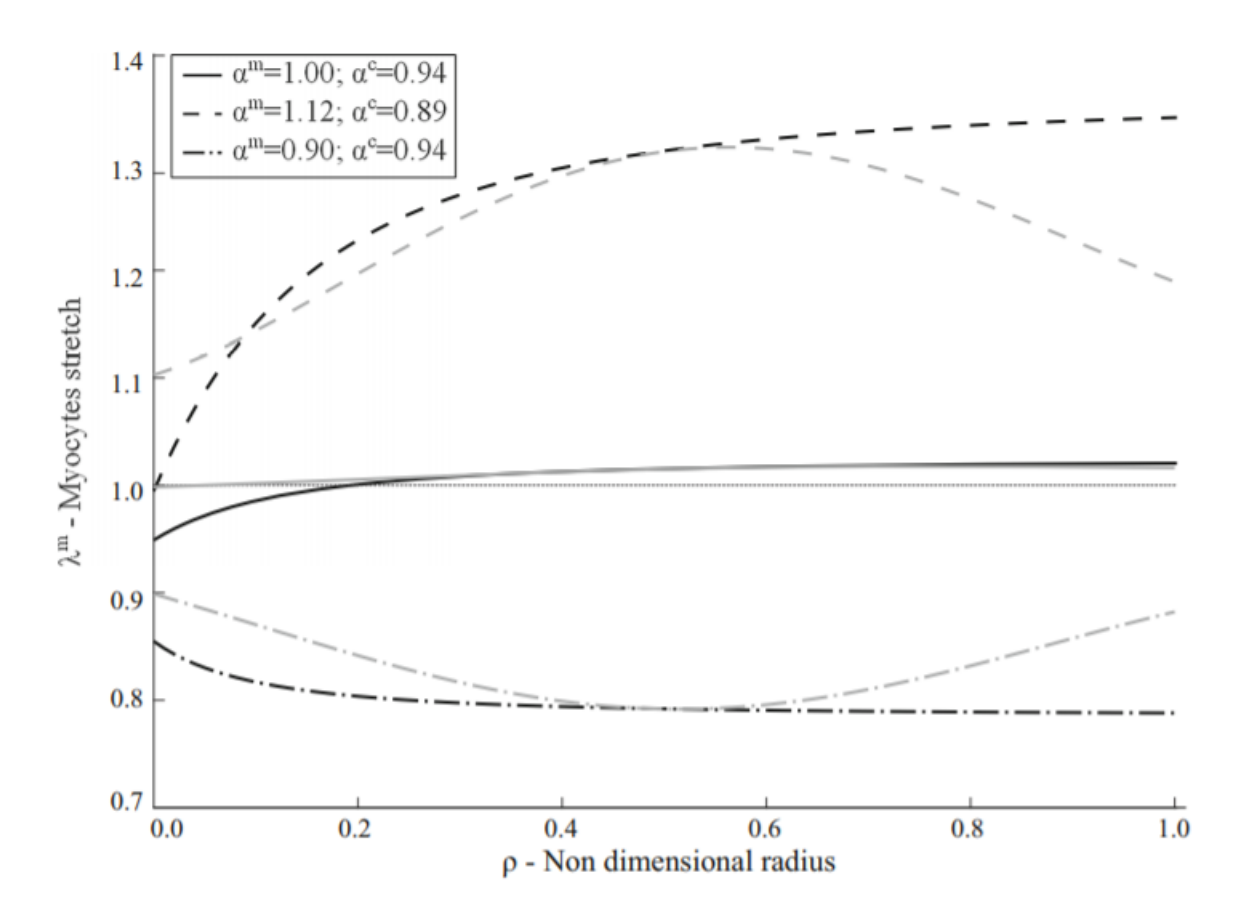


Figure 2.12: Comparison of the three different mechanical interactions considered. Myocytes and collagen interaction parameters, α^m and α^c , determined so that $\Phi = \Phi^*$ at $\phi^c = 10\%$. Curves represent myocytes stretch in the circumferential (black) and in the direction of the myocytes across the wall (gray).

Fung (1990) [103] ($\Phi^* = 45^\circ$), Omens et al. (1996) [107] ($\sim 51^\circ \pm 11^\circ$) and Rodriguez et al. (1993) [125] ($\sim 45^\circ \pm 15^\circ$). A Welch's t test was also performed and showed no significant difference between our measurements and those from the latter study ($\alpha > 0.8$). Unlike here, where we measured the opening angle over a 90-min period as it reaches a steady state, the opening angle reported in these studies was measured (without BDM in Omens and Fung 1990 [103]) within 30s of radial cutting before the onset of ischemic contracture. Given that the steady-state opening angle found here (57.88°) is well below that found under full contracture (180°) as reported in Omens and Fung (1990) [103], our measurements should correspond to a state at which the muscle is mostly relaxed.

In comparison with that found in the tissue mixture, collagen-only samples have a significantly higher opening angle, whereas myocytes-only samples have a smaller opening angle. The opening angle increased progressively with time until reaching a steady state in all experimental groups, a feature that is associated with the tissue viscoelastic behavior [153, 123]. We also note that the collagen-only tissue samples appear to be similar to that found in the hydrated cartilage tissue, which is composed of a dense elastic extracellular matrix network with fluid-filled pores. As such, we expect these samples to also possess viscoelastic behavior as exhibited in the variation of opening angle with time. Correspondingly, these results suggest that the collagen fiber network is the major contributor to the left ventricle residual stress fields, despite accounting for only about 10% of the cardiac tissue volume as estimated from the histological analyses.

Our finding that the tissue opening angle appears to be positively related to the collagen content is also compatible with those found in the arteries. First, opening angle of the arteries, which contains more collagen ($\phi^c \sim 50\%$) than the left ventricle, is substantially larger (in excess of 100°) [17]. Second, degradation of collagen using collagenase also reduces the opening angle [29] in the arteries, which is consistent with our findings.

To interpret these experimental findings further, we have developed a CMMI modeling framework that takes into account the inter-constituent mechanical interactions arising from combining the constituents into a mixture. In this framework, we introduced a mapping F_{int}^m and F_{int}^c that, respectively, represent the deformation of the myocyte and collagen when they are combined. We attribute that mapping to a mechanical interaction between the two constituents. We parameterized the CMMI model with measurements made on both untreated tissues and treated tissues with only myocytes or collagen fibers. Consequently, we showed that, without the presence of this mechanical interaction ($F_{int}^m = F_{int}^c = I$), the model predicted a significantly larger opening angle in the tissue mixture than what was measured in the experiments. To reproduce the opening angle would require a collagen mass fraction that is significantly lower than that measured here (10%) and reported previously [109, 92]. Altogether, these findings suggest that the contribution of collagen fibers and myocytes to the overall left ventricle mechanical behavior cannot be described simply by only

taking into account of the constituent's mere presence in the mixture (as in the standard constrained mixture model).

Different forms of mechanical interaction leading to the compression or tension of the collagen fibers and myocytes were investigated using the CMMI model. We showed that the form of mechanical interaction necessary for the model to be consistent with the measurements is not unique, as shown in Fig. 2.13. Specifically, consistency with the measurements can be achieved when the interaction results in a compression of the collagen fiber network and tension of the myocytes, or vice-versa. Because of the substantially higher stiffness found in the collagen fiber, however, the myocytes have to be severely compressed in the interaction (with a characteristic length < 0.3 of its pre-compressed length) for the model to be consistent with the experiments. In comparison, this consistency can be achieved with only moderate compression of the collagen fiber network. Correspondingly, our results suggest that the left ventricle mechanics is more sensitive to the interaction-induced collagen fiber deformation than that of the myocytes.

In support of the CMMI model's prediction that the collagen fibers are likely to be compressed by its interaction with the myocytes, previous studies have observed that the collagen fibers in cardiac tissues are not completely straightened (and wavy) even at physiological end-diastolic pressure [89, 106]. Moreover, a larger residual stress has also been shown to be associated with an increase in the left ventricle compliance [42], suggesting that the substantial contribution of collagen fibers to the residual stress field may aid the passive filling of left ventricle.

Moreover, given that the opening angle measured in the intact (mixture) tissue $\sim 58^{\circ} \pm 12^{\circ}$ is comparable with those found in similar studies by Omens and Fung [103] ($\sim 45^{\circ} \pm 10^{\circ}$, without ischemic contracture) and Omens et al. [107] ($\sim 51^{\circ} \pm 11^{\circ}$), we expect the transmural stretch gradient to be similar to those found in Rodriguez et al. (1993) [125]. We have also computed the transmural stretch in the muscle fiber direction, as well as in the circumferential direction. While the circumferential stretch follows an expected pattern of compression at the inner radius and tension at the outer radius, the stretch in the direction of the fibers follows a different distribution. This could be explained by choice of model description (isotropic vs orthotropic).

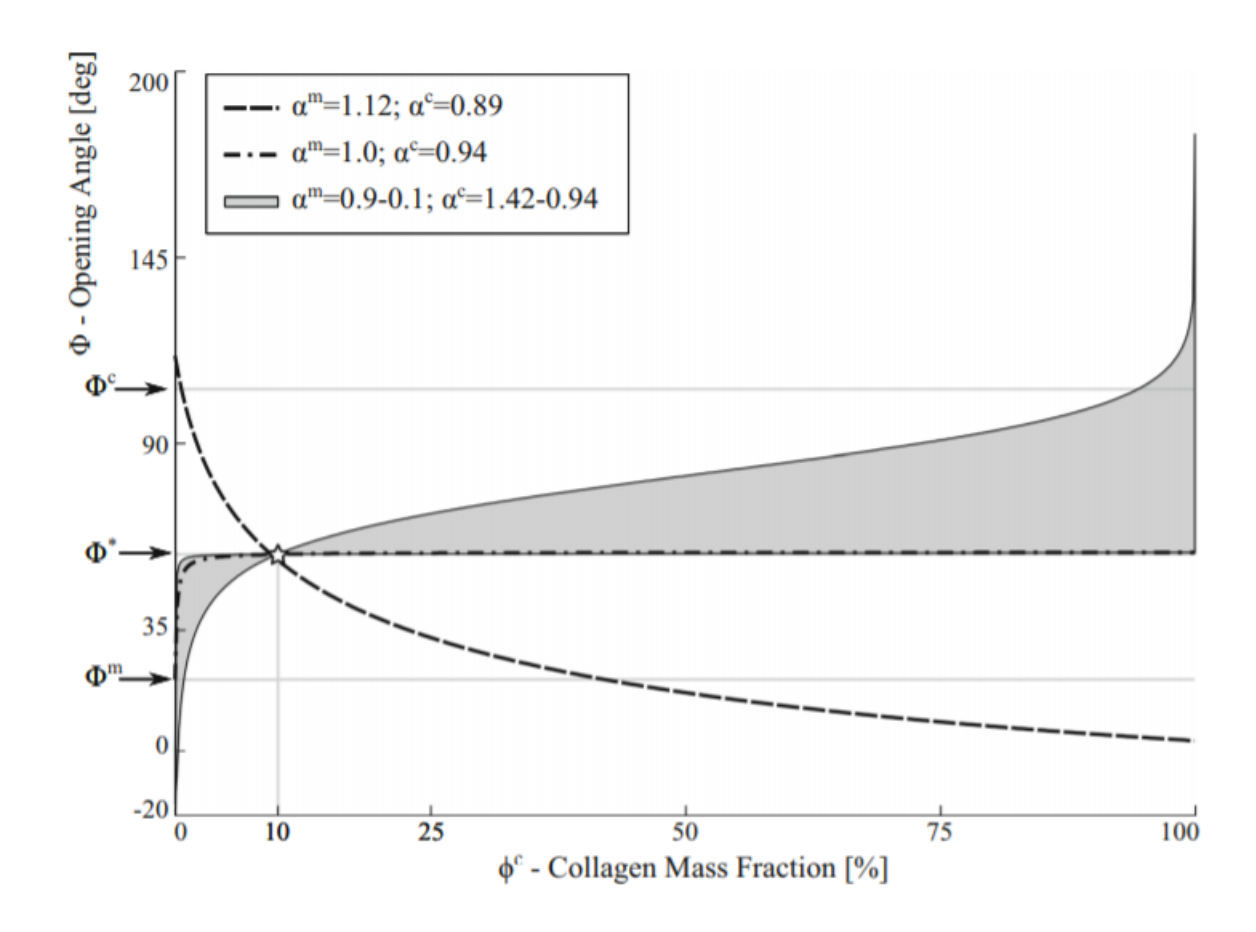


Figure 2.13: Summary of the effects of three different types of mechanical interactions on opening angle. Myocytes and collagen interaction parameters, α^m and α^c , determined so that $\Phi = \Phi^*$ at $\phi^c = 10\%$. Curves represent mixture opening angle Φ relationship with the collagen mass fraction ϕ^c at different combinations of α^c and α^m .

While the constrained mixture modeling framework has been used extensively to describe tissue mechanics in relation to its structural composition [66], this framework may be inadequate (at least where cardiac mechanics is concerned) as our finding suggests the existence of some interconstituent mechanical interactions in the left ventricle. Evidence of such mechanical interaction was also reported very recently by Avazmohammadi et al. (in 2017 [2]. Although reaching the same conclusion, that study, however, differs from ours in two aspects. First, the conclusion was reached by Avazmohammad et al. [2] based on their findings that the standard constrained mixture modeling framework was inadequate to fit the biaxial test measurements on the RV tissue. This is in contrast to our study, where the measurements of the left ventricle opening angle

form the experimental basis of our conclusion. Second, Avazmohammad et al. [2] modeled the mechanical interaction by introducing an additional "myo-collagen coupling" strain energy density function into the constrained mixture modeling framework. This differs from our proposed (CMMI) framework, in which an inter-constituent mechanical interaction mapping from the isolated constituent configuration to the mixture configuration was introduced. Despite these differences, the fact that the same conclusion was reached in two independent studies using different approaches lend support to the importance of accounting for the inter-constituent mechanical interaction in describing left ventricle mechanics.

2.3.1 Limitations

There are several limitations associated with this study. First, while it has been established previously that key features (e.g., weaves, struts and coils) of the collagen fiber network were preserved after decellularization (suggesting that it has minimal impact on the extracellular matrix's structural, functional and mechanical properties) [110], it is still possible that the collagen fibers were damaged during decellularization treatment. Similarly, the myocytes may also be damaged during collagenase treatment although it was previously established that the treatment is unlikely to do so [89].

Second, it is possible that bathing the tissue in solutions containing BDM may not prevent ischemic contracture of all the myocytes in the control and myocytes-only groups. However, the fact that the opening angle measured here in the control group is comparable to those previously measured in fully relaxed tissue [107, 103] and is also well below that found in fully contracting tissue [103] would suggest that the myocytes are mostly relaxed after treatment here.

Third, descriptors of the myocyte and collagen fiber mechanical behavior used here are highly simplified, which were characterized using previous uniaxial tension test data on isolated myocytes and individual collagen fibril. As a first approximation, we have also neglected any anisotropy of the cardiac tissue and focus primarily on the disparity in mechanical stiffness of the myocyte and collagen fiber (when straightened), which is the key contributor to our findings. Using anisotropic

constitutive laws to describe the mechanical behavior of the tissue constituents will, no doubt, increase the realism of the constrained mixture model. This will, however, not only require biaxial mechanical test results of cardiac tissues isolated with myocytes and collagen fibers, but also detailed information of the microstructural arrangement of these constituents in the tissue ring samples. Therefore, we believe that until such data become available, using the simplest possible constitutive law is the most appropriate choice here.

Last, we have assumed that the mechanical interaction deformation is isotropic and homogeneous. As a result, the form of mechanical interaction applied to the CMMI modeling framework to fit the measurements is not unique. While other forms can be prescribed in the CMMI framework, it will be fruitless to do so unless more microstructural information is available to constrain the form of interaction.

2.4 CONCLUSION

In conclusion, we have showed that the collagen fibers are key contributor to the residual stress fields found in the left ventricle of the normal rat. Our theoretical analysis on the experimental measurements also suggests the existence of some quantifiable inter-constituent mechanical interactions that must be taken into account when describing left ventricle mechanics. Whether this interaction is altered under pathological conditions will be addressed in future studies.

CHAPTER 3

LEFT VENTRICULAR GEOMETRY, TISSUE COMPOSITION, AND RESIDUAL STRESS IN HIGH FAT DIET DAHL-SALT SENSITIVE RATS

To build upon the establishment of constituent- and sex-related-differences in left ventricular residual stress in Chapter 2, we now introduce similar experimental results for a hypertensive rat model. The objectives of the following study are (1) to isolate the contribution of the collagen fiber network and the myocytes to the residual stress/strain distribution in the left ventricle wall of hypertensive Dahl-Salt sensitive rats fed with high fat diet; (2) to quantify the effect of hypertension on the left ventricle remodeling by comparing the myocardial characteristics, specifically geometry and tissue composition, of hypertensive animals to those of normotensive animals; and (3) to identify possible sex-specific features in the residual stress/strain distributions within the left ventricle wall, both in normotensive and hypertensive conditions.

3.1 METHODS

Dahl-Salt sensitive (Dahl-SS) rats, both male (M) and female (F), were fed with control fat diet (CD, 10 kcal% from fat, n = 15 M, n = 15 F) and high fat diet (HFD, 60 kcal% from fat, n = 15 M, n = 15 F) for 24 weeks starting at 3 weeks of age [1, 32]. All animal protocols used in this study were approved by MSU Institutional Animal Care and Use Committee.

3.1.1 Sample preparation

In the terminal study, the whole heart was isolated and we obtained two ring-shaped samples that exposed the left ventricle and the right ventricle by performing three lateral cuts. Of the two samples obtained from each heart, we fixed one for histological analysis and used the other for tissue constituents' isolation and then an OA test. The samples were divided equally into 3 groups: intact tissue, isolated collagen fibers, and isolated myocytes. To isolate the constituents, we followed previously published protocols [51], described in Chapter 2. To prevent active muscle contraction

while testing, both the isolated myocytes and intact tissue groups were soaked in a Krebs buffer containing 2,3-butanediome monoxime (BDM, myosin inhibitor) for 45 minutes prior and for the duration of the OA experiments [54]. After treatment and before the OA test, we obtained pictures of each sample to measure the outer diameter and thickness.

3.1.2 Histology and microstructural analysis

Samples were fixed in formalin (10% solution) for 72 hours and stored in a 30% ethanol solution until they were embedded in paraffin wax. The samples were then sectioned and stained with Picrosirius red (PSR) staining to highlight collagen fibers. After imaging (performed with a Nikon Eclipse 80i microscope with 10x magnification; n = 2 for each group), we evaluated the collagen area fraction (CAF) using a custom Matlab code.

3.1.3 Opening angle experiment

Following the procedure described in Chapter 2 [51], a radial cut was first applied through the left ventricle's wall (opposite to the right ventricle). Thereafter, pictures of the sample were taken for a period of 90 minutes. The OA was quantified by analyzing the images (using ImageJ) following a graphic procedure reported in Chapter 2 [51].

3.1.4 Mechanical testing

An additional set of left ventricles of male and female Dahl-SS rats (fed either with HFD or CD) as well as male and female Sprague Dawley rats were mechanically tested. First, we obtained two ring-shaped samples from each heart. Second, we divided the samples into two groups: isolated collagen and isolated myocytes (isolation protocols are specified in the Tissue preparation section). Third, the samples were mounted on a uniaxial tensile tester using two loops of suture (the bottom suture tied to a rigid clamp and the top suture attached to a 250g capacity load cell, LSB200, Futek), submerged in a bath with a Krebs buffer containing 2,3-BDM [54], and subjected to the following mechanical test protocol: 5% stretch for 10 cycles (preconditioning), 10% stretch for 5 cycles, 20%

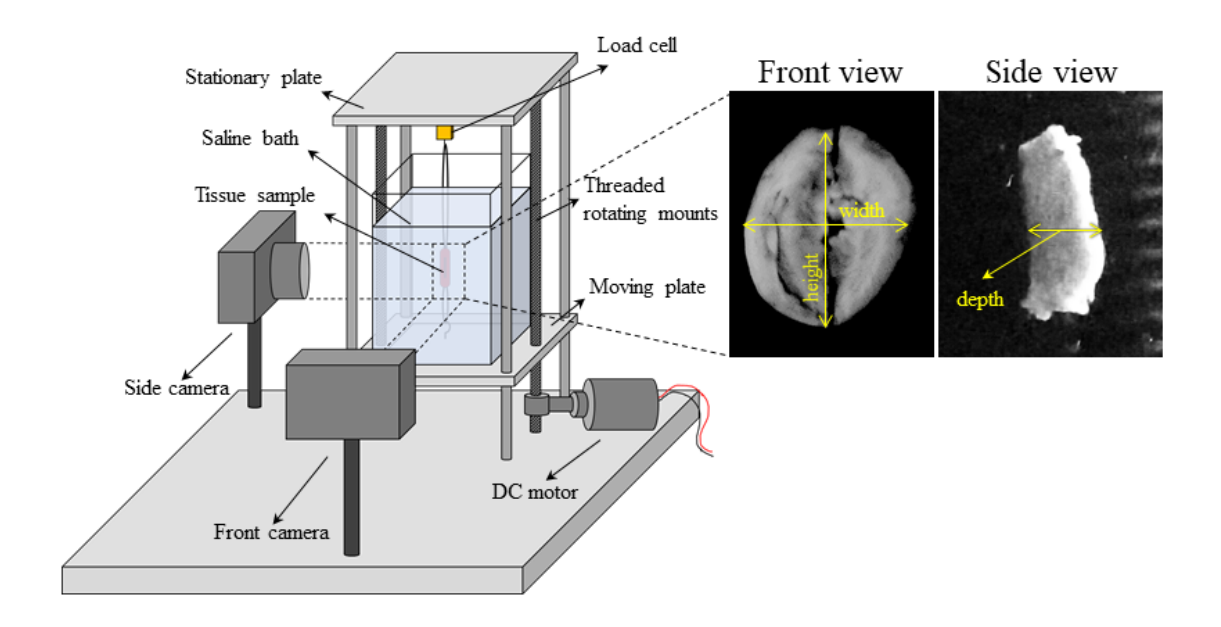


Figure 3.1: Schematic of mechanical testing set-up. Isolated myocytes from Sprague Dawley rat left ventricle used for illustrative purposes.

stretch for 5 cycles, and 30% stretch for 5 cycles. All loading was applied at a speed of 0.15 mm/s; the movement and all measurements (from the load cell and a Hitachi KP-M2A camera mounted in front of the sample) were all controlled simultaneously through LabView. A schematic of this experimental set-up can be seen in Fig. 3.1. To calculate the stress of the sample, pictures were taken before each set of cycles of the front (Hitachi camera) and side (1.6MP Android camera) of the sample to measure the width and depth (Fig. 3.1) used to estimate the initial cross-sectional area. Under an assumption of incompressibility, the width and depths would each change throughout the test with respect to $\frac{1}{\sqrt{\lambda}}$, where λ is the uniaxial stretch measured by the front-facing camera.

After testing, we evaluated the Cauchy stress and stretch from the axial force (load cell output) and the elongation data (Hitachi camera output) recorded during the last loading curve of the protocol. Fig. 3.2 shows the experimental values of Cauchy stress – stretch for a set of representative samples (symbols in the Figure represent collected data). These representative samples were males from each test group. The sample was considered incompressible, and the initial geometrical characteristics were evaluated from pictures of the side- and front-view of the sample before each

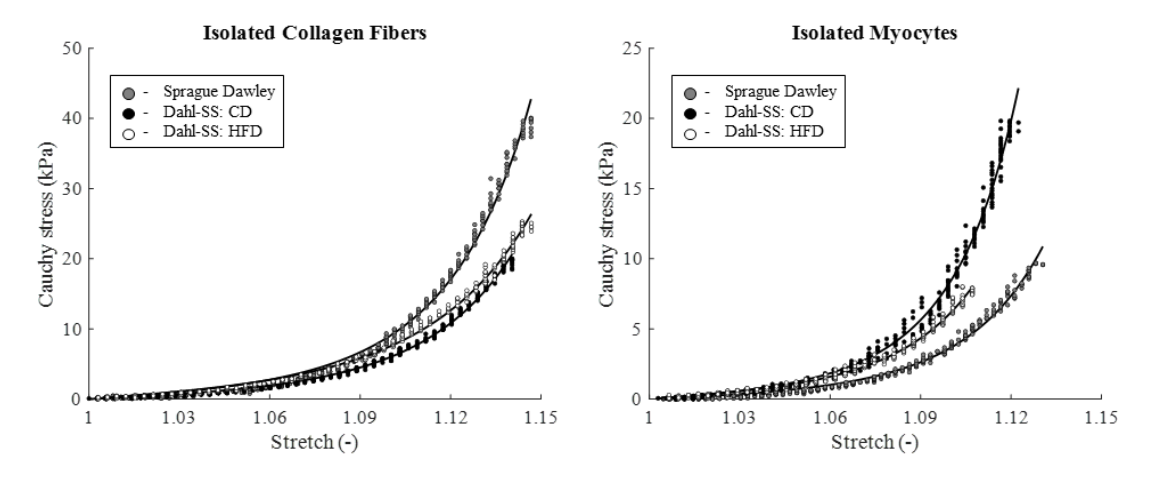


Figure 3.2: Cauchy stress vs. stretch experimental dataset (symbols) and model best-fit description (lines).

set of loading cycles.

3.1.5 Stress and stretch analysis

Constitutive modeling framework - We then used an isotropic, exponential strain energy function [26, 24] to describe the mechanical behavior of each isolated constituent, namely $W_c(C)$ for isolated collagen and $W_m(C)$ for isolated myocytes, given as

$$W_c = c_c [e^{k_C(I_1(C)-3)} - 1], \ W_m = c_m [e^{k_m(I_1(C)-3)} - 1]$$
(3.1)

where c_c and c_m are material parameters with the dimension of a stress, and k_c and k_m are dimensionless material parameters; C is the right Cauchy-Green tensor, defined as $C = F^T F$, and $F = diag[\lambda, \frac{1}{\sqrt{\lambda}}, \frac{1}{\sqrt{\lambda}}]$ is the deformation gradient tensor associated with the uniaxial tensile test with λ being the stretch in the direction of loading (i.e., circumferential direction). Material parameters were estimated by using the *lsqnonlin* function of Matlab to minimize the normalized root mean square deviation (NRMSD) between the experimental (t_{exp}) and theoretical (t_{th}) values of the Cauchy stress for each value of the applied stretch [12], defined as

$$NRMSD = \frac{1}{t_{exp}^{max}} \sqrt{\frac{\sum_{i=1}^{N} (t_{exp}^{i} - t_{th}^{i})^{2}}{N}}$$
(3.2)

where N is the number of experimental datapoints collected and t_{exp}^{max} is the maximum value of Cauchy stress reached for each sample during the mechanical test. We obtained eight sets of parameters: one for isolated collagen and one for isolated myocytes, for both male and female, for Sprague Dawley and for Dahl-SS animals. Values of the material parameters for each group are shown (as avg. +/- st.dev.) in Table 3.1. The mean values of material parameters for each group are then employed in the residual stress analysis. In full, the experimental groups in this section were (a) isolated collagen from Sprague Dawley rats (n=3 male, n=2 female) and Dahl-SS rats (males, n=2 HFD and n=2 CD; females n=2 HFD and n=2 CD), and (b) isolated myocytes from Sprague Dawley rats (n=3 male, n=3 female), and Dahl-SS rats (male: n=2 HFD and n=2 CD; female: n=2 HFD and n=2 CD). Due to the low statistical power of this portion of the study, we will not comment on differences in material parameters between the groups. In addition, the limited availability of Dahl-SS animals on each diet, allowed us to test mechanically only a low number of animals on CD (2 males and 2 females) and HFD (2 males and 2 females). For this reason, we employed the average of material parameters between diets for each male and female animal in the current study. This is a limitation of the study. To limit the impact of this limitation on the meaningfulness of this analysis we will report results for both stress and stretch residual stress fields (see Results section). Finally, the strain energy function of the intact tissue was described by the weighted averaged of the constituents as

$$W_{intact}(\mathbf{C}) = \phi_c W_c(\mathbf{C}) + \phi_c W_m(\mathbf{C})$$
(3.3)

where ϕ_c and ϕ_m represent the area fractions of the collagen (CAF) and myocytes ($\phi_m = 1 - \phi_c$) evaluated in the intact tissue (see Histology section). Note that from Eq. 3.3, one can recover the isolated collagen fibers strain energy function when $\phi_c = 1$ and $\phi_m = 0$ and the isolated myocytes strain energy function when $\phi_c = 0$ and $\phi_m = 1$.

Residual stress modeling - We used the continuum mechanics theory of large deformation to model the residual stresses in the left ventricle [51, 99, 108, 67]. For each sample, we have evaluated the Cauchy stress across the wall as

$$t_{\alpha} = -p_{\alpha} \mathbf{I} + 2\mathbf{F} \frac{\partial W_{\alpha}(\mathbf{C})}{\partial \mathbf{C}} \mathbf{F}^{T}$$
(3.4)

Group:	c _c (kPa)	k _c (-)	c _m (kPa)	k _m (-)
SD Male	0.465 ± 0.225	31.09 ± 4.09	0.051 ± 0.031	36.26 ± 13.73
SD Female	0.492 ± 0.312	32.83 ± 4.18	0.047 ± 0.011	38.67 ± 9.33
Dahl-SS Male	0.091 ± 0.060	30.17 ± 5.55	0.054 ± 0.012	43.08 ± 19.90
Dahl-SS Female	0.326 ± 0.325	32.75 ± 4.92	0.064 ± 0.016	31.23 ± 8.20

Table 3.1: Best-fit material parameters values estimated for the model presented in Equation 3.1 for each group (avg. \pm st.dev).

where W_{α} is the appropriate strain energy function (with $\alpha = c$, m, or *intact*; see Equations 3.1 and 3.3), p_{α} is a Lagrange multiplier used to enforce incompressibility, and F and C are the deformation gradient and the right Cauchy-Green deformation tensor representing the mapping from the stress-free, cut configuration (coordinates R, Θ, Z) to the load-free, closed configuration (coordinates R, Θ, Z). Specifically, for each sample, R is written as

$$\boldsymbol{F} = \begin{bmatrix} \frac{\partial \rho}{\partial R} & 0 & 0\\ 0 & \frac{\rho}{R} \frac{2\pi}{2\pi - \Phi} & 0\\ 0 & 0 & \Lambda_z \end{bmatrix}$$
(3.5)

where Φ represents the opening angle for each sample.

In order to calculate the Cauchy stress distribution across the wall given by Eq. 3.4, we used each sample's individual geometry from the open configuration (R_i, R_o, Φ) , along with their pooled material properties (c_c, k_c, c_m, k_m) and constituent area fractions (ϕ_c, ϕ_m) . It should be noted that when using Eq. 3.3 for intact tissue, ϕ_c and ϕ_m were equal to their experimental values. For each sample, the inner and outer radii and axial stretch of the closed, load-free configuration $(\rho_i, \rho_o, \text{ and } \Lambda_z)$ were estimated by using the deformation gradient in Eq. 3.5 and allowing the closed configuration to reach radial and axial equilibrium (using the *lsqnonlin* function on Matlab)—i.e.,

$$\int_{\rho_i}^{\rho_o} \frac{1}{\rho} (t_{\theta\theta} - t_{\rho\rho}) d\rho = 0, \tag{3.6}$$

$$\int_{\rho_i}^{\rho_o} \rho \left[2t_{zz} - (t_{\theta\theta} + t_{\rho\rho}) \right] d\rho = 0 \tag{3.7}$$

Additionally, an assumption of incompressibility was made for Eq. 3.5, resulting in a third equation used to solve for the unknown geometry:

$$\rho_o = \sqrt{\rho_i^2 + \frac{1}{\Lambda_z} \frac{2\pi}{2\pi - \Phi} (R_o^2 - R_i^2)}$$
 (3.8)

Lastly, for each sample, we had individual geometry measurements (R_i , R_o , Φ , ρ_i , ρ_o , Λ_z), pooled material properties from their breed and sex (c_c , k_c , c_m , k_m), and collagen and myocytes area fractions (ϕ_c , ϕ_m) for the intact tissue, measured for each breed, sex, and diet (i.e. HFD or CD). Using all of this information, we were able to calculate the radial, circumferential, and axial stresses for each group as functions of their non-dimensional radii.

Finally, in order to draw comparisons between groups, we have identified a subset of characteristic points on the transmural distribution of stress and stretch across the wall, which can be seen in Fig. 3.3 and Fig. 3.4, respectively. Specifically, we calculated the minimum value of the radial stress/stretch (maximum compression) and its normalized location across the radius; the maximum (maximum tension, at the outer radius) and minimum (maximum compression, at the inner radius) values of the circumferential and axial stresses/stretches, as well as the normalized location across the wall of the circumferential and axial neutral axes.

3.2 RESULTS

As previously reported [1, 32], Dahl-SS rats fed with HFD for 24 weeks have a significantly higher body weight and mean arterial pressure (MAP) as measured by the tail-cuff plethysmography method (MAP, 155 ± 4.7 mmHg for M; 162 ± 5.7 mmHg for F) when compared to their counterparts that were fed with a CD (MAP of 124 ± 5.6 mmHg for M; 142 ± 8.1 for F) for both sexes. It is important to note that, while the CD animals have significantly lower MAP compared to HFD, their arterial pressure is still considered to be above the hypertension threshold (MAP ~ 106 mmHg30). For this reason, we will also compare our results to those collected previously from normotensive (NT) Sprague Dawley rats [51] (MAP: 105 ± 3.3 mmHg31). While we are aware that to compare different animal strains is not ideal, we believe that it is important to establish a baseline for NT animals, as reported in previous studies [45, 50].

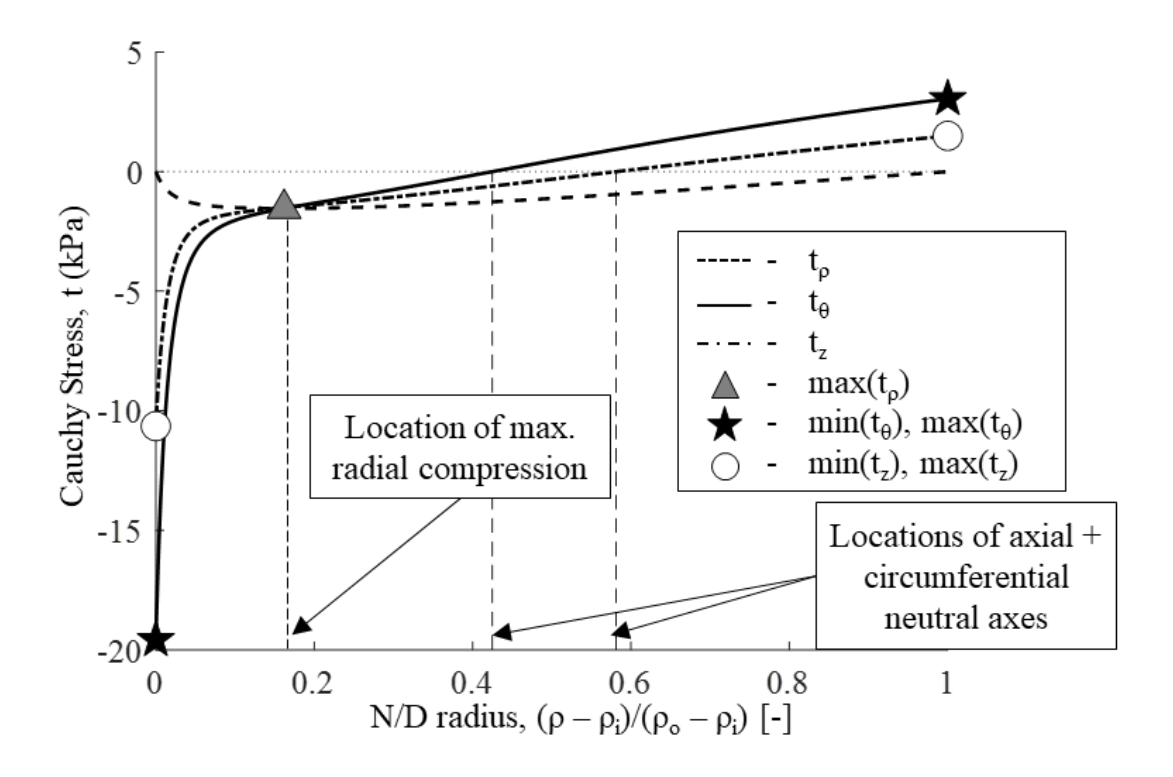


Figure 3.3: Transmural residual stress distribution for one representative sample, showing stress points of interest.

Fig. 3.5 shows the geometric characteristics indexed by the left ventricle cross-sectional area for the animal groups considered. Overall, left ventricles in the HFD group have a larger cross-sectional area compared to the CD for both sexes and all tissue treatments (difference not significant for isolated myocytes and isolated collagen fibers in M, and for intact tissue in F). The female left ventricles are also smaller than their male counterpart (difference not significant for isolated myocytes and isolated collagen fibers for HFD and for isolated collagen fibers in CD). When compared to NT animals, both HFD and CD animals have larger cross-sectional areas.

3.2.1 Histology and microstructural analysis

Fig. 3.6(a-f) shows images of histological slides stained with PSR for representative samples. Fig. 3.6(g) shows the values of collagen area fraction (CAF) for each group; we observe no difference in CAF when comparing CD to HFD and male to female. When comparing the hypertensive animals

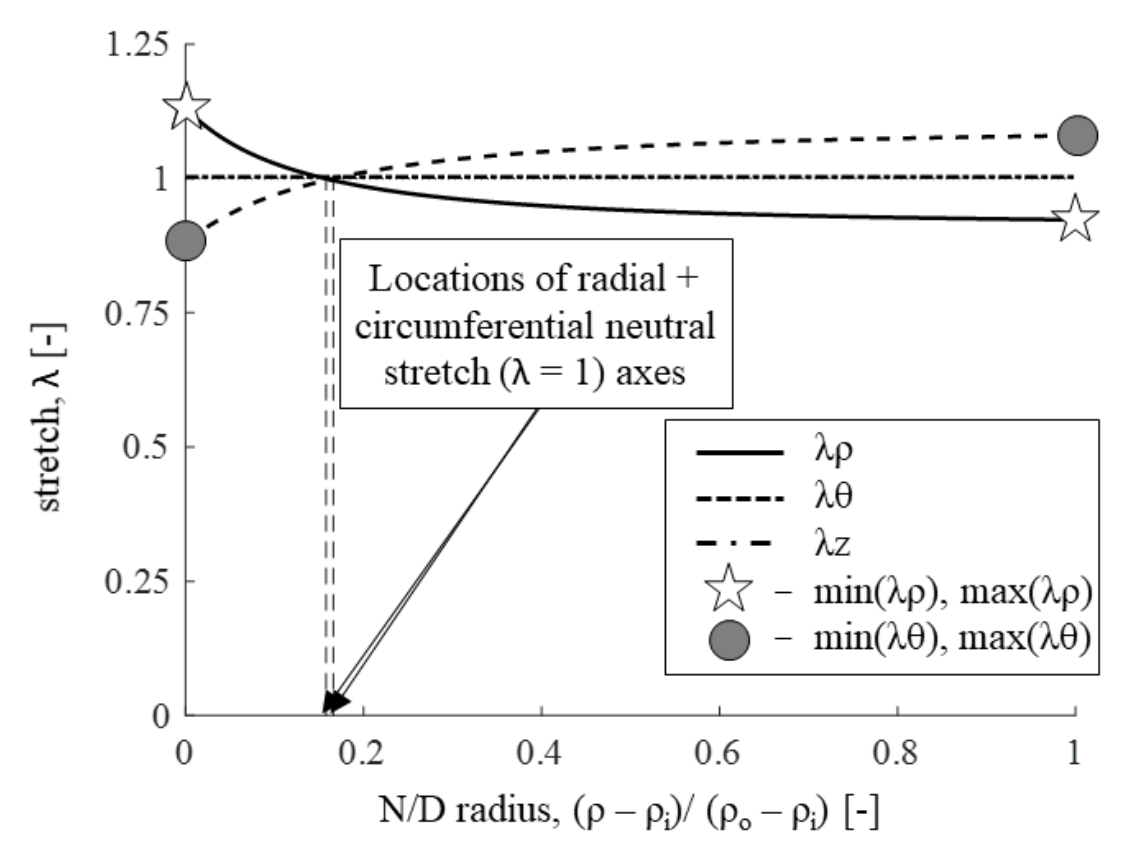


Figure 3.4: Transmural residual stretch distribution for one representative sample, showing stretch points of interest. Note: while the axial stretch assumes in most cases values close to 1, no plain strain assumption was made.

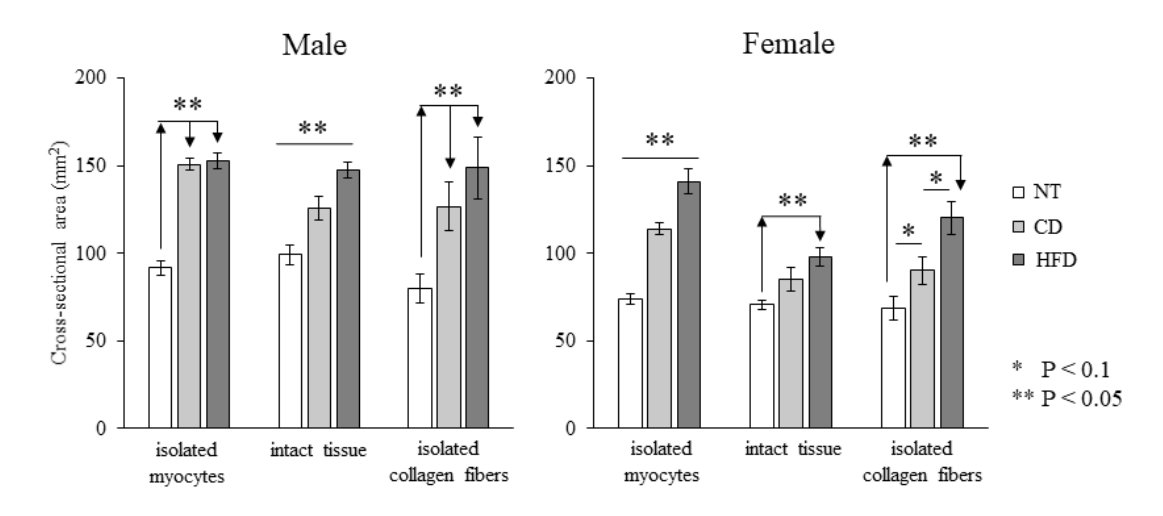


Figure 3.5: Cross-sectional area evaluated for all samples (avg. \pm st. err.).

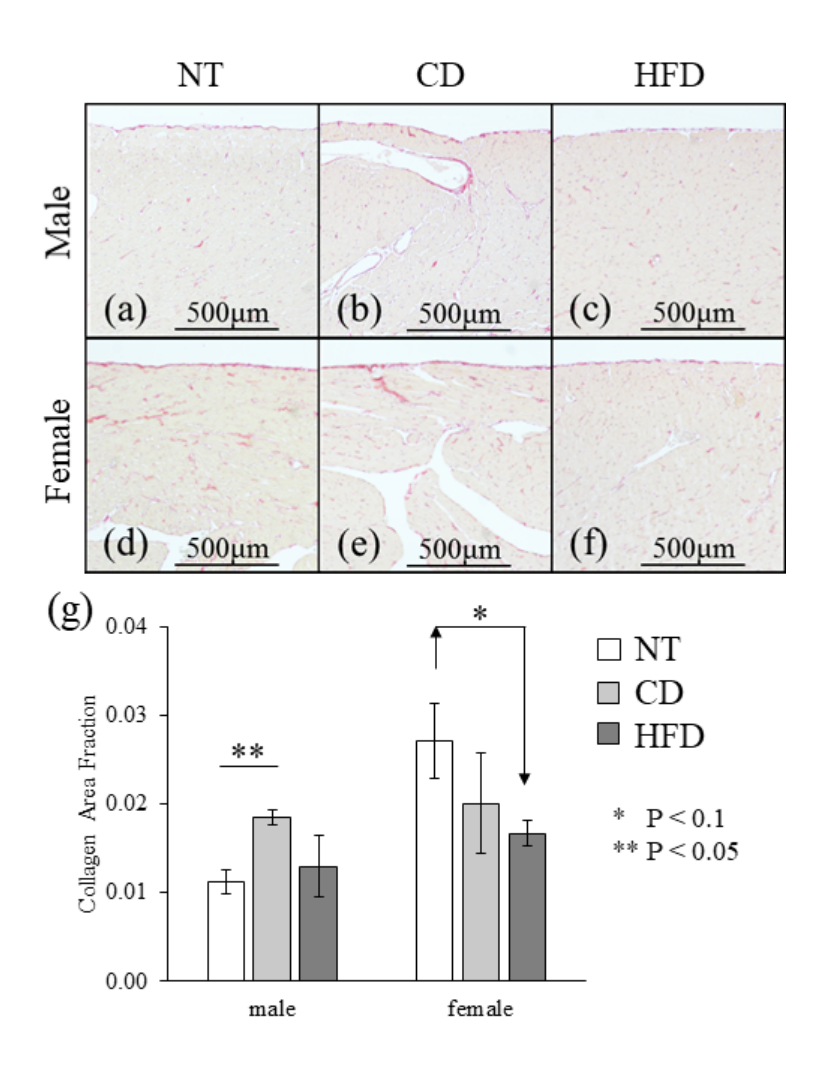


Figure 3.6: (a-f) Images of picrosirius red stained slides of male (a-c) and female (d-f) left ventricle (a, d: NT; b, e: CD; c, f: HFD). (g) Collagen area fraction evaluated for all samples (avg. ± st. err.).

(CD + HFD) to NT animals, we also observe no significant difference in CAF. Male CD samples, however, have a higher CAF when compared to NT males, whereas female HFD samples have a lower CAF compared to those from the corresponding NT group. Finally, female NT samples have a higher CAF when compared to those from their male counterpart.

3.2.2 Opening angle experiment

We report the OA results collected for all groups at the 90 min mark, motivated by the results reported in [51]. As shown in Fig. 3.7a, the OA for isolated collagen fibers is highest, followed by

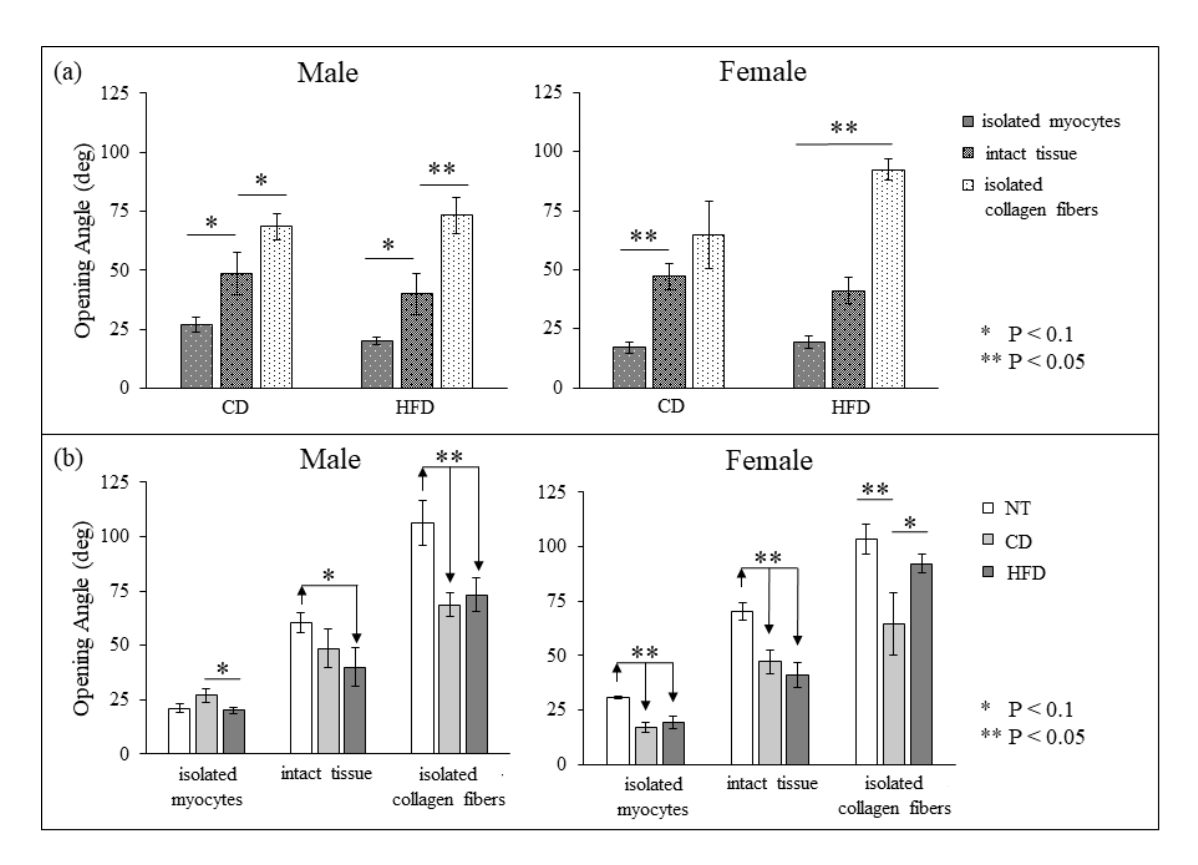


Figure 3.7: Opening angle (deg) measured for all samples (avg. \pm st. err.). (a) Comparison between isolated myocytes, isolated collagen fibers, and intact tissue for both CD and HFD. (b) Comparison between CD and HFD (also included data for NT).

that of the intact tissue, and that of the isolated myocytes for both sexes and both diets (difference not significant for intact tissue vs isolated collagen in CD F), similar to that reported in NT animals [51]. Comparison of the OA between CD and HFD groups in Figure 3.7b reveals that the OA is similar for intact tissues in both sexes, but HFD males have a lower OA compared to CD males in isolated myocytes (value is unchanged in females) and HFD females have a higher OA when compared to CD females in isolated collagen fibers (value is unchanged in males). Comparing these results to that of the NT animals reveals that increased MAP could lead to a decrease in the OA in the intact tissue, isolated collagen fibers, and isolated myocytes.

3.2.3 Stress and stretch analysis

Consistently with what is observed for the OA's values, the stress and stretch analyses show overall higher residual stresses/stretches in the isolated collagen fibers and lower stresses/stretches in the isolated myocytes when compared to intact tissue for all quantities' components considered (see Fig. 3.3 and 3.4 for definitions) and for all groups. However, these differences are more prominent in female than they are in male when considering both residual stress or stretch distributions. When looking at stresses specifically, while differences are all significant for all female groups (i.e., when comparing isolated constituents to one another and when comparing isolated constituents to intact tissue), in male hypertensive animals, differences are mostly not significant when comparing intact tissue to isolated collagen fibers and isolated myocytes, for both CD and HFD. For the male hypertensive animals, however, all the residual stress components calculated for isolated collagen fibers remain significantly higher than that for isolated myocytes. A similar trend can be observed in the residual stretch distributions as well, with two exceptions: (1) in CD female animals we observe no differences between intact tissue and isolated collagen fibers (true for all stretch markers considered) and (2) in HFD male animals, we do observe a significant difference between intact tissue and collagen fibers (true for most stretch markers considered). As a representative subset of stress components, we show the maximum circumferential tensile stress and stretch in Fig. 3.8(a) and 3.8(b), respectively – focusing on highlighting differences between constituents.

When analyzing the effect of high blood pressure on the residual stress and stretch distributions, we observe that, overall, NT animals have higher residual stresses/stretch when compared to hypertensive animals (both CD and HFD) for both male and female. The differences between NT and both cases of hypertensive were consistently significant for all samples collected from the female animals, while it was only significant in the males' isolated collagen fibers and slightly (P = 0.07) for the CD isolated myocytes (insignificant for the HFD isolated myocytes). Moreover, we have found no differences when comparing the stress/stretch levels between CD and HFD animals, in both male and female, the only exception being potentially an increase in collagen residual stresses/stretches when comparing CD to HFD (not significant). Fig. 3.9 shows the maximum

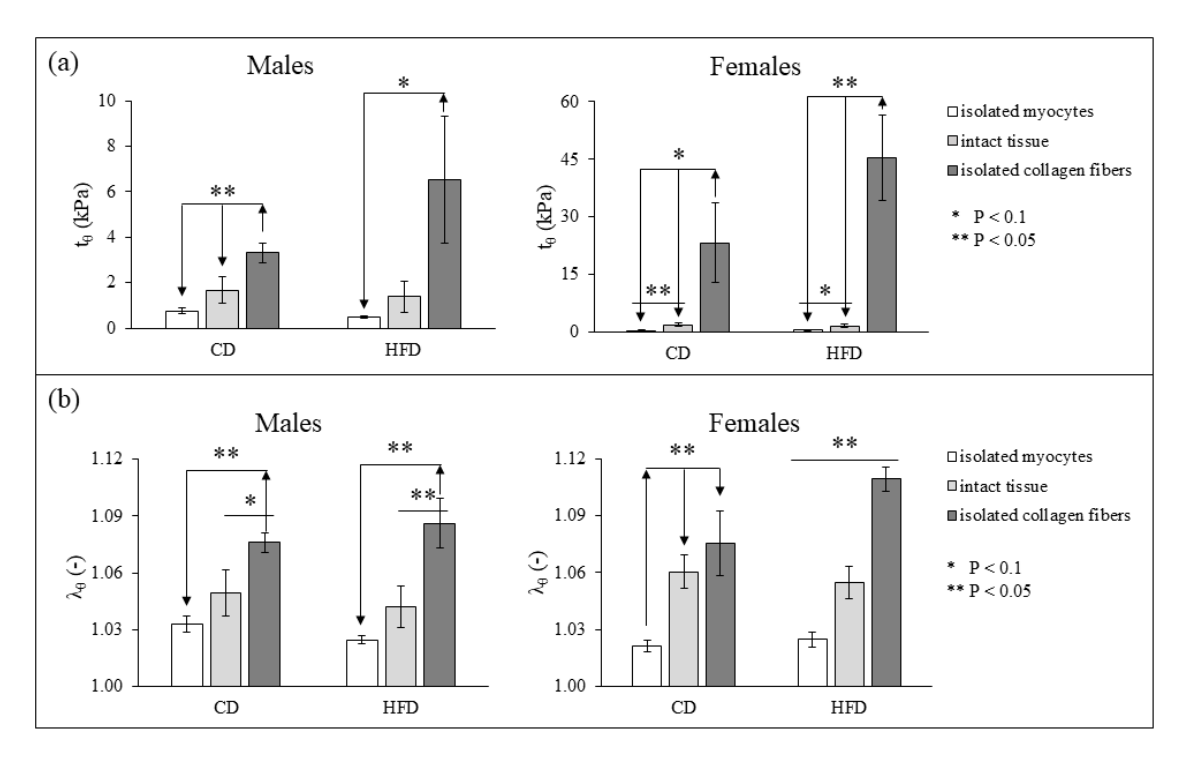


Figure 3.8: Comparison between isolated myocytes, isolated collagen fibers, and intact tissue for both CD and HFD of the maximum value of (a) circumferential residual stress (t_{θ} , as identified in Figure 2) and (b) circumferential stretch (λ_{θ}) for all samples (avg. \pm st. err., note: the graphs have different vertical axes).

value of circumferential stress and stretch, as a representative subset, focusing on highlighting the comparison between NT and hypertensive animals, and between male and female animals, for isolated myocytes (left), intact tissue (center), and isolated collagen fibers (right).

From Fig. 3.9 we can also infer the effect of sex on the stress distribution. In NT animals, females have significantly higher values for all the residual stress/stretch components when compared to males. In hypertensive animals, the stress in the female hearts remains significantly higher than that in the male for the isolated collagen fiber network, results specific to the residual stress distribution (the residual stretches show no sex-difference in the isolated collagen fibers). In addition, the difference in residual stress/stretch characteristics between male and female animals is lost for both intact tissue and isolated myocytes (or the relation is reversed, like in isolated myocytes in CD Dahl-SS rats, where males have a higher stress than females).

Finally, Fig. 3.10 shows the relative location across the left ventricle wall (measured through

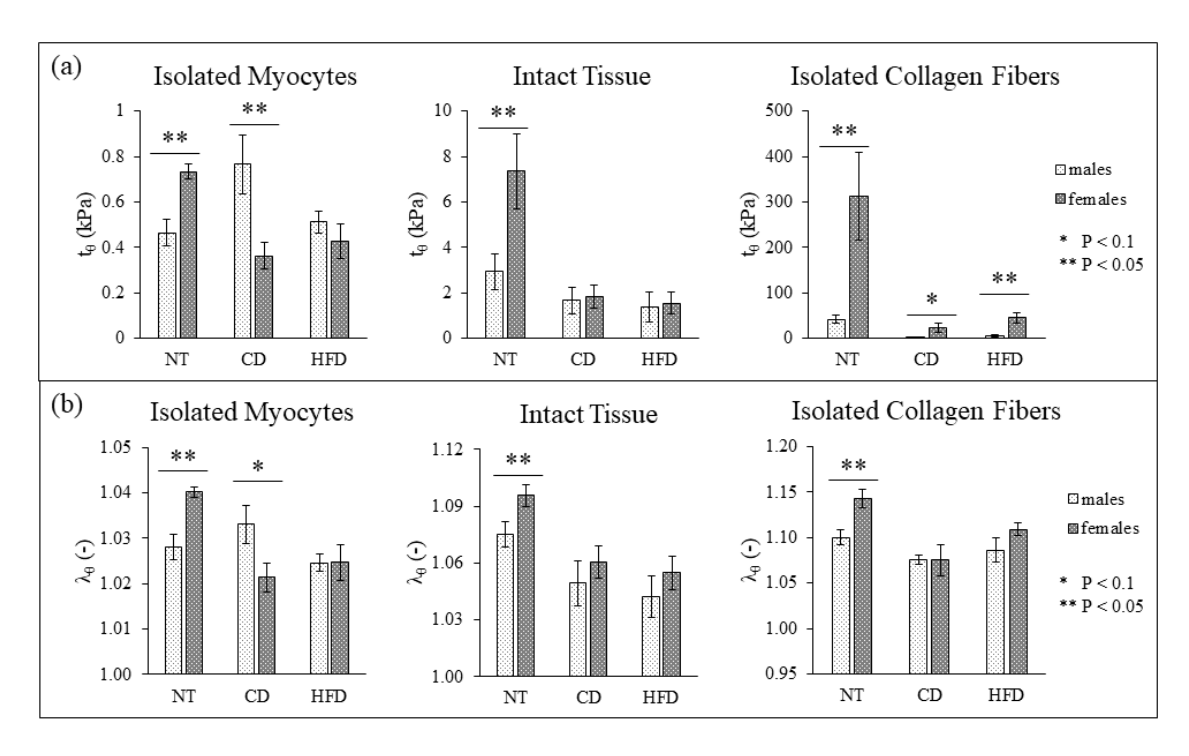


Figure 3.9: Comparison between sex of the animal, including data for NT, of the maximum value of (a) circumferential residual stress (t_{θ} , as identified in Figure 3.3) and (b) circumferential stretch (λ_{θ} , as identified in Figure 3.4) for all samples (avg. \pm st. err., note: the graphs have different vertical axes).

the dimensionless radius) of the circumferential neutral axis (location along the radius where the circumferential stress is null) for intact tissue in both male and female animals. The neutral axis in female left ventricle moves significantly closer to the luminal layer with the increase in blood pressure, while it remains unchanged for male hearts.

3.3 DISCUSSION

We have measured the changes in the OA and residual stresses/stretch, associated with hypertension, of the intact cardiac tissue and tissues with isolated constituents in both male and female rats. The key findings of this study are 1) OA in the intact tissue, isolated collagen fibers, and isolated myocytes are all reduced with hypertension in male and female rats; 2) All residual stress/stretch components are highest in the isolated collagen fibers, followed by the intact tissue and isolated myocytes in both male and female rats; 3) All the residual stress/stretch components are also reduced with hypertension in both male and female rats; and 4) All the residual stress/stretch components

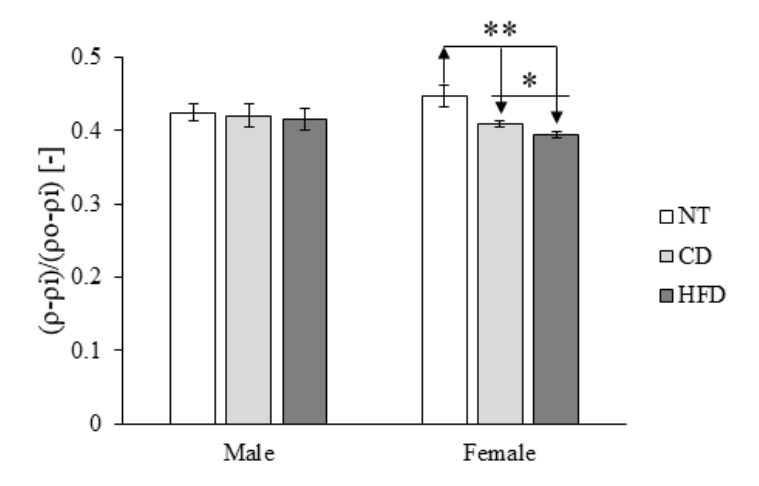


Figure 3.10: Non-dimensional radial location of the circumferential neutral axis in intact tissue for all for all samples (avg. \pm st. err.). Non-dimensional radius of 0 indicates the inner wall, while a value of 1 indicates the outer wall. Comparison between CD and HFD (also included data for NT).

in the female NT rats are significantly higher than those in the male NT rats, but the difference is lost with hypertension in the intact tissue and tissue with isolated myocytes.

Our finding of a reduction in OA with hypertension is consistent with a previous study on the embryonic chick heart [135], where they found the OA was decreased from 31 ± 10 to a minimum of -8 ± 12 degrees 12 hours after induction of pressure overload. This finding is, however, in contrast to a previous study, which reported that the OA of the intact tissue is increased with pressure overload [107]. This discrepancy may be due to 1) the different approach used to generate pressure overload – aortic banding [107] vs. Dahl-SS animals that are genetically predisposed to high blood pressure [45] used here and 2) the different stages of remodeling – 3 weeks after banding [107] vs. 24 weeks of CD or HFD here. Consequently, the tissues studied here may correspond more to the decompensated phase of remodeling vs. compensated in Omens et. al. [107]. Finally, the OA reported in Omens et. al. [107] is higher in hypertensive animals compared to controls one week after banding (i.e., after onset of pressure overload); however, the authors reported no statistically significant difference between the groups 3 weeks after surgery. This could support an inversion between the values of the OA of treated vs. control animals in later time points, leading to a lower value of OA in hypertensive animals long-term.

Our analysis went further to estimate the OA angle (residual strains) of the isolated collagen fibers and myocytes as well as their corresponding residual stresses, which previous studies are lacking [109]. We found that residual stresses associated with the isolated collagen fibers are significantly higher than that of the isolated myocytes and the intact cardiac tissue. This suggests that collagen fibers remain the stronger contributor to the residual stress distribution in remodeled hypertensive left ventricles. The residual stresses of the constituents (especially that of the isolated collagen fibers) as well as the intact tissue are all reduced with hypertension. Based on a previous study [42], a reduction in the residual stress may contribute to the increased left ventricle stiffness that is typically associated with hypertension [137]. Moreover, males fed with HFD have decreased OA and residual stresses/stretches in isolated myocytes when compared to males fed with CD, and females fed with HFD have increased OA and residual stresses/stretches in isolated collagen fibers when compared to females fed CD. These results may suggest a potential increase in the contribution of the collagen fibers and a decrease in the contribution of the myocytes to the residual stress distribution as MAP increases, despite having no changes in the overall CAF between NT and hypertensive animals (Fig. 3.6). We have also observed, only in female animals, that the circumferential neutral axis moves closer to the inner radius with an increase in MAP (Fig. 3.10), suggesting a larger portion of the wall is in tension due to residual stresses. This could be associated with the observed changes in circumferential systolic strain distribution across the myocardial wall in hypertension [111].

We have also investigated sex differences in residual stresses/stretches in this study, and have found that residual stresses/stretches in the female rats are significantly higher than those in the male rats under normotensive condition. This difference, however, is lost or inverted with hypertension in the intact tissue as well as the tissue with isolated myocytes, suggesting that hypertension has a bigger effect on the residual stress field in female rats than male rats. In fact, residual stresses in the female left ventricle decrease with hypertension on average 77% for intact tissue and 46% for isolated myocytes, while in the male left ventricle, on average, residual stresses in intact tissue decrease by 48% and in isolated myocytes increase by 37% (% change evaluated for the maximum

circumferential stress, Fig. 3.8). This suggests that the remodeling process in the left ventricle could have sex-specific traits, a hypothesis supported also by observation in a previous publication. First, gender-differences in heart failure preserved ejection fraction (HF_pEF) , of which hypertension is a major risk factor, have long been observed [28, 3]. Besides affecting more women, it is also found in a study that left ventricle diastolic function is more impaired with a greater diastolic stiffness present in women than men in HF_pEF [47]. Our finding that a larger reduction in residual stresses/stretches associated with hypertension (that in turn may cause an increase in left ventricle stiffness based on a previous study [42]) is consistent with this clinical observation, despite the decrease in CAF in the hypertensive samples compared to NT samples in females. Additionally, while hypertension is more prevalent in men than in women in young age, this gap does close and may even reverse by age 75 [119]. However, to our knowledge, it is unknown if there is a difference in severity of hypertension associated with this difference in prevalence. The current study presented data from rats 24 weeks of age, close to middle age for these animals. At this age, we show that the females are in a more severe state of hypertension than the males, in terms of both a higher MAP as well as higher residual stress. This disparity between males and females could be caused by several factors such as body weight, hormones, or activity levels. In future studies, we can investigate this by adding time points to the animals' ages, as well as measuring body weights and hormone levels, along with the MAP.

Finally, we have also analyzed changes in the overall geometry of the left ventricle, and we observed an increase in the left ventricle cross-sectional area following a pathological increase in MAP, which confirms what was previously reported [107]. These differences seem to be associated with an increase in both left ventricle thickness and diameter. Specifically, both outer diameter and thickness increase with an increase in MAP in female rats. In male rats, both outer diameter and thickness are higher in the hypertensive animals for the isolated constituents, while the thickness increases moderately in the intact tissue.

3.3.1 Limitations

This study has some limitations. First, the duration of the opening angle experiment was longer than what was previously published by other groups [103]. The duration of the overall experiment was determined based on a terminating criterion that the rate of change in angle is equal or less than $\sim 0.2^{\circ}$ /min on average for all the experimental groups. This is because we seek to determine the opening angle at a steady state that corresponds to the true residual stress found in the left ventricle in its passive state. Indeed, the duration is longer than those found in previous studies (e.g., Omens et. al. [103] measured the opening angle within 30 seconds of radial cutting to determine the residual strain without ischemic contracture). While it is possible that the measurement performed on intact tissue and isolated myocytes is affected by muscle contraction, we performed all measurement in a solution containing a myosin inhibitor (BDM) to limit this effect. Furthermore, we collected datapoints throughout the 90 minutes of the experiment, including at the time of the cut (within 30 sec); and the statistical analysis for the measurements collected at the time of the cut seems to confirm the relations established considering the OA measured at 90 min (data not shown). Second, we are using material parameters collected from a uniaxial tensile test and employing an isotropic model to describe the left ventricle constituents in the stress analysis. While we know that the myocardium does not behave as an isotropic material, we were constrained by the experimental capabilities in our facilities. To decrease the effect of this limitation on the analysis, we have decided to, first, include results for both the residual stress and stretch distributions, and second, to focus our analysis on the circumferential distribution of stress, which is the direction better characterized by both the experimental set up and the choice of strain energy function. A more precise characterization of the tissue, which includes biaxial information and more accurate description of the fiber distributions across the wall, will be the focus of future studies.

3.4 CONCLUSION

In this study, we reported the changes in the left ventricle geometry, composition, and residual stress distribution in Dahl-SS rats of both sexes fed with CD or HFD. In summary, we show that

1) animals fed with HFD have a larger left ventricle cross-sectional area compared to CD in both sexes; 2) CAF is not affected by diet; 3) OA and residual stresses/stretches of collagen fibers is largest followed by that of the intact tissue and then isolated myocytes in hypertension; 4) OA of isolated collagen fibers from the left ventricle of male rats fed with HFD is lower than those fed with CD, whereas the OA of isolated myocytes from the left ventricle of female rats fed with HFD is higher those fed with CD; 5) OA and residual stresses/stretches of the left ventricle in the hypertensive animals are lower than that of the NT animals; and 6) the residual stresses/stretches in the female NT rats are higher when compared to the male NT rats, while we observe no difference between female and male hypertensive rats in the intact tissue and tissue with isolated myocytes.

CHAPTER 4

CHANGES IN BLADDER WALL MECHANICAL BEHAVIOR WITH TYPE II DIABETES

As previously mentioned, while several studies have reported changes in mechanical behavior and structure in the urinary bladder due to type I diabetes, this same information has not been reported in regard to type II diabetes. In this study, we aim to characterize the alterations in mechanical behavior and the extracellular matrix of the urinary bladder following neuropathy induced by type II diabetes in rats. Specifically, we will use two type II diabetic rat models: Goto-Kakizaki (a lean model) and Zucker Diabetic Fatty (an obese model). When studying tissue remodeling caused by type II diabetes, it is key to consider obesity as a factor, as the two are highly correlated. Additionally, obesity has been shown to cause systemic inflammation [34], which could exacerbate the remodeling response. To study this, we have taken the bladders from the lean and obese diabetic models, along with their controls, subjected them to stress-stretch testing, measured the relative amounts of constituents, and quantified immune system activation. Finally, we have implemented a constitutive model to quantify differences in mechanical behavior between the groups.

4.1 METHODS

As a lean model of type II diabetes, we used male Goto-Kakizaki (GK-D, Taconic Farm, Germantown, NY, n = 6) and male Wistar rats as their appropriate controls (GK-C, Charles River Labs, Wilmington, MA, n = 6) [48]. As an obese model of type II diabetes, we used male Zucker diabetic fatty rats (ZDF-D, Charles River, n = 4) and their male lean littermate as appropriate controls (ZDF-C, Charles River, n = 4) [112]. The GK groups were fed an NIH-31M diet (23% cal/protein, 18% cal/fat, 59% cal/carbohydrates), while the ZDF groups were fed a Purina 5008 diet (27% cal/protein, 17% cal/fat, and 56% cal/carbohydrates). Animals were weighed, their fasting blood glucose (FBG) measured, and euthanized at age 14-17 weeks [132]. A subset of the GK animals (3 controls, 3 diabetics) were aged 35-43 weeks. Following euthanasia, this subset of

animals was kept frozen (-4°C) for 4-5 months before isolation and testing of the urinary bladder. For this reason, statistical analyses were performed on the mechanics of these bladders compared to their 14-17-week-old, non-frozen counterparts, and no differences were found. All animal protocols used in this study were approved by Michigan State University (MSU) Institutional Animal Care and Use Committee.

4.1.1 Sample preparation

Following euthanasia, whole urinary bladders were extracted from the rats. The bladders were photographed in order to measure their length and width, Fig. 4.1(a); then we isolated two ringshaped samples \sim 3mm in height. One ring was flash frozen in optimal cutting temperature (O.C.T.) compound, and stored at -80°C for 6-8 months. At the time of testing, the samples were removed from the -80°C freezer and allowed to thaw at room temperature for 1 hour. They were then rinsed in calcium-free Krebs-Hensleit buffer containing (in g/L distilled water): 2 C₆H₁₂O₆, 0.141 MgSO₄, 0.16 KH₂PO₄, 0.35 KCl, 6.9 NaCl, 2.1 NaHCO₃. Prior to testing, the rings were decellularized following a modification of a previously published protocol [51] (Chapters 2 and 3), adapted to treat urinary bladder tissue. Briefly, the samples were soaked in the following solutions: heparinized phosphate-buffered saline for 15 minutes, 1% sodium-dodecyl sulfate for 48 hours, distilled water for 15 minutes, and finally, 1% Triton-X100 for 30 minutes. Finally, the samples were rinsed again in the Krebs buffer before mechanical testing. Preliminary results showed no differences (P = 0.632) in the mechanical behavior of fresh and frozen decellularized bladder tissue (data not shown).

4.1.2 Histology and microstructural analysis

The second ring obtained was set for histology; briefly the tissue was submerged in 10% formalin for 4 days, then transported in 30% ethanol to MSU Histopathology lab and embedded in paraffin, sliced at 5µm, and stained with a Verhoeff-Van Gieson (VVG) and toluidine blue (t-blue) stain. An initial image was taken of the stained slides on a desktop to acquire a measurement of the wall

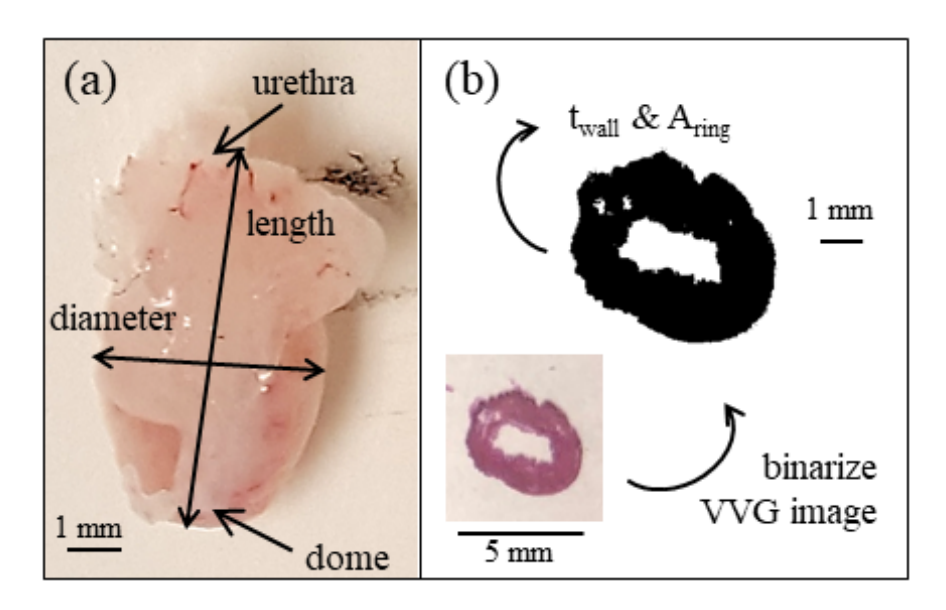


Figure 4.1: (a) Measurement locations for bladder sample geometry (GK-C bladder used for illustration). (b) Image of a stained slide taken on a desktop to measure the wall thickness, t_{wall} , and ring cross-sectional area, A_{ring} .

thickness, t_{wall} , and ring cross-sectional area, A_{ring} , Fig. 4.1(b). The remaining images were taken at 40x magnification on an Olympus BX41 microscope using Nikon DXM1200 software.

For VVG, color and shape analyses were performed using a custom MatLab code. The code identified the following in VVG stain: elastin (purple or black & fiber-shaped), collagen (magenta), and cells (cytosol = mauve & flat, nuclei = purple or black & round). Area fractions of each constituent were calculated in the images as the number of pixels of the constituent divided by the total number of pixels in the image (after removing any background pixels not containing tissue).

The t-blue stain was used to count and rank activation of mast cells. These cells are activated by the immune system and are used for assessing inflammatory response of a tissue [94, 121]. Because mast cells will be present regardless of inflammation level, simply counting the number of mast cells present in the tissue samples would not provide sufficient information. Instead, mast cell activation was estimated through a ranking system [35], Fig. 4.2. Finally, a normalized mast cell activation (NMCA) score was calculated for each sample by

$$NMCA = \frac{1 \times n_1^{mc} + 2 \times n_2^{mc} + 3 \times n_3^{mc}}{A_{ring}}$$
 (4.1)

where n_1^{mc} , n_2^{mc} , and n_3^{mc} , are the number of mast cells that received a score of 1, 2, and 3,

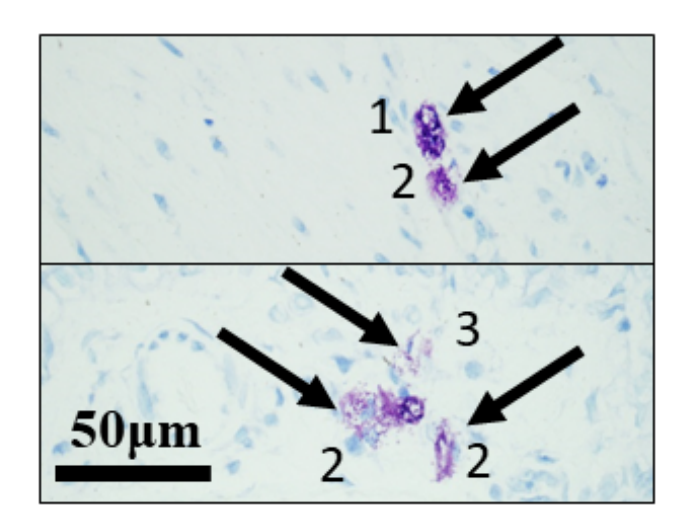


Figure 4.2: Representative mast cells and their scores from a ZDF diabetic bladder in t-blue stain.

respectively and A_{ring} represents the cross-sectional area of the sample. A completely inactive mast cell—one that was completely encapsulated—was given a score of 1. A completely active mast cell—one that had been fully de-granulated—received a score of 3. Any mast cell that appeared to be beginning to de-granulate received a score of 2 [35].

4.1.3 Mechanical testing

Following the experimental protocol for the uniaxial ring test outlined in Chapter 3 (modified for urinary bladder tissue), samples were mounted onto a uniaxial stretching machine, see Fig. 4.3. Samples were mounted onto a uniaxial stretching machine using two loops of black suture—tied at the bottom to a clamp and at the top to a 250g capacity load cell (LSB200, Futek); the bottom clamp was contained within a custom saline bath that was filled with Krebs for the duration of the tests to ensure adequate hydration of the tissue. The uniaxial machine movement as well as measurements from the load cell and a 1.6MP Android camera mounted in front of the sample were all controlled simultaneously through LabView. The load cell measured uniaxial force, while the camera measured sample height. A 10g preload was placed on each sample once before testing. The complete uniaxial test, adapted from a previously published work [52], involved subjecting the samples to the following (all at a speed of 0.15mm/s): 5% stretch for 10 cycles (preconditioning),

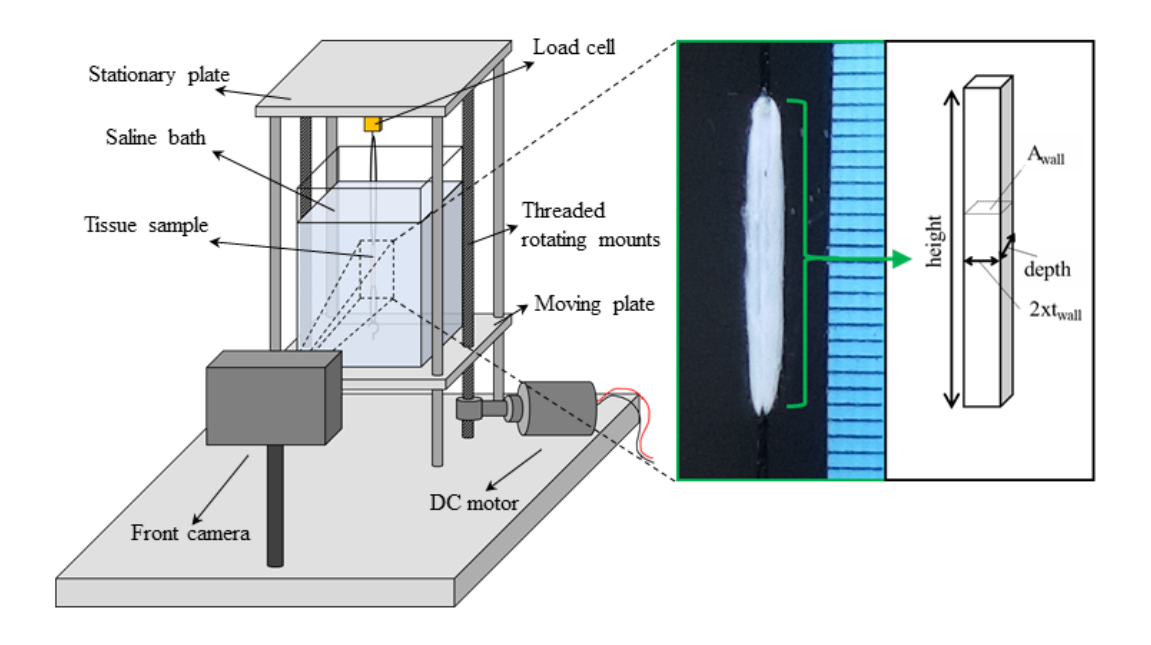


Figure 4.3: Experimental set-up and sample geometry.

10% stretch for 5 cycles, 20% stretch for 5 cycles, and 30% stretch for 5 cycles. A modification was made from the previously described protocol due to the access of only one camera. A single picture of the mounted sample was taken from the front before each set of cyclic loading. This image was used to estimate the wall cross sectional area, A_{wall} of the reference configuration for each test, Fig. 4.3.

Assuming the sample to be incompressible produced the following deformation gradient

$$F = \begin{bmatrix} \lambda & 0 & 0 \\ 0 & \frac{1}{\sqrt{\lambda}} & 0 \\ 0 & 0 & \frac{1}{\sqrt{\lambda}} \end{bmatrix}$$
 (4.2)

where λ is the uniaxial stretch in the loading direction—equal to the ratio of the current height over the reference height, defined as the height at the beginning of each set of cycles. Then, A_{wall} will change with respect to $1/\lambda$ throughout the test. Initial A_{wall} was calculated using t_{wall} and height measured from the front-view pictures and depth using a volume measurement from the unloaded rings along with the assumption of incompressibility, Fig. 4.3. Initial height and A_{wall} for each sample were updated before each set of cycles during the experiments. The Cauchy stress in the

uniaxial direction (t_{exp}) is then the force, as measured by the load cell, over the current A_{wall} value. For comparison across test groups, the last loading curve of the 30% cyclic test was isolated in each sample. Each of these curves started at a stress value of 0kPa with no stretch and, depending on the stiffness of the sample, reached a maximum of ~75-350kPa (~50-125g) at 30% stretch. In order to average within and compare between groups, the stretch of each curve was linearly interpolated to produce ten points between 0 and 75kPa, as this was just below the lowest maximum stress value reached by all samples. Six standard type II t-tests were used to assess differences between groups at each stress-level. Additionally, ANOVA's were run to account for interactions between obesity and diabetes.

4.1.4 Constitutive modeling framework

For this study, we implemented a strain energy function of a Demiray material [26, 24], previously described in Chapters 2 and 3. Briefly, the strain energy function for this type of material is:

$$W(C) = c(e^{k(I_1(C)-3)} - 1)$$
(4.3)

where c and k are material parameters, the first with dimension of stress, and the second dimensionless, and $I_1 = tr(C)$ is the first invariant of the right Cauchy-Green deformation tensor $C = F^T F$. It follows that the Cauchy stress, T, is given by

$$T = -pI + 2F \frac{\partial W(C)}{\partial C} F^{T}$$
(4.4)

where p is the Lagrange multiplier needed to enforce incompressibility. For a uniaxial stretch assuming zero-stress boundary conditions in the transverse plane, the theoretical Cauchy stress in the loading direction, t_{th} , can be written as

$$t_{th} = 2ck\left(\lambda^2 - \frac{1}{\lambda}\right)e^{k\left(\lambda^2 + \frac{2}{\lambda} - 3\right)} \tag{4.5}$$

The material parameters c and k have been optimized to best describe the experimental data (i.e., the last loading of the 30% stretch curves for each sample, in its totality). The parameter

optimization was performed by least squares minimization of error evaluated as the difference between theoretical and experimental stress. Due to the nonlinear behavior of the bladder tissue, the data becomes clustered in the lower stress region of the stress-stretch plots. For this reason, the error was weighted more heavily for lower stresses during the optimization process. Specifically, the error values for the first half of the data set were multiplied by two. Goodness of fit of each curve was evaluated in the form of normalized root mean square deviation (NRMSD)[12]

$$NRMSD = \frac{1}{t_{exp}^{max}} \sqrt{\frac{\sum (t_{th} - t_{exp})^2}{n}}$$
 (4.6)

where t_{th} and t_{exp} are the theoretical (Eq. 4.5) and experimental Cauchy stress, n is the number of data points, and t_{exp}^{max} is equal to the maximum experimental value of stress during the 30% loading.

4.2 RESULTS

Both the GK and ZDF diabetic groups showed a significant increase in FBG (P < 0.1 for GK, P < 0.01 for ZDF) compared to their respective controls, see Table 4.1 [81, 82]. It should be noted that one GK-C animal's FBG level could be considered an outlier and, if removed, the value of the FBG for this group drops from 125+/-83 mg/dL to 86+/-9 mg/dL, which is strongly different from its diabetic counterparts (P < 0.01). A reason for this high reading in one animal could be that it was subjected to isoflurane anesthetic—which has been shown to increase blood glucose levels [129]—shortly before the measurement was taken. Moreover, this animal's physiological parameters (mitochondria, cardiovascular, and muscle performances) were similar to those of the rest of the GK-C group (data not shown). For this reason, we included the mechanical and histological data from this animal. A proposed cut-off of FBG to diagnose diabetic onset in rats is 135 mg/dL [146]. While the GK-C are below this cut-off, the ZDF-C are above it, yet still significantly below the ZDF-D. Additionally, the GK-C had a body weight significantly higher than the GK-D, while the ZDF-C group body weight was significantly lower than their diabetic counterparts (P < 0.01 for both groups).

The bladders of the diabetic rats in both groups were longer on average than the controls, Table 4.2. The ZDF diabetics showed slightly increased outer diameters compared to their controls while

Measurement:	GK-C	GK-D	ZDF-C	ZDF-D
FBG (mg/dL) Body Weight (g)	125 ± 83	208 ± 49	149 ± 14	495 ± 84
	685 ± 171	395 ± 75	317 ± 6	377 ± 13

Table 4.1: FBG levels and body weights of each group at time of euthanasia (avg. \pm st.dev.).

Group:	length	diameter	volume	t _{wall}	A _{ring}
GK-C	12.10 ± 1.78	6.30 ± 0.26	118.41 ± 12.70	1.32 ± 0.06	13.92 ± 0.93
GK-D	13.94 ± 2.43	5.63 ± 0.69	146.90 ± 25.08	1.15 ± 0.48	13.08 ± 2.78
ZDF-C	11.50 ± 0.87	5.83 ± 1.04	122.78 ± 61.52	0.81 ± 0.20	11.78 ± 5.59
ZDF-D	14.00 ± 2.16	7.25 ± 1.19	157.98 ± 19.68	1.08 ± 0.27	15.78 ± 4.79

Table 4.2: Geometry measurements taken for each group (avg. \pm st.dev.).

Group:	cells	collagen fibers	elastin fibers
GK-C	0.803 ± 0.029	0.195 ± 0.030	0.002 ± 0.001
GK-D	0.799 ± 0.008	0.199 ± 0.007	0.002 ± 0.001
ZDF-C	0.787 ± 0.073	0.195 ± 0.084	0.018 ± 0.019
ZDF-D	0.836 ± 0.061	0.145 ± 0.071	0.019 ± 0.021

Table 4.3: Area fractions of tissue constituents for each group (avg. \pm st.dev.)

the GKs were slightly smaller in diameter than controls. On average, the diabetic bladders had a larger volume than their respective controls. The GK bladders displayed thinned walls with diabetes, while the diabetic ZDF bladders had slightly thicker walls than the control ZDFs. There were no significant differences in these measurements between the diabetics and their respective controls. However, the diabetic ZDF bladders had significantly larger outer diameters than the diabetic GKs and the controls ZDF bladders were significantly thinner than the GK controls.

4.2.1 Histology and microstructural analysis

VVG – Analysis of the VVG slides found no significant differences area fractions of cells, collagen fibers, or elastin fibers in the tissue samples, Table 4.3.

T-blue – We hypothesized that the NMCA (Eq. 4.1) would be increased in the diabetic animals compared to their controls, as type II diabetes has been associated with inflammation [114], and

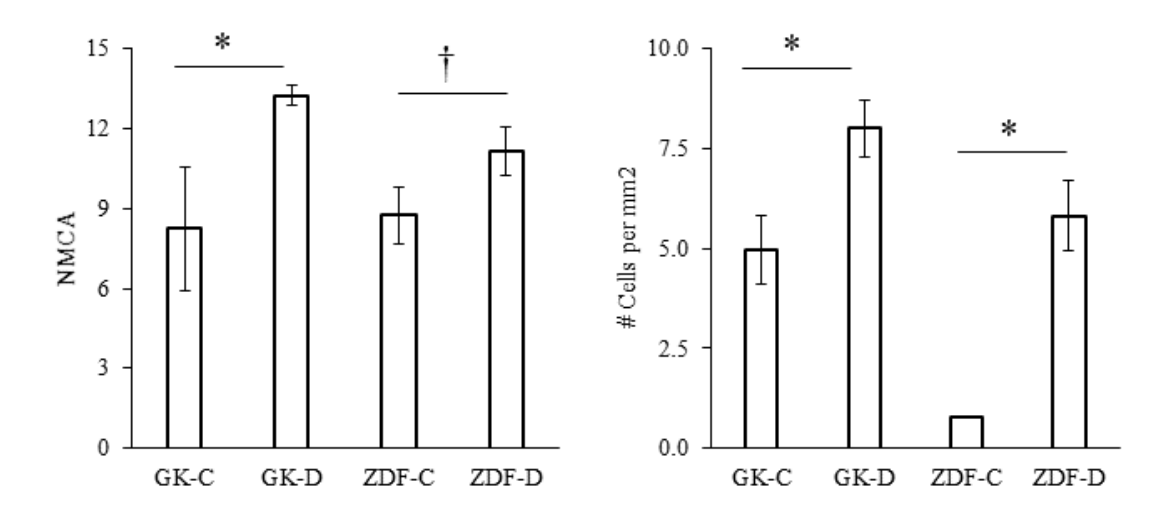


Figure 4.4: Left: NMCA score for each group, Right: mast cell density for each group. Error bars show standard error, \dagger - P < 0.1, * - P < 0.05

so this would likely lead to immune system—and mast cell—activation. This increase in NMCA was significant (P < 0.05) in the GK animal model, and nearly significant in the ZDF model (P = 0.07), Fig. 4.4. It was also noted that there was an overall higher amount of mast cells in the GK bladders than in the ZDF bladders, though this may not be indicative of higher inflammation, as these are two different breeds of rat. Additionally, we report a normalized total count of the mast cells in each group. In both groups, the number of mast cells per mm² was significantly higher in the diabetics than in the controls, Fig. 4.4.

4.2.2 Mechanical testing

In both the ZDF and the GK models, the diabetic bladders were significantly more compliant than the control bladders. This increase in compliance can be seen in Fig. 4.5 as a right-ward shift of the curve. Additionally, the ZDF-C showed significantly increased compliance compared to the GK-C group, though this difference was not present in the diabetics.

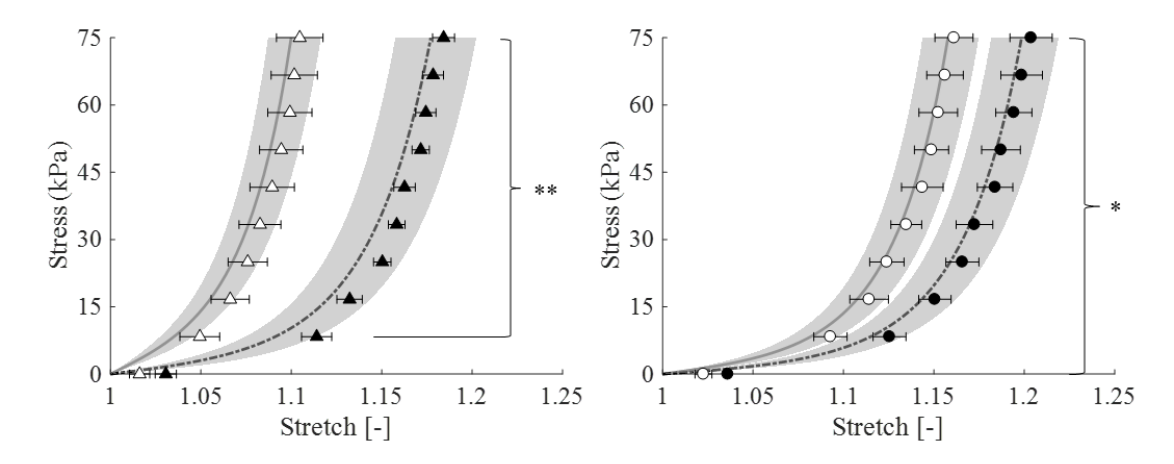


Figure 4.5: Average stress-stretch curves for each test group (markers) and simulated stress-stretch curves from model (lines), for GK (left) and ZDF (right). White markers represent controls, and black markers represent diabetics. Error bars and shaded regions represent standard error of experimental stretch and standard error of model-predicted stretch, respectively. Significance values refer to mechanical data, * - P < 0.1, ** - P < 0.05.

Group:	c (kPa)	k (-)
GK-C	0.715 ± 0.268	46.76 ± 15.50
GK-D	$0.339 \pm 0.222*$	$24.94 \pm 7.01*$
ZDF-C	$0.295 \pm 0.109*$	31.46 ± 6.28
ZDF-D	$0.205 \pm 0.081*$	$24.09 \pm 4.68*$

Table 4.4: Estimated material parameter values for the model fit of each group (avg. \pm st.dev.). * - P < 0.05 compared to GK-C; no other comparisons were significant.

4.2.3 Constitutive model parameters

In order to assist with the understanding of where in the stress-stretch curves the differences between the groups lie, we analyze the material parameters c and k, as introduced in Equations 4.3 and 4.5. Fig. 4.5 shows theoretical stress-strain curves using average +/- standard error of parameters c and k. The range of NRMSD for all groups was 1.5-6.5%.

In order to determine where each parameter had a significant influence over the mechanical model, we performed a sensitivity analysis using the one factor at a time method [55]. Each parameter was given three values (i.e., small, medium, and large) based on the values obtained in the fitting of this study, Table 4.4. Specifically, the small, medium, and large values were

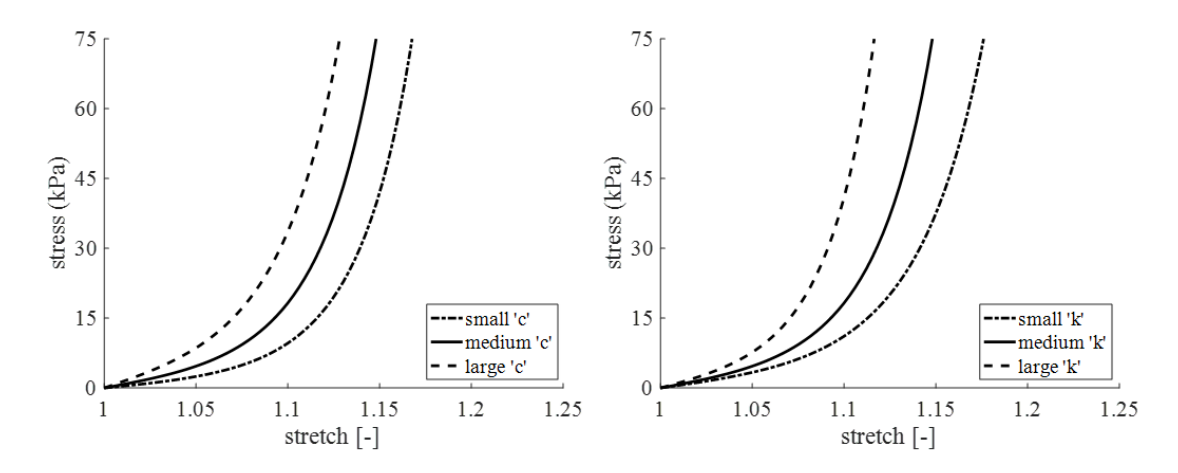


Figure 4.6: Perturbations of a simulated stress-stretch curve through manipulation of c and k.

the minimum, average, and maximum values of the full set of parameters obtained in this study, respectively. While adjusting one parameter, the other was kept at its 'medium' value. The theoretical stress was calculated for each of these parameters and plotted in Fig. 4.6.

It can be seen that the perturbations of both parameters cause marked changes in the stress-stretch response—namely the larger values cause a leftward shift of the curve. However, looking closely, one can see that the changes in stiffness due to c are evident at low-stresses, whereas the changes in stiffness due to k are evident at high-stresses. To understand exactly how these parameters, affect the overall material behavior, we calculated and plotted the %-change in theoretical stress given by the endpoints of the range of these parameters in our fitted experimental data. Using Eq. 4.5 for theoretical stress, minimum and maximum values of % – change were calculated for each parameter using

% - change_c^{min} =
$$100 \times \left[\frac{t_{th}(c_{min}, \bar{k}) - t_{th}(\bar{c}, \bar{k})}{t_{th}(\bar{c}, \bar{k})} \right]$$
 (4.7)

$$\% - \text{change}_c^{max} = 100 \times \left| \frac{t_{th}(c_{max}, \bar{k}) - t_{th}(\bar{c}, \bar{k})}{t_{th}(\bar{c}, \bar{k})} \right|$$
(4.8)

% - change_k^{min} =
$$100 \times \left[\frac{t_{th}(\bar{c}, k_{min}) - t_{th}(\bar{c}, \bar{k})}{t_{th}(\bar{c}, \bar{k})} \right]$$
 (4.9)

% - change_k^{max} = 100 ×
$$\left[\frac{t_{th}(\bar{c}, k_{max}) - t_{th}(\bar{c}, \bar{k})}{t_{th}(\bar{c}, \bar{k})} \right]$$
 (4.10)

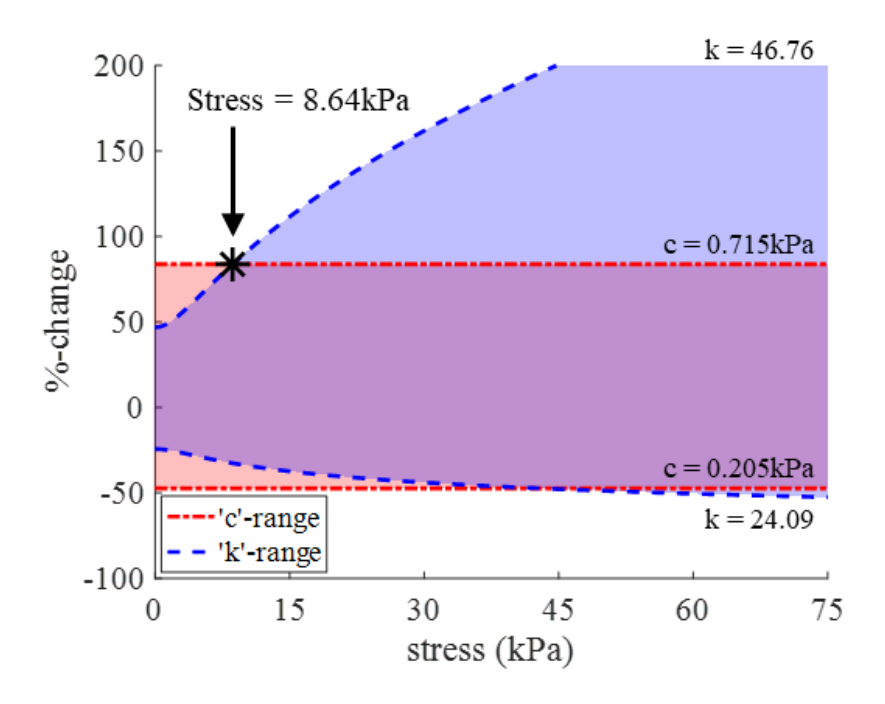


Figure 4.7: Percentage changes from mean parameter stress through perturbation of material parameters. Shaded regions represent possible values in the range of parameters optimized in this study. Black star indicates the earliest value of stress where k sensitivity could overtake c sensitivity.

where \bar{c} and \bar{k} are the average values for c and k from the experimental groups.

As expected with an exponential model, perturbation of the linear parameter c causes a constant change in the stress values, while the exponential parameter k causes a non-linear deviation. At the highest value of k, the %-change caused by k overtakes the %-change caused by the highest value of c at a stress value of 8.64kPa, Fig. 4.7. For any values of these parameters lower than the maximum, this switch in parameter sensitivity will occur for a higher value of stress. We conclude that, for the range of parameters considered here, c dominates the mechanical behavior for stress values below 8.64kPa; above this value the behavior is dominated by the parameter k.

To compare the parameters across each of the groups, t-tests were performed to detect significant differences. Each of the parameters and their statistical significance are summarized in the Table 4.4. The GK-C had significantly higher values of c and k than the GK-D and ZDF-D groups, and a higher value only of c than the ZDF-C group.

Additionally, a 2-way ANOVA was performed to detect differences between c and k from this

model. According to our ANOVA test, c was significantly affected (P < 0.05) by both the presence of diabetes as well as the animal model—i.e. either GK or ZDF. Parameter k was also significantly affected by the animal model, but only mildly by the presence of diabetes (P = 0.0916). Moreover, neither parameter had a significant interaction term, meaning that, in our experiments, there was no correlation between the model and the presence of diabetes.

4.3 DISCUSSION

Diabetes onset was confirmed in both the GK and the ZDF groups of animals through elevated FBG (FBG > 135mg/dL [146]). It should be noted that, while the GK-C had FBG below this threshold, the ZDF-C were above it, with an FBG of 149+/-14mg/dL [81]. While this is still significantly lower than the ZDF-D level of 495+/-84mg/dL, it is worth noting that some of these animals may have been close to becoming diabetic, or pre-diabetic. Additionally, the ZDF-D rats had a significantly higher body weight compared to their controls, confirming the expected obesity of the model of rat. On the other hand, the GK-D rats were significantly smaller in bodyweight than their control counterparts, confirming the lean model.

In both animal models, the average dome to urethra bladder length was higher in the diabetic bladder than in the control. However, the GK-D bladders were slightly smaller in terms of outer diameter, wall thickness, and cross-sectional area than their controls. Conversely, the ZDF-D bladders were slightly larger in these measurements than their controls. Though these differences in overall geometry of the organ were not significant, it is a trend indicative of bladder remodeling that may have been affected by the presence of obesity. Moreover, these trends are consistent with studies that have examined the changes in bladder geometry with type I and II diabetes [83, 116, 101, 114, 73, 39].

Stress-stretch curves of the bladder rings showed increased compliance in both diabetic groups when compared to their controls. This has been shown in previous studies in terms of type I diabetes [144, 84], but this is the first time this has been reported in type II diabetic models. Additionally, we observed an increase in tissue compliance of the ZDF-C bladders compared to the GK-C, while the

GK-D and ZDF-D were statistically similar. The cause of the increase in compliance of the ZDF-C bladders compared to the GK-C was not apparent, as these two groups of bladders both came from animals that were non-diabetic and non-obese. Here, considering the average FBG of these groups can provide some insight. As stated previously, the FBG of some of the ZDF-C animals could be considered pre-diabetic. It is possible that these animals had already begun to experience some bladder dysfunction, which has been shown previously in the ZDF model females [39], resulting in remodeling of the tissue and increased tissue compliance. This bladder dysfunction may not be due to peripheral neuropathy as it is in the diabetic model [9], but potentially as a result of the polyuria, an earlier symptom of diabetes. Furthermore, the obese model of diabetes showed a higher compliance when compared to the lean model.

The constitutive model proved useful in identifying where the differences in the mechanical behavior are most prevalent. Specifically, the model is most sensitive to c for low stress and most sensitive to k for high stress. Here, the c-dominated region and the k-dominated region are separated at a value of stress of ~ 8 kPa (with c being at the lower end and k being at the higher end). While GK-C had a significantly higher value of both c and k when compared to their diabetic counterparts, it only had a larger c parameter when compared to the ZDF-C. This seems to suggest that the ZDF model control bladder was significantly more compliant than the GK at low stress. Moreover, c, when normalized by FBG, has an exponentially decaying correlation ($R^2 = 0.64$) with FBG. That is to say, with increasing FBG, there is evidence of a decrease in c. In the urinary bladder, this may be due to an increase in elastin content, which has been reported previously in type I diabetes [49]. The reason for this hypothesis is the structure and purpose of elastin fibers in the urinary bladder wall. While in other tissues, such as arteries, elastin provides strength to the wall, and an elastin increase would be expected to cause a subsequent increase in wall stiffness (and so, c). However, in the urinary bladder, elastin fibers may be responsible for maintaining collagen fiber waviness. In this case, an increase in elastin content may increase the waviness of the collagen fiber matrix, causing delayed collagen fiber recruitment, and increased tissue compliance at low stresses—i.e. decreased value of c—which has been shown in the present study. It is possible that increased FBG results in increased elastin content, which is responsible for the correlation between FBG and the parameter c. For the bladder function, this low-stress region is especially important, as this organ operates at low pressures, again, suggesting that the ZDF control animals might have experienced bladder dysfunction. This change could be due to chronic overstretching of the bladder caused by polyuria leading to remodeling of extracellular matrix proteins to compensate, causing the tissue to become more compliant at low stress.

Results from the VVG histological analysis showed, however, no differences between any of the groups with respect to constituent area fractions. Collagen was slightly decreased on average in the ZDF diabetics compared to their controls, though this difference was not statistically significant. Due to limitations in our elastin measurement techniques, though, we were unable to measure a precise elastin area fraction at this time. Specifically, in the ZDF tissue samples, the standard deviations were larger than the average area fractions, showing large uncertainty in the measurement. However, changes in mechanical behavior of the tissue lead us to believe that there could be some underlying remodeling of the extracellular matrix that is currently being undetected—i.e. changes in the type of collagen or in elastin content. An increase in elastin has been reported in type I diabetic rat bladders [49]. With respect to type II diabetes, some studies have also found no difference in rat bladder constituent area fractions [73, 39], though noting subjectively that there were some overall changes to the tissue contents, specifically fibrosis. Additionally, Gasbarro et. al. [39] performed their study on female rats, while the current study has been conducted only on males. There has also been reported connections between chronic overstretching of the healthy urinary bladder and production of new elastin, resulting in increased compliance [149].

Mast cell activation was slightly increased in the GK diabetics compared to their controls. This increase was not present in the ZDF bladders, though in both models, there was an observed increase in the density of mast cells in the tissue with diabetes. This could be evidence of inflammation in the tissue, as these cells are recruited as immune system response. Previous studies have also shown inflammation in the urinary bladder in rat models of type I diabetes [114]. Additionally, bladder inflammation has been linked to extracellular matrix remodeling in the neurogenic bladder

(specifically for spinal cord injured rats) [148]. Both the normalized mast cell activation score and the mast cell density were higher in the GK tissue samples compared to the ZDF. However, these are two different breeds of rat and this specific result may not be related to higher inflammatory response, but simply to a difference between the breeds. Furthermore, while the overall cell density in the GK bladders was higher than in the ZDF, when comparing controls to diabetic samples within each model, we see a $\sim 60\%$ increase for GK and a $\sim 600\%$ increase for ZDF. This could be related to ZDF animals being an obese model of type 2 diabetes, and obesity has been correlated with systemic inflammation in humans [34]. The evidence for increased inflammation, supports the possibility of remodeling of the extracellular matrix with diabetes.

4.3.1 Limitations

Limitations of this study include the comparison between different breeds of rat. Though the mechanical behavior of the bladder's extracellular matrix is comparable, their tissue constituents would not be expected to have equivalent area fractions, even in healthy conditions. Therefore, we cannot perform a statistical analysis on the constituents' area factions directly; we can only note the differences between the diabetics and their respective controls. Confirmation of diabetic onset was given through measurement of fasting blood glucose. A more common measurement, clinically, is A1C in blood. A combination of these two measurements in future animal studies of this kind may provide a clearer picture of the connection between the animal models and clinical (human) diabetes. Further, this study only considered male rats, because only the male ZDF rats develop diabetes. Previous studies, however, have shown differences in urinary bladder function in type II diabetic female rats [39, 152]. Additionally, the GK group included two different age ranges, though the mechanical data showed no differences between these ages. Moreover, the present study is focused only on circumferential mechanical properties, while previous studies have shown that changes in urinary bladder mechanical behavior due to type I diabetes are present in both the circumferential and longitudinal directions [144]. Finally, while we suspect a potential increase in elastin content and a switch in the primary type of collagen with diabetes, the quantification technique employed here is unable to detect that. While our mechanical data suggest extracellular matrix protein remodeling, the histological analysis presented here is unable to support this.

4.4 CONCLUSION

To our knowledge, this is the first study of its kind to compare the mechanical behavior of urinary bladder tissue from obese and non-obese type II diabetic rat models. Experimental evidence has shown an increase in tissue compliance due to diabetes that is present both with and without obesity. The constitutive model assisted in showing that the changes in tissue compliance begin at very low stress-stretch values. Moreover, the ZDF lean littermate also displays an increase in bladder compliance when compared to the GK control. This could be due to the elevated—though not technically diabetes-qualifying—FBG level of this group. The ZDF lean littermate control, then, may be exhibiting signs of early diabetes, or pre-diabetes, which could be causing pre-diabetic bladder dysfunction. This concept sheds light on the idea that the bladder may be experiencing dysfunction and even remodeling before this animal model is even considered to be diabetic. Though the histological analysis showed no changes to cell and collagen content, we are continuing to work on obtaining a precise measurement of elastin area fraction and collagen type analysis to pinpoint a specific cause to the changes in tissue mechanical behavior. From this study, we can conclude that there is evidence of tissue inflammation in the bladder associated with both obese and non-obese type II diabetes in rats, which could potentially be triggering extracellular matrix remodeling, resulting in increased bladder tissue compliance. Given these results, future studies may be able to assess the ability of treatments used for type II diabetes in recovering baseline urinary bladder function and mechanical behavior.

CHAPTER 5

RADIATION CYSTITIS-INDUCED STIFFENING OF THE URINARY BLADDER

In the Literature review of this thesis, we discuss effect of radiation cysitis (RC) on bladder composition and function. Currently, however, it is unknown how this may affect overall bladder tissue mechanical behavior. This topic will be addressed in the following chapter. Previously, a preclinical RC model was developed that closely mimics the human condition [157]. This model has been shown to increase deposition of collagen fibers in the detrusor, leading to an overall increase in the concentration of collagen I and III fibers. This study aims to identify alterations to the mechanical behavior of urinary bladder tissue following radiation exposure. Specifically, we aim to characterize these changes through a stress-stretch analysis and calculation of tissue stiffness at several points of interest. To our knowledge, this study is the first-of-its-kind to present mechanical data on radiation cystitis-affected bladder tissue.

5.1 METHODS

This study was performed with full approval from the Beaumont Institutional Animal Care and Use Committee (AL-20-04). Radiation cystitis was induced in the mouse bladder as previously described [157]. Forty 8-week old female C57Bl/6 mice were purchased from Charles River (Wilmington, MA).

5.1.1 Bladder radiation treatment

Mice were randomly assigned to an irradiated or control treatment group (n = 20/group). Radiation was delivered to the mouse bladder using the Small Animal Radiation Research Platform (SARRP) using a two-beam approach. For radiation treatment, anesthesia was induced using 2.5-3% isoflurane through inhalation and maintained at 1.5-2% throughout the procedure (30-45 minutes). Mice were placed on the SARRP platform and a CT image was taken to localize the bladder. The CT image was used to determine the placement of the two beams and assure the whole bladder was

irradiated. All care was taken to avoid the spinal cord, the long bones, colon and overlap of entrance and exit beams to help minimize damage to other organs. Mice received a single dose of 40 Gy, evenly divided over the two beams, using a 5 x 5 collimeter. Mouse breathing and heart rate was continuously monitored during the procedure. After radiation treatment, mice were placed in a heated recovery cage and returned to regular housing when fully recovered. Untreated mice were anesthetized for the same duration of time as their irradiated littermate controls.

5.1.2 Void Spot Assay

Bladder function was assessed using the Void Spot Assay as previously described [157]. In short, mice were singly housed for 4 hours in a cage lined with thick filter paper. During the assay, mice had access to food, but water was withheld. To minimize destruction of the filter paper, mice were given a small rounded and open bottom house, as well as a short piece of string paper. After 4 hours, mice were returned to regular housing, filter paper was placed on an XcitaBlue Conversion Screen (BioRad Cat# 1708182), and urine spots were visualized under TransUV light. Using Fuji Software, urine spots were counted, and total and average void volumes were calculated. Statistical significance was determined through student's t-tests.

5.1.3 Tissue preparation

Three- and six-months post-irradiation, animals were euthanized and bladders collected. Ten irradiated and 10 untreated animals were sacrificed at each time point. Bladders were placed in transportation media (Krebs-Hensleit buffer with 2.1g/L sodium bicarbonate) and shipped on ice overnight to Michigan State University. Upon arrival, each bladder was cut into ring-shaped samples by removing the dome and trigone, leaving behind a lateral ring. The rings were decellularized via a previously published protocol [51], described in each of the previous chapters. Briefly, the rings were soaked in the following solutions: phosphate-buffered saline containing heparin sodium salt for 15 minutes, 1% sodium dodecyl sulfate for 48 hours, deionized water for 15 minutes, and 1% Triton X-100 for 30 minutes. These samples were decellularized for two main reasons: (1)

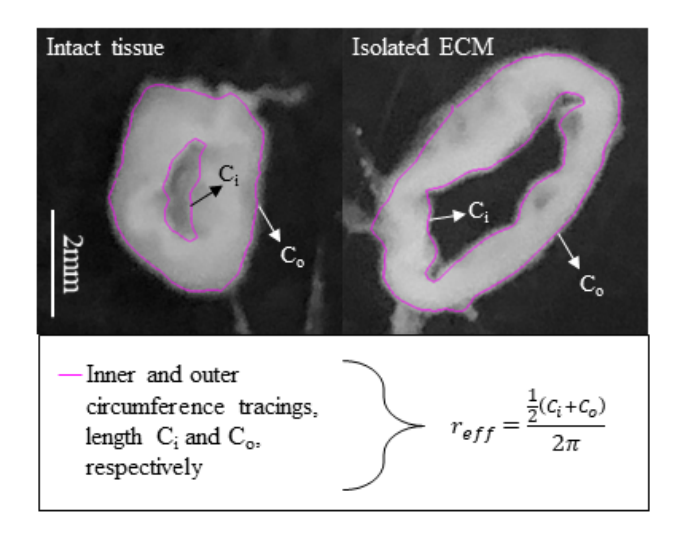


Figure 5.1: Protocol for estimating effective bladder radius.

we aim to focus on the altered mechanical behavior of the remodeled extracellular matrix, and (2) removing the cells removes the possibility of smooth muscle cells contracting during mechanical testing. Ring samples were photographed both before and after decellularization in order to capture any changes to the radius or wall thickness.

5.1.4 Bladder ring radius measurement

An effective radius was measured for each tissue ring, before and after decellularization, using the following method: (1) a photograph of the tissue, taken from above was converted to greyscale, (2) using the NeuronJ plugin for ImageJ [130], the inner and outer circumference of each sample was traced, (3) the length of each tracing was measured in pixels and converted to millimeters using a scale from the original photo, (4) the inner and outer radius of the rings were calculated from their respective circumferences, and finally (5) the effective radius was determined to be the average of these two radii. An effective radius is used rather than the inner and outer radii to negate the effect of the bladder wall folding into itself in photographs. A representation of this measurement can be found in Fig. 5.1.

5.1.5 Mechanical testing and stress-stretch analysis

All mechanical testing was performed in a custom-built saline bath containing calcium-free 300mOsm (isosmotic) Krebs-Hensleit buffer to ensure proper hydration of the tissue. The samples were mounted onto a uniaxial machine using black cotton thread to secure the sample to the saline bath/uniaxial machine on the bottom and to a load cell (FUTEK, LSB200, 250g capacity) at the top. Cameras were mounted facing the front (Hitachi KP-M2A) and side (iPhone, 12MP) of the sample to take pictures that were used to estimate the initial cross-sectional area of the sample. The uniaxial machine's DC motor, along with the cameras and load cell were controlled through Lab-View. Cyclic loading, adapted from a previously published protocol [52] (Chapter 3), was applied to the samples as follows (all at a strain rate of 0.01s-1): 5% stretch for 10 cycles (preconditioning), 10% stretch for 5 cycles, 15% stretch for 5 cycles, and 20% stretch for 5 cycles. Before each set of cycles, a pre-load of 2-2.25g was placed onto the sample. During the loading cycles, the height and axial force were continuously measured via the front-facing camera and the load cell, respectively. Pictures were taken of the sample from the front and side before each set of cycles (after application of the pre-load) to measure the initial width and depth of the samples for an estimation of initial cross-sectional area. For a schematic of the experimental set-up, see Fig. 5.2.

The samples were assumed to be incompressible and isotropic, resulting in a deformation gradient of $F = diag[\lambda; 1/\sqrt{\lambda}; 1/\sqrt{\lambda}]$ where λ is the stretch in the uniaxial (circumferential) direction. The width and depth of the sample, then, change throughout the test with respect to the term $1/\sqrt{\lambda}$. The designated reference configuration was based on the geometry (initial cross-sectional area and initial height) measured before each set of cycles (with the pre-load applied). Then, the stress in the uniaxial direction is simply the ratio between the force read by the load cell and the current cross-sectional area.

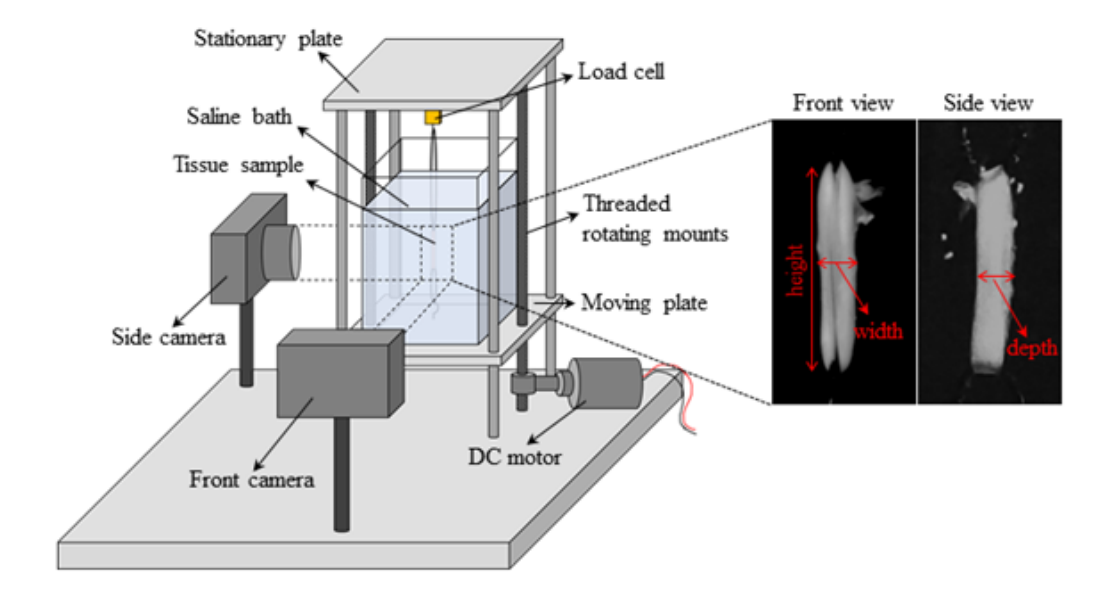


Figure 5.2: Experimental set-up for uniaxial testing.

5.1.6 Constitutive modeling framework

The final 20% loading curves were fitted to a two-parameter, Demiray constitutive model [26, 24]

$$W(C) = c(e^{k(I_1(C)-3)} - 1), (5.1)$$

where c and k are material parameters, C is the right Cauchy-Green deformation tensor $C = F^T F$, and $I_1(C) = tr(C)$ is its first invariant. Following, the definition of Cauchy stress for an incompressible material is

$$t = -p\mathbf{I} + 2\mathbf{F} \frac{\partial W(\mathbf{C})}{\partial \mathbf{C}} \mathbf{F}^{\mathbf{T}}, \tag{5.2}$$

where p is a Lagrange multiplier and I is the identity matrix. For a uniaxial ring test, with noload boundary conditions in the transverse directions, the theoretical stress in the circumferential direction is then

$$t = 2ck\left(\lambda^2 - \frac{1}{\lambda}\right)e^{k\left(\lambda^2 + \frac{2}{\lambda} - 3\right)}.$$
 (5.3)

Parameters, c and k were optimized to fit the full final 20% loading curve for each sample, by minimizing the normalized root mean square deviation through the Matlab function lsqnonlin, as previously described by Chen et. al. [12].

5.1.7 Mechanical parameters and stiffness calculations

To characterize how the mechanical behavior of the extracellular matrix may be changing with respect to radiation cystitis, we have also measured several characteristics of the stress-stretch curves. These characteristics have been measured using a method adapted from a previously published work [14], wherein the model curves for all (produced by Eq. 5.3) are simulated from zero stress to 100kPa, as this is the physiological maximum the bladder may experience [128]. These curves were then separated into three regions: (1) low-stiffness linear region, (2) transition region, and (3) high-stiffness linear region. The low-stiffness linear region was defined as the region between the points $\lambda = 1$ and $\lambda = \lambda_1$ where λ_1 is estimated through the following process. First, a straight line is fitted from the first point on the curve through each of the remaining points on the curve (through λ_{max} , defined by $t(\lambda_{max}) = 100$ kPa). Then, λ_1 is the first point at which the linear fit produces an R² value of less than 0.999. The high stiffness linear region is defined through a similar process to estimate its left bound, λ_2 , by fitting the straight lines backward starting from λ_{max} . Upper and lower stiffnesses of the tissue were estimated as the slopes of these two semi-linear regions. Additionally, to characterize the non-linearity of the stress-stretch curve, we also located the point at which the two linear portions of the curves would intersect. Once these regions were separated, the following parameters were defined:

- 1. λ_1 and λ_2 boundary points between the regions
- 2. t_1 and t_2 the stresses at which λ_1 and λ_2 occur
- 3. λ_{max} the maximum stretch (i.e. the stretch at t = 100kPa)
- 4. k_{low} and k_{high} the stiffnesses (slopes) of the low-stiffness and high-stiffness linear regions, respectively
- 5. (λ_{int}, t_{int}) the point at which the two linear regions would intersect

For a visual definition of these parameters, see Fig. 5.3.

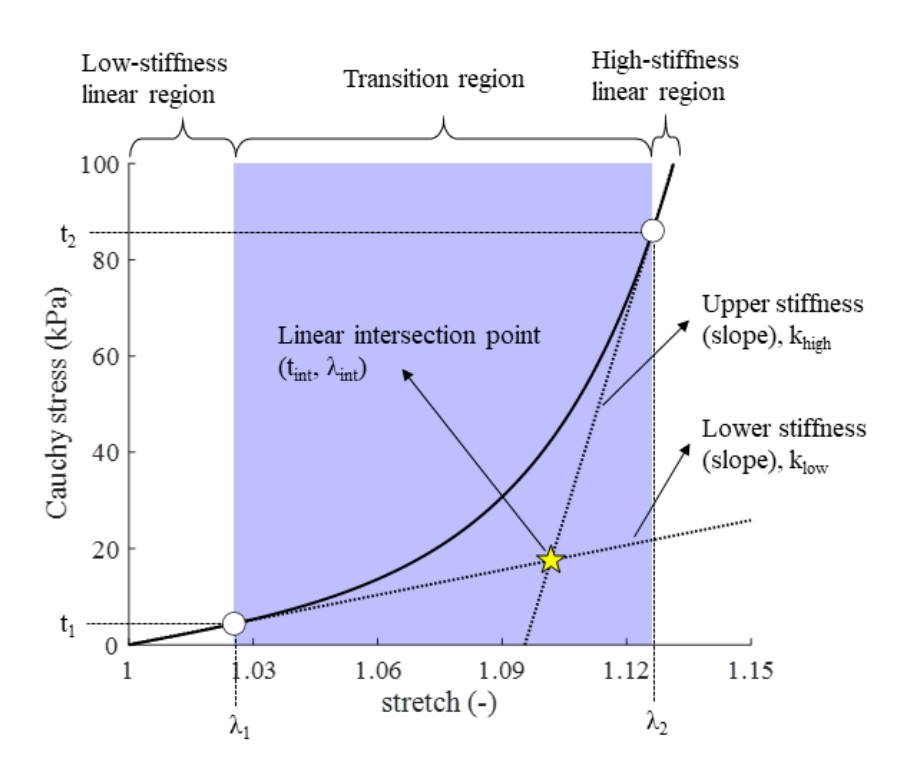


Figure 5.3: Transition regions and points of interest for a representative (control) stress-stretch model curve.

5.1.8 Histology and tissue composition

Following mechanical testing, the stretched, decellularized rings were fixed in 10% formalin for 96 hours, before being moved to 30% ethanol. The decellularized rings were then processed overnight and embedded in paraffin blocks. Slides were sectioned at 5-6 µm and stained for collagen and elastin fibers, as follows. Sections were incubated overnight at 60°C, and deparaffinized and rehydrated through xylene and alcohol series. Heat-mediated antigen retrieval was performed with 10mM citrate buffer and non-specific antigens blocked with blocking buffer (1% Roche Blocking Buffer, 1% BSA, 5% normal goat serum, 0.04% Tween in TBS). Primary antibody was diluted 1:100 in blocking buffer and incubated overnight at 4°C. Antibodies used were collagen I (ab34710, Abcam) and elastin (ab21610, Abcam). Slides were subsequently incubated with Alexa Fluor 488 goat anti-rabbit secondary antibody (A11070, Thermo Fisher Scientific), diluted 1:500 in blocking buffer. Four to six images were taken per bladder section, and three regions of interest (ROI) selected per image. The percentage of ROI with positive staining was calculated using ImageJ.

Currently, this process has been done only for the 6 months time point.

Because the samples used for mechanical testing had been decellularized, we were not able to obtain an overall collagen area fraction for this group. Instead, a separate group of animals were provided the same treatment (either left untreated, n = 5, or given the 1x40Gy dose of irradiation, n = 5). These animals were given 6 months of recovery time, matching the cohort described above, and had their bladders paraffinized and sectioned in the same manner—though not decellularized. Finally, these samples were stained with a Masson's trichrome stain and imaged using ImageJ, to calculate a total area fraction of collagen for bladders affected by irradiation.

5.2 RESULTS

Radiation treatment was well-tolerated by all animals. No change in body weight or behavior was noted after radiation exposure. The irradiated mice developed skin discoloration at beam entrance and exit sites by 10 weeks after irradiation as shown previously [157]. Two mice, 1 irradiated and 1 untreated, were lost prior to the 6-months time point due to complications unrelated to irradiation. Approximately 30% of mice developed allopecia, which is inherent to the inbred C57BL/6 strain [134].

5.2.1 Micturition patterns

To determine if the observed irradiation-induced bladder stiffness altered overall bladder function, we performed void spot assays on untreated and irradiated mice. The void spot assay is a non-invasive commonly used test to assess overall bladder function in rodents [127]. Only at the 6 months time point, over a four-hour period, mice that had been exposed to irradiation had an increased number of urine spots in comparison to the untreated mice, Fig. 5.4. In addition, irradiated mice voided smaller volumes of urine as noted by the average voided volume, without significantly changing the total voided volume during the assay Fig. 5.4. The change in micturition behavior started at 3 months post-irradiation and became more apparent and significant as time progressed.

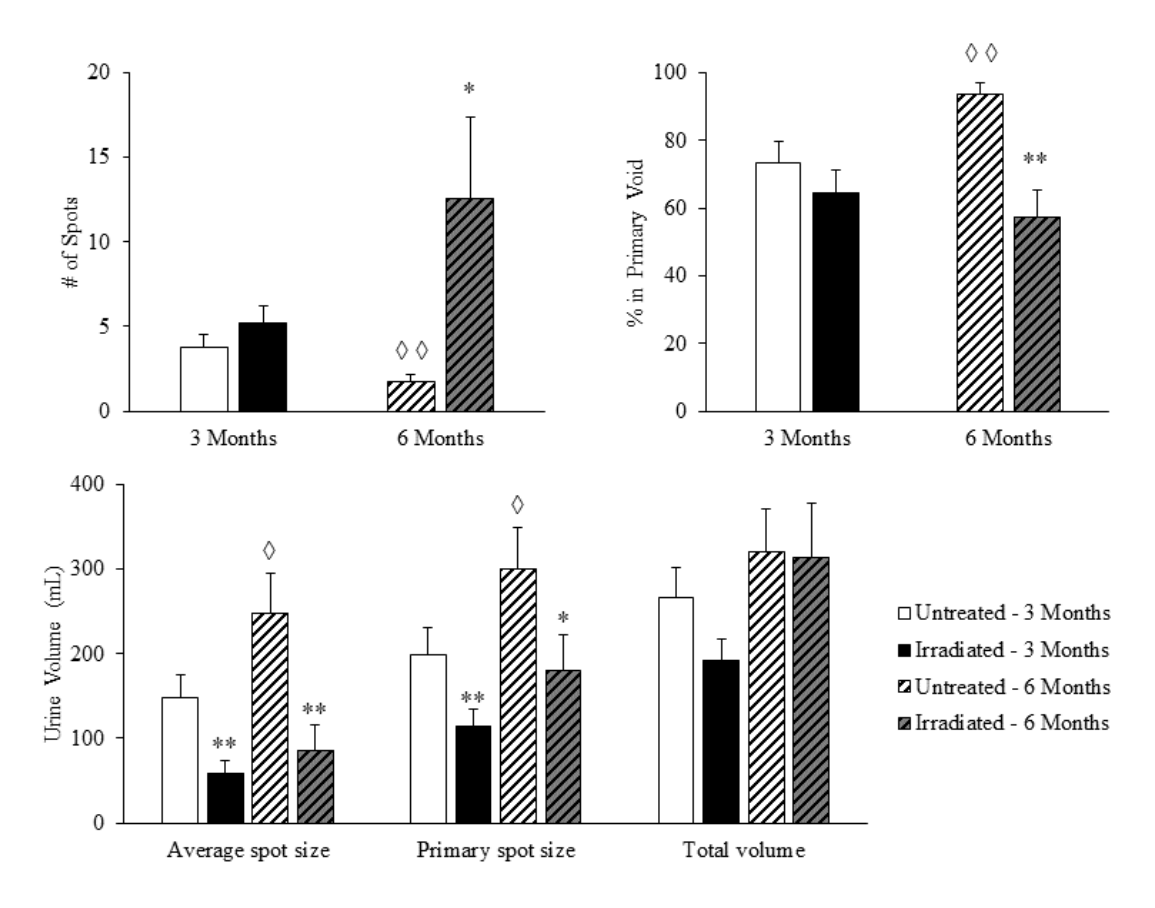


Figure 5.4: Changes in micturition behavior by radiation treatment and recovery time. Statistical symbols: *P < 0.1, compared to untreated, **P < 0.05, compared to untreated, $\diamond P < 0.1$, compared to 3 months, $\diamond \diamond P < 0.05$, compared to 3 months.

5.2.2 Changes to effective bladder wall radius

The process of decellularization significantly increased the bladder wall radius for all treatment and recovery time groups Fig. 5.5. While the irradiated tissue had no change in radius related to time, the untreated group had a significant increase in both the intact tissue and isolated ECM from 3 to 6 months. Finally, the isolated ECM of the irradiated tissue had a singificantly smaller radius than their respective untreated group at 6 months post-treatment.

5.2.3 Changes to stress-stretch curves and constitutive parameters

In order to estimate the changes to bladder ECM mechanics in terms of a constitutive model, the final 20% loading curve was interpolated into 10 points within the highest common range

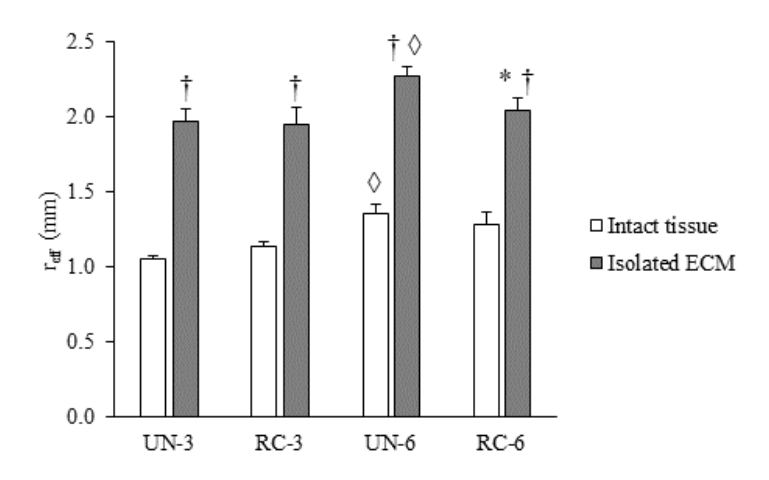


Figure 5.5: Changes to effective bladder radius, caused by radiation treatment, recovery time, and decellularization (average +/- standard error). Statistical symbols: *P < 0.05, compared to untreated, $\diamond P < 0.05$, compared to 3 months, $\dagger P < 0.05$, compared to intact tissue.

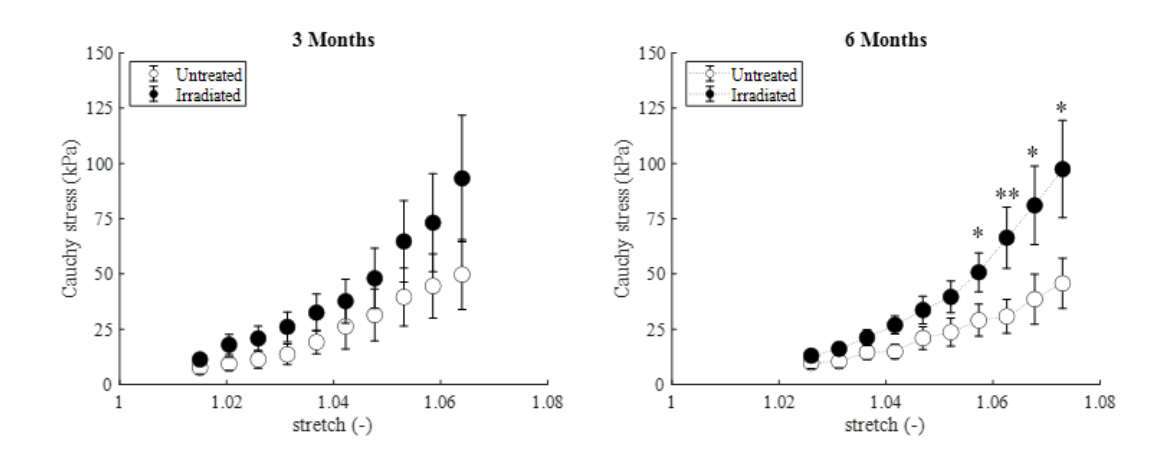


Figure 5.6: Average +/- standard error stress-stretch curves for all samples. *P < 0.1, **P < 0.05.

of stretch for each sample. This allowed for a fitting of the model that was common—with regard to preconditioning—across all samples. Fig. 5.6 shows the average and standard error for each group from these interpolated curves. At 3 months post-radiation, there were no significant differences between the untreated and irradiated tissues. At 6 months, though, at high stretches, the irradiated tissue showed a significantly higher amount of stress than the untreated tissue, indicating an increased stiffness of the extracellular matrix induced by the radiation treatment. There were no changes in either the untreated or the irradiated groups related to time.

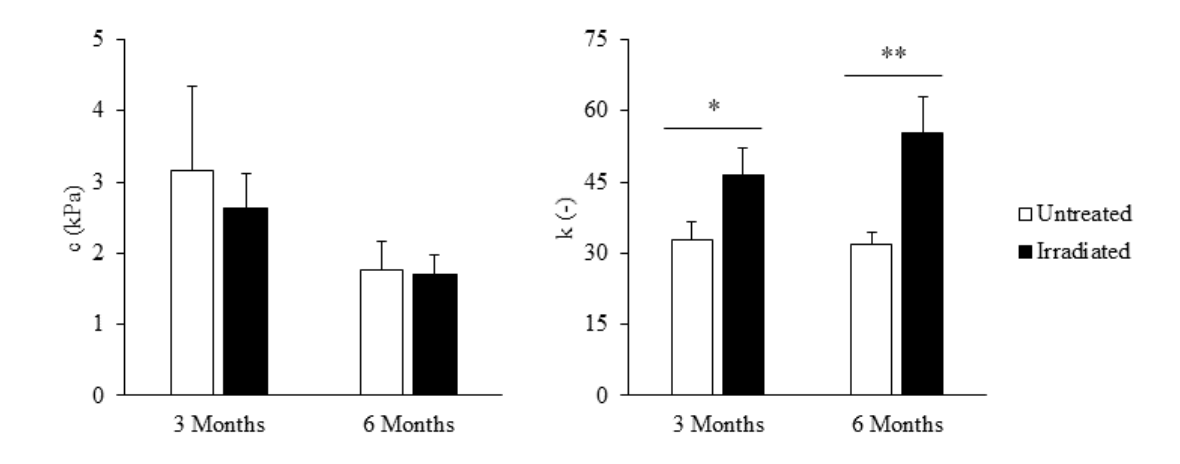


Figure 5.7: Average +/- standard error parameters from the constitutive model. *P < 0.1, **P < 0.05.

The full final 20% loading curve of each sample was fitted to the previously mentioned constitutive model with parameters c and k. These fits had normalized root mean square deviations of 2-11%. In regard to both time and radiation treatment, there were no changes to parameter c, Fig. 5.7. Parameter k, however, was dependent on radiation treatment. Specifically, k was higher in the irradiated tissue, as compared to the untreated tissue. This result was slight at the 3 months timepoint (P < 0.1), but significant by 6 months (P < 0.05). In this model, an increase in k suggests an increase in tissue stiffness at higher stresses, as discussed in Chapter 4.

5.2.4 Transition regimes and tissue stiffness

Using the constitutive model, the curves were separated into linear and transitional regimes, which assisted in identifying where, specifically, the bladder ECM mechanics were altered, within a range of physiologically relevant stresses. Each simulated stress-stretch curve was separated into the three regimes through identification of the points mentioned in the methods, Fig. 5.3. In general, the stretches $(\lambda_1, \lambda_2, \lambda_{int}, \text{ and } \lambda_{max})$ were all lower in the irradiated curves, as compared to the untreated, Fig. 5.8. However, this was only a significant decrease at 6 months. The corresponding stress values for these points $(t_1, t_2, t_{int}, \text{ and } t_{max})$ showed no significant changes related to radiation

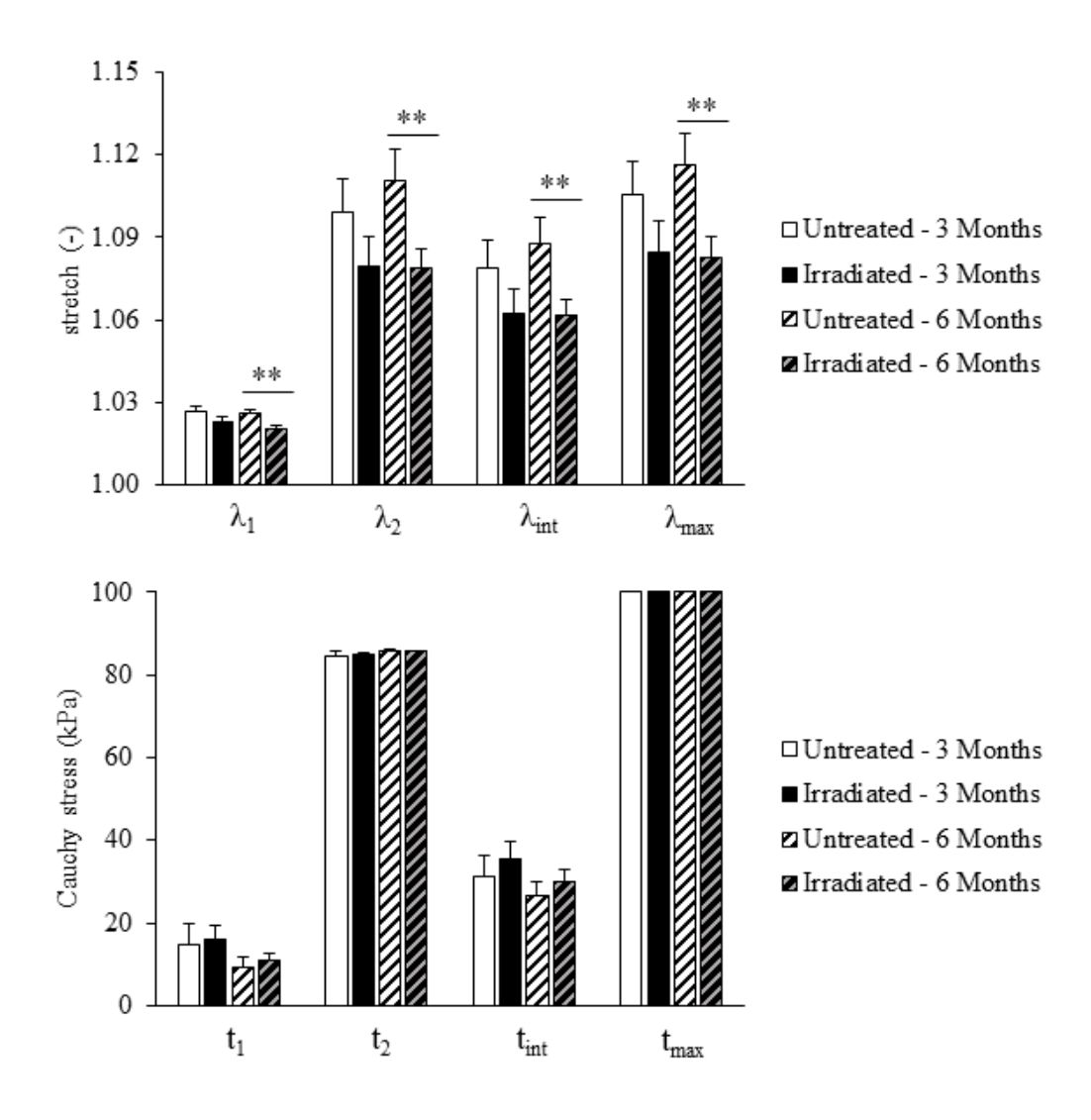


Figure 5.8: Average +/- standard error regime endpoints. **P < 0.05

treatment. Changes in these points' locations were insignificant with respect to time.

Stiffness in the lower and upper linear regions were increased on average in the irradiated groups, compared to the untreated groups, Fig. 5.9. This increase in stiffness, however, was only significant for the higher region at 6 months post-treatment. Again, there were no changes in stiffness with respect to time.

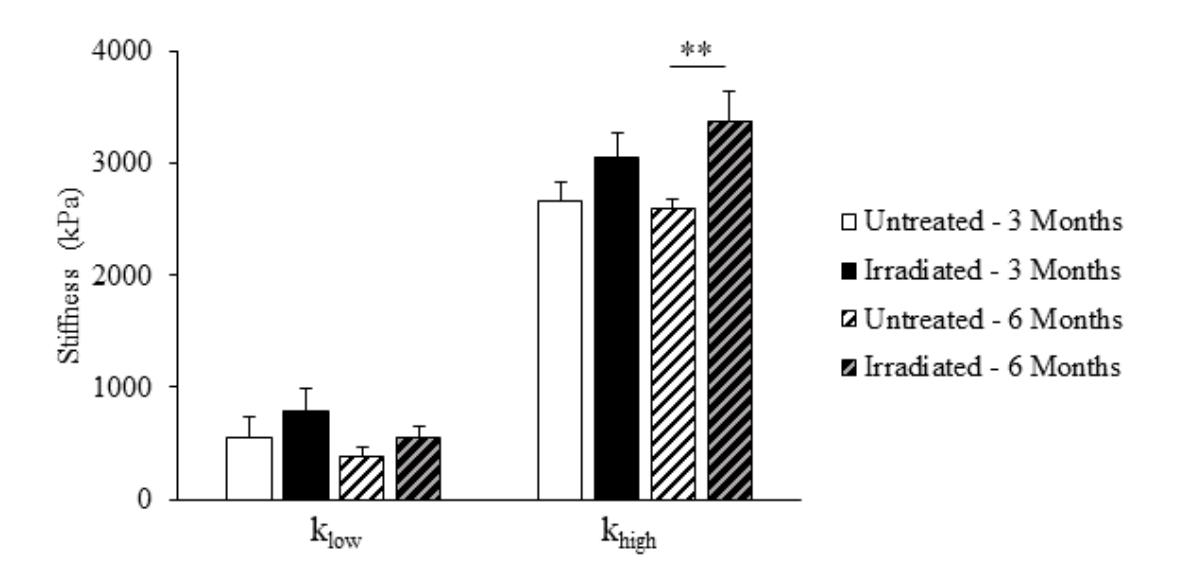


Figure 5.9: Average +/- standard error low and high stiffnesses of the consitutive model stress-stretch curves. **P < 0.05.

5.2.5 Histology and tissue composition

Analysis of the collagen I and elastin content of the decellularized and stretched rings showed no significant difference associated with irradiation, Fig. 5.10. However, the second cohort of animals showed a significant fibrosis caused by irradiation, Fig. 5.10. Currently, this section of the study is ongoing and we are unsure of the impact of recovery time on these results.

5.3 DISCUSSION

The aim of this study was to identify and characterize changes to the mouse bladder following onset of radiation cystitis, related to bladder extracellular matrix remodeling and mechanical behavior. To do so, we measured several mechanical, histological, and micturition parameters. Generally, we have found that radiation causes a time-dependent (progressive) change to micturition patterns (increased void frequency with decreased void volume), an overall increase in collagen deposition, eventually leading to an increase in extracellular matrix stiffness.

The micturition experiment presented here, showed a transition from a primary voiding spot

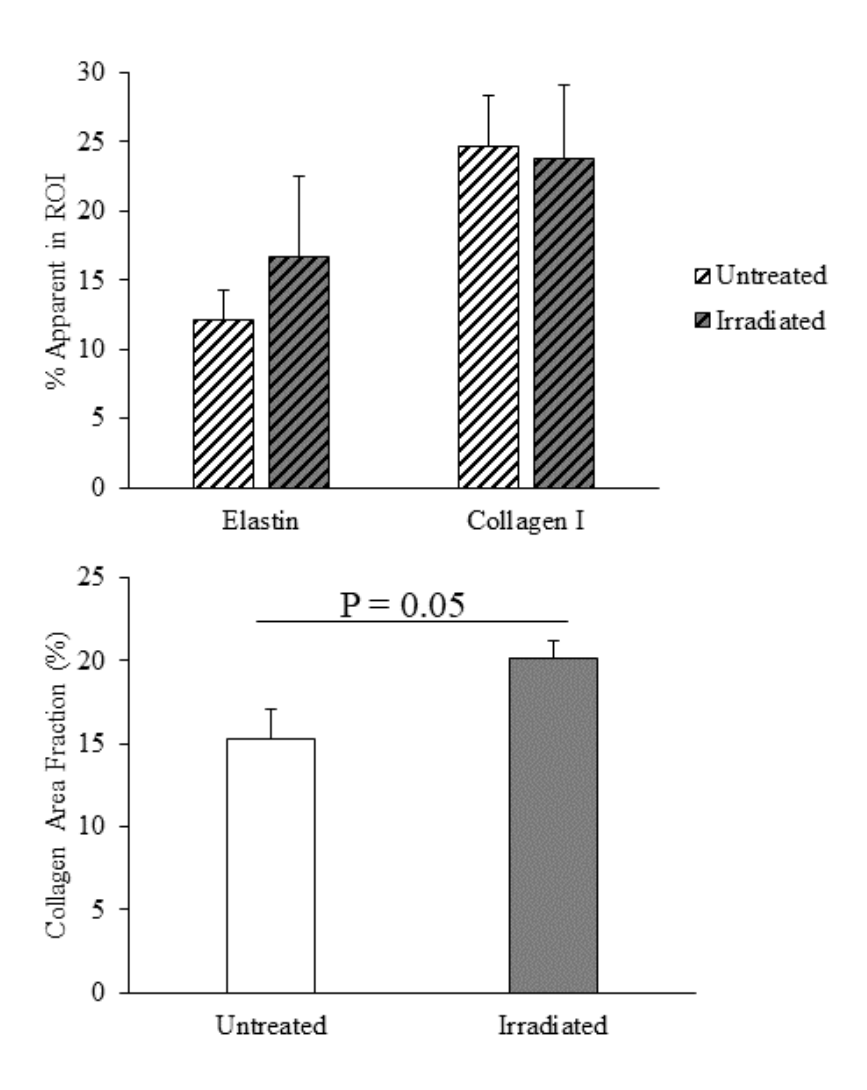


Figure 5.10: Top: Elastin and collagen I content in the decellularized rings. Bottom: Total collagen area fraction of the non-decellularized, second cohort of bladders.

preference to a voiding pattern with many small spots, caused by irradiation treatment. This transition begins by 3 months, and progresses through the 6 months time point. An interpretation of this transition of mouse voiding behavior is that these mice have decreased bladder capacity and increased voiding frequency. This is apparent through combining the overall changes: maintaining of the total voided urine volume (no changes in urine production) with a decrease in void spot size (more frequent, but smaller voids). This is similar to what humans experience, often reporting symptoms of increased frequency and decreased bladder capacity [158].

Average stress-stretch curves of the irradiated animals showed higher stiffness in the irradiated tissue samples, as compared to the untreated, which became significant at 6 months post-treatment. The constitutive model showed no changes to parameter c, which dominates mechanical behavior at low stress. Conversely, parameter k, which dominates behavior at high stresses, was increased in the irradiated tissue, which became significant at 6 months. Overall, these results indicate that radiation cystitis causes a progressive increase in stiffness in the extracellular matrix of the bladder that is focused on the upper-end of the stress-stretch curve.

This concept of radiation-induced stiffening at high stresses is reinforced by the boundaries and stiffnesses of the regimes measured from the model curves. While the stress-value of the boundaries is conserved across treatment and recovery time, each point has a stretch value that is significantly decreased by radiation treatment; this is significant only at 6 months. Additionally, the stiffnesses of the two linear regions is increased with radiation—which is significant in the upper linear region. This type of alteration to the stress-stretch behavior of the extracellular matrix could be indicative of a decreased bladder capacity, a common hallmark of radiation cystitis [115], as the tissue is reaching maximum in vivo stress at a much lower stretch.

The addition of the transition regions was useful in identifying connections between the micturition and mechanical data sets. Specifically, we see that at the maximum stress (100kPa) that may be seen physiologically, the irradiated bladders have a significantly lower stretch. This indicates that animals with irradiated bladders will experience higher stress in their bladders at a lower stretch (or urine volume), meaning that these animals may have an urge to void earlier than their untreated

counterparts. This was apparent from the micturition data as well, in the form of decreased average spot size, and increased numbers of spots. The irradiated animals voided more frequently and with lower volumes than their controls, and this was likely due to the increased stiffness of the bladder tissue. This behavior (both mechanical and micturition) was present at 3 months and severe by 6 months, which illustrates a progressiveness of the disease that is also seen in humans.

Bladder tissue mechanical behavior is dominated primarily by elastin fibers at low stresses and collagen fibers at high stresses [19, 96, 149]. This is due to the structure of the bladder extracellular matrix—collagen fibers are tightly coiled and wavy, and straighten out/engage as deformation is applied. Therefore, the results of this study (i.e. increased stiffness caused by radiation that occurs primarily at high stresses) indicate that remodeling of the extracellular matrix caused by radiation treatment includes changes to collagen content or structure. This type of remodeling differs from other commonly studied diseases in bladder mechanics, such as spinal cord injuries or diabetes, where the bladder becomes loose due to a depletion of collagen fibers and an increase in elastin [46, 96, 141, 148, 84, 144].

From the second cohort used in the histological section for collagen area fraction measurement, we can see that this dosage of irradiation causes significant fibrosis of the urinary bladder in mice, which is consistent with what has been seen previously in the literature [156, 159, 75]. Conversely, according to the measurements taken from the decellularized rings, we can see that there is no change to elastin content. These results are consistent with what has been shown in the changes to bladder mechanics—specifically, an increase in stiffness at higher stresses is indicative of an increase in collagen content, while no changes to stiffness at lower stresses, is indicative of unchanged elastin content. Finally, we have also seen that there is no significant change to the amount of collagen I, specifically. This may be because both collagen I and collagen III are being deposited in relatively similar amounts, which would not be detected in decellularized tissue.

An interesting result is the lack of alterations to the mechanics of the tissue at 3 months, followed by significant stiffening of the tissue at 6 months post-treatment. This indicates a progression of disease in this mouse model, similar to what humans experience with RC. Patients with RC tend

to have diminished bladder capacity (potentially caused by extracellular matrix stiffening) that worsens and becomes more apparent over time [158].

5.3.1 LIMITATIONS

This study does have several limitations. First, we include two time points in our experiments, 3 and 6 months following treatment. While we observe time-dependent (progressive) onset of RC, we are currently unable to determine specifically when symptoms or remodeling may begin, or how it will progress after the 6 month time point. In future studies, we plan to address this issue with more time points—potentially starting at 2 weeks post-treatment, and extending to at least 12 months post-treatment.

Second, this study includes only female mice, while RC affects both males and females. Given that a common reason for pelvic radiation therapy is prostate cancer, it is important to look into performing a study like this on males as well. The reason for using female mice instead of males is the ease of performing a void spot assay, as male mice tend to urinate in a territorial marking fashion.

Finally, the use of a uniaxial mechanical test and isotropic constitutive model has its own limitations. Of course, the urinary bladder is not an isotropic material. However, using this test and model allows us to compare the overall composition of the tissue in one direction. This is a particular limitation due to the available experimental facilities in our laboratory.

5.4 CONCLUSIONS

In this study, we have shown that a previously developed model of radiation cystitis [157] causes changes to bladder function that are consistent with humans [158], primarily increased voiding frequency and decreased bladder capacity. These changes are also associated with an increase in collagen fiber deposition, though no changes to elastin content. This also leads to an increase in bladder extracellular matrix stiffness at high stress, which may be responsible for the decreased capacity of the bladder. Additionally, we have shown that these changes, like in humans,

are progressive and worsen over time.

CHAPTER 6

CONCLUSIONS AND FUTURE WORK

Through this work, we have established several novel concepts in left ventricle and urinary bladder constitutive modeling. First, we showed the need to include mechanical interactions between the collagen fibers and the myocytes when modeling the left ventricle. Second, in both healthy and pathological (hypertensive) conditions, we showed that the left ventricle's intact tissue, isolated collagen fibers, and isolated myocytes each have their own unique and significantly different unloaded (opening angle) configurations. Third, we have shown that the constitutive behavior of the urinary bladder in type II diabetes (both with and without obesity) is similar to what has previously been established in type I diabetes. Specifically, diabetic cystopathy has been shown to cause a significant decrease in tissue stiffness. Finally, in the previous chapter, we have shown the first known representation of the altered mechanical behavior in radiation therapy-treated bladder tissue, and the resulting progressive increase in tissue stiffness. In the following section, I will discuss the plans for future work in constitutive modeling of these tissues.

6.1 UPDATED LEFT VENTRICLE INTER-CONSTITUENT MECHANI-CAL INTERACTION

In Chapter 2, we developed a novel concept for modeling interactions between myocytes and collagen fibers in the left ventricle. In doing so, we utilized previously published data from stress-strain testing of an isolated collagen fiber [131] and an isolated myocyte [8] to estimate material parameters. While this was useful as a first step toward establishing this modeling framework, these data may not be the best-suited to represent tissue samples for this study, as we are working with the entire matrices of these isolated constituents, not single fibers. The differences between these estimated material parameters from the literature and the mechanical data we have observed can be seen in Fig. 6.1. Instead, we will build on the data set for the material parameters estimated in Chapter 3. In this study, we mechanically tested the isolated myocytes and collagen fibers of

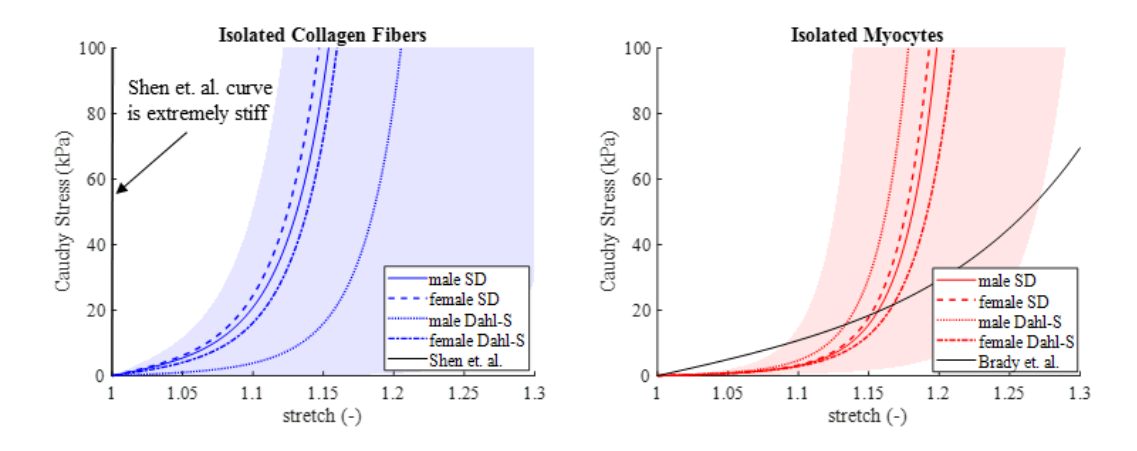


Figure 6.1: Observed mechanical data vs. material parameters obtained from literature for isolated collagen fibers [131] and isolated myocytes [8]. Shaded regions represent standard error model predictions.

the left ventricle from male and female Sprague Dawley and Dahl-salt sensitive rats fed both a control and high fat diet. Currently, each group has only two or three samples. Additionally, we have combined the control and high fat diet fed Dahl-SS parameters due to a low volume of samples. We plan to test a larger number of each in order to validate that the material parameters of the left ventricles of these groups do not change with diet (or, possibly, show that they do). In order to obtain a more meaningful data set, each group should have at least five samples. Once the mechanical tests are complete, we should have a set of mechanical parameters for all groups (male/female, healthy/hypertensive, control/high fat diet, collagen/myocytes).

Once the test groups have a meaningful amount of mechanical data, we can estimate material parameters of each group from a constitutive model. Rather than a Demiray model for both constituents, as proposed in Chapters 2 and 3 [26], we propose the use of a two-fiber family of collagen model for the isolated collagen fibers [62] while using the Demiray model for the myocytes, now with the updated mechanical data. Again, we will use a weighted average strain energy function for the intact tissue and, in full, the strain energy functions will be

$$W = \phi^c W^c + \phi^m W^m \tag{6.1}$$

$$W^{m} = c \left[e^{k(I_{1} - 3)} - 1 \right] \tag{6.2}$$

$$W^{c} = \frac{c_{1}}{2} (I_{1} - 2) + \sum_{k=1,2} \frac{c_{1}^{k}}{4c_{2}^{k}} \left[e^{\left\{ c_{2}^{k} ((\lambda^{k})^{2} - 1)^{2} \right\}} - 1 \right]$$
 (6.3)

$$\lambda^{k} = \sqrt{\lambda_{\theta}^{2} sin^{2}(\alpha^{k}) + \lambda_{z}^{2} cos^{2}(\alpha^{k})}$$
(6.4)

where ϕ^c and ϕ^m are the collagen and myocytes area fractions for each group measured from histology, c and k are the material parameters for isolated myocytes, and c_1 , $c_1^{(1,2)}$, and $c_2^{(1,2)}$ are the material parameters for collagen, and $\alpha^{(1)}$ and $\alpha^{(2)}$ are the directions of the two fiber families of collagen. If we assume that the two fiber families are symmetric about the z-axis, then $c_1^{(1)} = c_1^{(2)}$, $c_2^{(1)} = c_2^{(2)}$, and $\alpha^{(1)} = -\alpha^{(2)}$. After optimizing each of these parameters to fit the mechanical data, the steps from Chapter 2 can be repeated to estimate updated measurements of the interaction terms α^ξ for healthy males, and repeat these steps again for females and the hypertensive models. Also, in Chapter 2, we discussed the inter-constituent interaction only in terms of the interaction parameter representing an isotropic tension or compression, α^ξ . Specifically, the deformation gradients from the isolated constituents' closed configurations to the combined, intact tissue closed configurations from this chapter are

$$\boldsymbol{F} = \alpha^{\xi} \begin{bmatrix} \frac{\partial \rho}{\partial \rho^{\xi}} & 0 & 0 \\ 0 & \frac{\rho}{\rho^{\xi}} & 0 \\ 0 & 0 & \lambda^{\xi} \end{bmatrix}. \tag{6.5}$$

While the values for α^{ξ} have been shown to be non-negligible, we note that this deformation gradient in itself implies an interaction even excluding the α^{ξ} parameter. In our future work pertaining to this modeling framework, we plan to discuss the mechanical interaction of these two constituents in terms of both α^{ξ} and each component inside the deformation gradient.

Following the establishment of the inter-constituent interactions, we plan to construct a finite element model of the left ventricle that can display distributions of stress across the wall associated with the deformation from the opening angle to the closed and circumferentially loaded ring.

6.2 INTER-CONSTITUENT MECHANICAL INTERACTION IN THE URINARY BLADDER

Compared to the left ventricle, constitutive modeling of the urinary bladder has not been explored as deeply in the literature. Because of this, our results thus far have employed simplified constitutive models as presented in Chapters 4 and 5 [26]. We have shown that diabetic cystopathy and radiation cystitis may cause significant decreases and increases in tissue stiffness, respectively. However, in the case of type II diabetic cystopathy, our results showed no significant changes to the extracellular matrix—in terms of area fractions of elastin and collagen fibers. Though we have seen histological evidence for radiation-induced remodeling, our diabetic results leave us to question, if it is not the quantity of extracellular matrix fibers, what is causing the changes to the mechanical behavior of the tissues?

One possible way to obtain an answer to this question, would be to create an inter-constituent interaction model for the urinary bladder, as we did for the left ventricle. However, the urinary bladder brings a new challenge: elastin fibers. Because the left ventricle wall has negligible amounts of elastin, we can focus only on the collagen fibers and myocytes. In the urinary bladder, though, the constituents of interest, mechanically, would be smooth muscle, collagen fibers, and elastin fibers. It would be logical to propose isolating each constituent and measuring the resulting geometry of ring-shaped samples, however, the small amount of elastin in the urinary bladder would likely not hold a recognizable shape. However, we can remove the collagen and smooth muscle from each tissue ring using the methods described in each of the previous chapters, and we can remove the elastin fibers through the use of the enzyme elastase. In using these tools, we would be able to create rings that have the following structures: isolated collagen, isolated muscle, collagen + muscle, muscle + elastin, elastin + collagen, and intact tissue (untreated), Fig. 6.2.

Additionally, each of these samples may have their own unique opening angle, similar to the left ventricle. Through the use of these opening angles in a similar manner as in the left ventricle studies, we can estimate the inter-constituent interactions. Briefly, each closed configuration would be allowed to reach axial and radial equilibrium and each open configuration will be in axial,

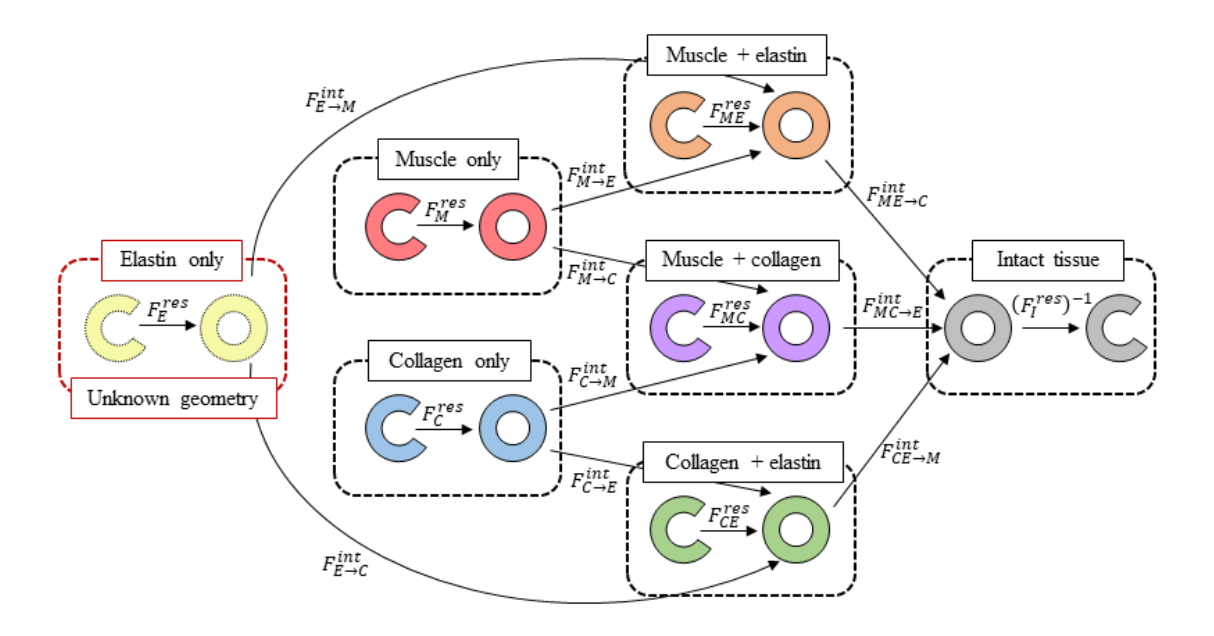


Figure 6.2: Configurations of interest and deformation gradients for estimating urinary bladder inter-constituent interactions.

radial, and bending moment equilibrium. An additional issue posed by the unknown geometry of the isolated elastin samples would be that we cannot assume we know the initial geometry of all isolated constituents and move forward through the problem as we did for the left ventricle in Chapter 2. Instead, we propose that the geometries for the closed configurations (as well as their opening angles) in the isolated collagen, isolated muscle, collagen + elastin, and muscle + elastin groups is known. From this point, we would be able to estimate the interactions without having to know the geometry or opening angle of the elastin.

Though it has not been established that residual stresses reside within urinary bladder tissue, our pilot studies have shown that while there may not be a significant opening angle in the intact tissue, there is in both the collagen + elastin (decellularized) and isolated collagen (decellularized and elastase-treated) configurations of healthy rat urinary bladders, Fig. 6.3. Similarly to the left ventricle version of this model, we could mechanically test isolated collagen fibers and isolated muscle cells to obtain material parameters for these groups. For material properties of elastin, we can use previously published mechanical data on a single elastin fiber, [74].

A successful application of this inter-constituent interaction model on the urinary bladder would

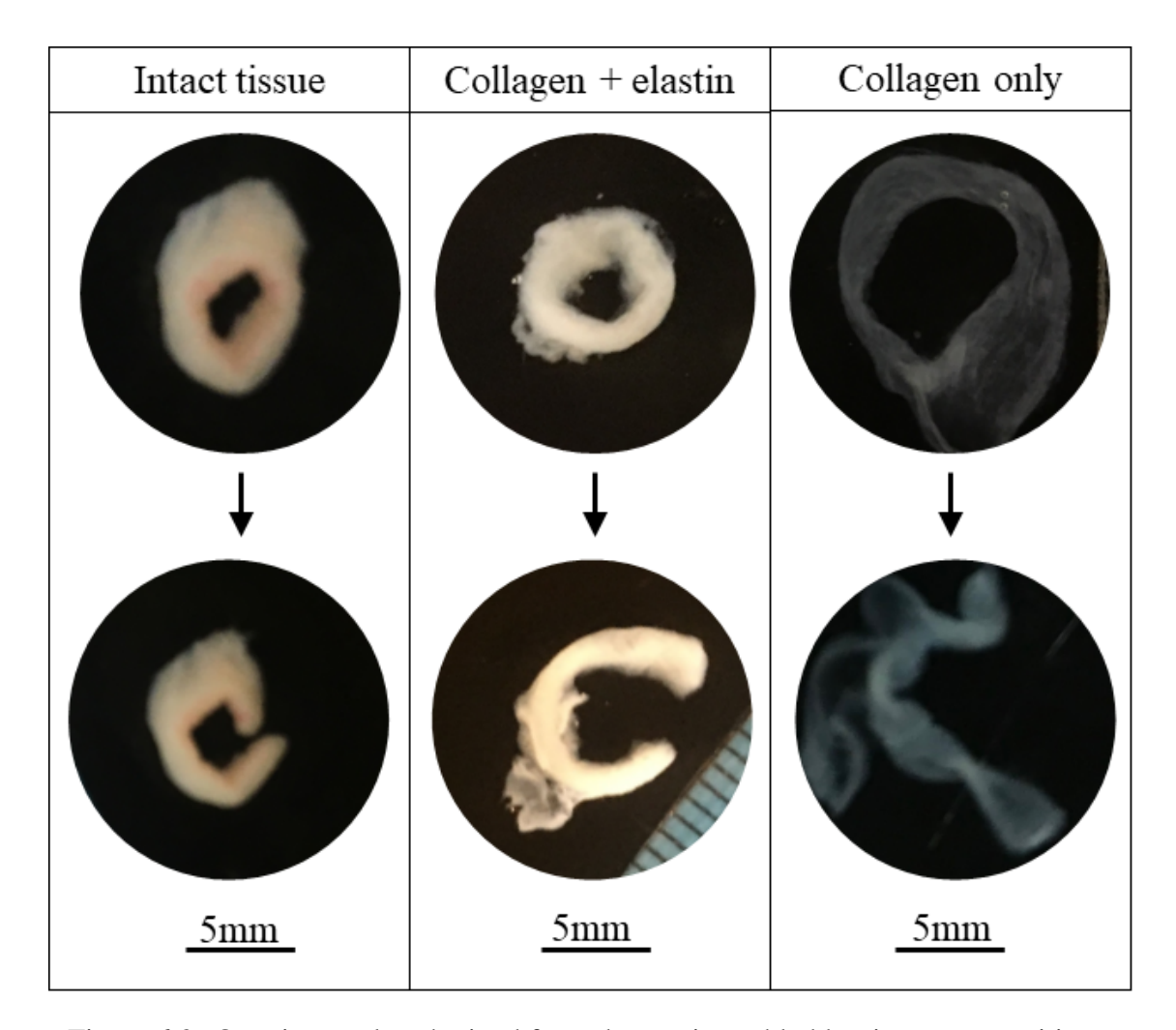


Figure 6.3: Opening angles obtained from three urinary bladder tissue compositions.

allow us to understand how smooth muscle, collagen fibers, and elastin fibers interact mechanically both in healthy and pathological—i.e. diabetic and irradiated—states.

6.3 CONCLUDING REMARKS

The research presented here has made large strides in understanding the mechanical microenvironment of soft biological tissue constituents. Specifically, we have applied constitutive models to healthy and pathologically remodeled left ventricle and urinary bladder tissue and proposed a model of the mechanical inter-constituent interactions of muscle cells, collagen fibers, and elastin fibers. This work can help inform finite element models that depend on accurate representation of the mechanical behavior of soft tissues, moving toward predictive medicine and understanding disease progression.

APPENDIX

The following appendix details the derivation and solution processes involved in completing the interaction problem described in Chapter 2.

Recall that all configurations in this problem are in cylindrical coordinates, and are either in an "open" or "closed" state with radial, circumferential, and axial directions of (R, Θ, Z) or (ρ, θ, z) , respectively. A superscript of ξ indicates a configuration of isolated constituents—either collagen fibers (c) or myocytes (m). Each configuration has a volume of

$$v = \pi(\rho_o^2 - \rho_i^2)z\tag{1}$$

or

$$V = \frac{2\pi - \Theta}{2\pi} (R_o^2 - R_i^2) Z \tag{2}$$

for the closed or open state, respectively. In equation 2, Θ refers to the opening angle of that configuration. For each deformation, we make an assumption of incompressibility, so that the determinant of the deformation gradient is equal to 1, |F| = 1. Finally, each problem will have its own equilibrium equations that will be solved in order to estimate the geometric outcome. These equilibrium equations will be a function of stress, defined by our constitutive model described in Chapter 2. Briefly, we employ the definition of Cauchy stress, T, for an incompressible material,

$$T = -pI + 2F \frac{\partial W(C)}{\partial C} F_T$$
 (3)

where p is a Lagrange multplier, I is the identity matrix, W is a strain energy function, and $C = F^T F$ is the right Cauchy-Green deformation tensor. The strain energy function used in chapter 2 is a demiray-type [26, 24] defined by

$$W(\mathbf{C}) = c \left[e^{k(I_1(\mathbf{C}) - 3)} - 1 \right]. \tag{4}$$

Two sets of the parameters c and k were optimized via a fitting to previously published stress-strain data on a single collagen fibril and a single myocyte [131, 8], to obtain c^c and k^c for collagen, and c^m and k^m for myocytes. Stress in configurations containing isolated constituents can then be calculated by simply using equation 3 and their respective constitutive model—either

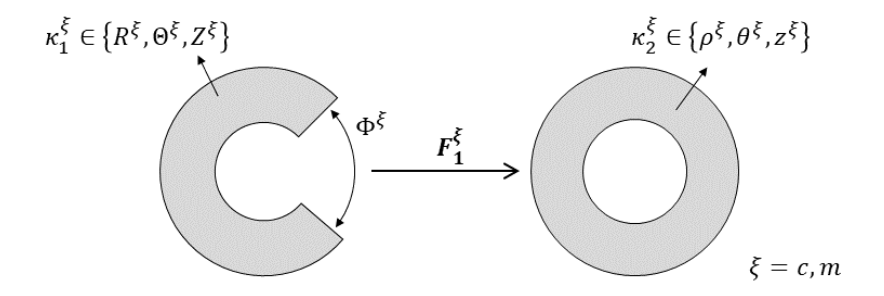


Figure .4: Configurations of interest for part 1 of the opening angle inter-constituent interaction model.

 $W^c(\mathbf{C^c}, c^c, k^c)$ or $W^m(\mathbf{C^m}, c^m, k^m)$. Stress in the intact tissue, however, must be calculated using a weighted average function for stress in the constituents through

$$T = -pI + 2\phi^{c}F^{c}\frac{\partial W^{c}(C^{c})}{\partial C^{c}}(F^{c})^{T} + 2\phi^{m}F^{m}\frac{\partial W^{m}(C^{m})}{\partial C^{m}}(F^{m})^{T}$$
(5)

where ϕ^c and ϕ^m are the area fractions of collagen fibers and myocytes, respectively, as measured from the histological analysis in Chapter 2. Finally, all problems defined in the following sections were solved using the *lsqnonlin* function on Matlab.

A.1 Open to closed isolated constituents

This section includes the solution process for solving Part 1 of 3 from Chapter 2. The configurations of interest for this part of the problem are outlined in Fig. .4. We first make an assumption that the experimental geometry of the closed configuration, κ_2^{ξ} is the true geometry. We also take the opening angle, Θ^{ξ} from the experimental value. The unknown values to solve for are, then, R_i^{ξ} , R_o^{ξ} , and $\lambda_1^{\xi} (= z^{\xi}/Z^{\xi})$. The reason for assuming true geometry to be that of the closed configuration is the imperfect ring-shape of the actual LV samples. When the physical samples reach a configuration akin to κ_1^{ξ} , they have a tendency to twist and so measurements of the radii may have larger error here. Therefore, we take the radii measurements from the closed configurations of the samples.

To begin solving for the unknown geometry, we first define the deformation gradient as

$$\boldsymbol{F_{1}^{\xi}} = \begin{bmatrix} \frac{\partial \rho^{\xi}}{\partial R^{\xi}} & 0 & 0\\ 0 & \frac{\rho^{\xi}}{R^{\xi}} \frac{2\pi}{2\pi - \Theta^{\xi}} & 0\\ 0 & 0 & \lambda_{1}^{\xi} \end{bmatrix}.$$
 (6)

An assumption of incompressibility–i.e. $V_1^{\xi}=v_2^{\xi}$ or $|F_1^{\xi}|=1$ –allows us to write

$$\rho^{\xi} = \sqrt{(\rho_i^{\xi})^2 + \frac{2\pi - \Theta^{\xi}}{2\pi} \frac{1}{\lambda_1^{\xi}} (R^{\xi} - R_i^{\xi})^2}.$$
 (7)

This provides us with an equation to translate between coordinate systems, as well as a definition for $\frac{\partial \rho^{\xi}}{\partial R^{\xi}}$, given by

$$\frac{\partial \rho^{\xi}}{\partial R^{\xi}} = \frac{2\pi - \Theta^{\xi}}{2\pi} \frac{1}{\lambda_{1}^{\xi}} \frac{R^{\xi}}{\rho^{\xi}}.$$
 (8)

Finally, our κ_2^{ξ} configuration in is radial and axial equilibrium, defined by the following equilibrium equations:

$$\int_{\rho_i^{\xi}}^{\rho_o^{\xi}} \frac{1}{\rho^{\xi}} (t_{\theta\theta}^{\xi} - t_{\rho\rho}^{\xi}) d\rho^{\xi} = 0$$

$$\tag{9}$$

$$\int_{\rho_{i}^{\xi}}^{\rho_{o}^{\xi}} \rho^{\xi} [2t_{zz}^{\xi} - (t_{\theta\theta}^{\xi} + t_{\rho\rho}^{\xi})] d\rho^{\xi} = 0.$$
 (10)

Finally, we can use equations 9 and 10, along with our definitions of stress and the deformation gradient to solve for ρ_i^{ξ} and λ_1^{ξ} . Finally, once we know these two, we can use equation 7 to solve for ρ_o^{ξ} . This part of the problem will be done twice, once for collagen fibers, and once for myocytes.

A.2 Closing and combining constituents

This section follows the closing of the isolated constituents by combining them into one closed, mixed configuration, κ_3 , as defined in figure .5. Here we know the geometry from the previous section, namely, R_i^m , R_o^m , R_i^c , R_o^c , ρ_i^m , ρ_o^m , ρ_o^c , ρ_o^c , λ_1^m , λ_1^c , Θ^m , and Θ^c . Here, we are estimating the unknown geometry of the closed, mixed configuration, κ_3 , in terms of ρ_i , ρ_o , λ_2^m (= z/z^m), and

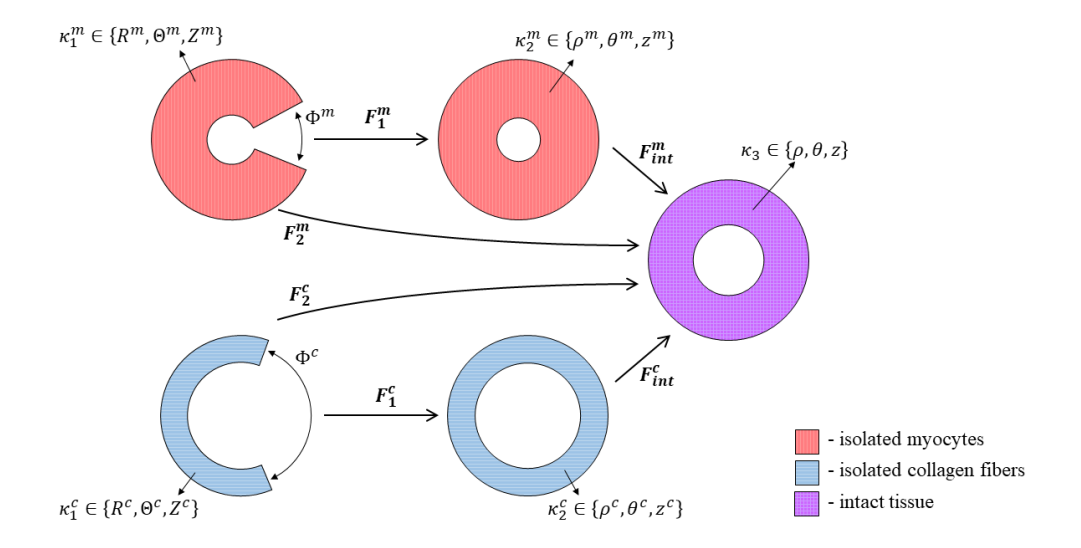


Figure .5: Configurations of interest for part 2 of the opening angle inter-constituent interaction model.

 $\lambda_2^c (= z/z^c)$. Our deformation gradients, are then defined by

$$\boldsymbol{F_{2}^{\xi}} = \boldsymbol{F_{int}^{\xi}} \boldsymbol{F_{1}^{\xi}} = \alpha^{\xi} \begin{bmatrix} \frac{\partial \rho}{\partial \rho^{\xi}} & 0 & 0 \\ 0 & \frac{\rho}{\rho^{\xi}} & 0 \\ 0 & 0 & \lambda_{2}^{\xi} \end{bmatrix} \begin{bmatrix} \frac{\partial \rho^{\xi}}{\partial R^{\xi}} & 0 & 0 \\ 0 & \frac{\rho^{\xi}}{R^{\xi}} \frac{2\pi}{2\pi - \Theta^{\xi}} & 0 \\ 0 & 0 & \lambda_{1}^{\xi} \end{bmatrix} = \alpha^{\xi} \begin{bmatrix} \frac{\partial \rho}{\partial R^{\xi}} & 0 & 0 \\ 0 & \frac{\rho}{R^{\xi}} \frac{2\pi}{2\pi - \Theta^{\xi}} & 0 \\ 0 & 0 & \lambda_{1}^{\xi} \lambda_{2}^{\xi} \end{bmatrix}, \tag{11}$$

where α^{ξ} defines the isotropic mechanical inter-constituent interaction. Similarly to part 1, we also define an incompressibility equation, equating the volumes of the open, isolated constituents to the closed, mixed configuration,

$$\rho = \sqrt{(\rho_i)^2 + \frac{2\pi - \Theta^{\xi}}{2\pi} \frac{1}{(\alpha^{\xi})^3 \lambda_1^{\xi} \lambda_2^{\xi}} (R^{\xi} - R_i^{\xi})^2},$$
(12)

which again, provides a definition for the partial derivative in the deformation gradient,

$$\frac{\partial \rho}{\partial R^{\xi}} = \frac{2\pi - \Theta^{\xi}}{2\pi} \frac{1}{(\alpha^{\xi})^{3} \lambda_{1}^{\xi} \lambda_{2}^{\xi}} \frac{R^{\xi}}{\rho}.$$
 (13)

This new configuration is also in radial and axial equilibrium, and so we apply the equilibrium equations

$$\int_{\rho_i}^{\rho_o} \frac{1}{\rho} (t_{\theta\theta} - t_{\rho\rho}) d\rho = 0 \tag{14}$$

$$\int_{\rho_i}^{\rho_o} \rho [2t_{zz} - (t_{\theta\theta} + t_{\rho\rho})] d\rho = 0.$$
 (15)

In this part of the problem, however, the stress is defined in the mixed configuration and therefore must be treated as the weighted average of the two constituents, as described in chapter 2. For this, we use our experimental values of area fractions for the weights, namely 10% collagen fibers, and 90% myocytes.

Now, as in part 1, we have our two equilibrium equations, however, we have three unknowns, ρ_i, λ_2^c , and λ_2^m (as ρ_o is a function of these three and can be solved for last using incompressibility). We can overcome this, though, by using incompressibility as a constraint on the axial stretches. Specifically, the volumes of the two constituents in their closed state must be equal to one another in order for the entire problem to work. Therefore, we can write an incompressibility equation to define λ_2^c as a function of λ_2^m , and continue to solve the problem for the three unknowns, now with a third equation, which we derive from the incompressibility equation 12. These two incompressibility functions

$$\rho_o = \sqrt{\rho_i^2 + \frac{2\pi - \Theta^c}{2\pi} \frac{1}{(\alpha^c)^3 \lambda_1^c \lambda_2^c} (R_o^c - R_i^c)^2} = \sqrt{\rho_i^2 + \frac{2\pi - \Theta^m}{2\pi} \frac{1}{(\alpha^m)^3 \lambda_1^m \lambda_2^m} (R_o^m - R_i^m)^2}$$
(16)

can be rewritten to define this third equation,

$$\lambda_2^c = \frac{2\pi - \Theta^c}{2\pi - \Theta^m} \frac{(\alpha^m)^3 \lambda_1^m \lambda_2^m}{(\alpha^c)^3 \lambda_1^c} \frac{R_o^c - R_i^c)^2}{(R_o^m - R_i^m)^2}.$$
 (17)

Finally, we can solve for ρ_i , λ_2^m , and λ_2^c using equations 14, 15, and 17, then use incompressibility to estimate ρ_o .

A.3 Opening the mixture

In the final section of this appendix, we will describe the third part of the opening angle problem: solving for the geometry of the open mixture, defined by κ_3 in Fig. .6. Here we know all of the geometry we have previously defined, R_i^m , R_o^m , Θ^m , R_i^c , R_o^c , Θ^c , ρ_i^m , ρ_o^m , ρ_i^c , ρ_o^c , ρ_i , ρ_o , λ_1^m , λ_2^m , λ_1^c , and λ_2^c . Now, we must solve for the geometry in the open mixture, R_i , R_o , λ_3 (= Z/z), and Θ .

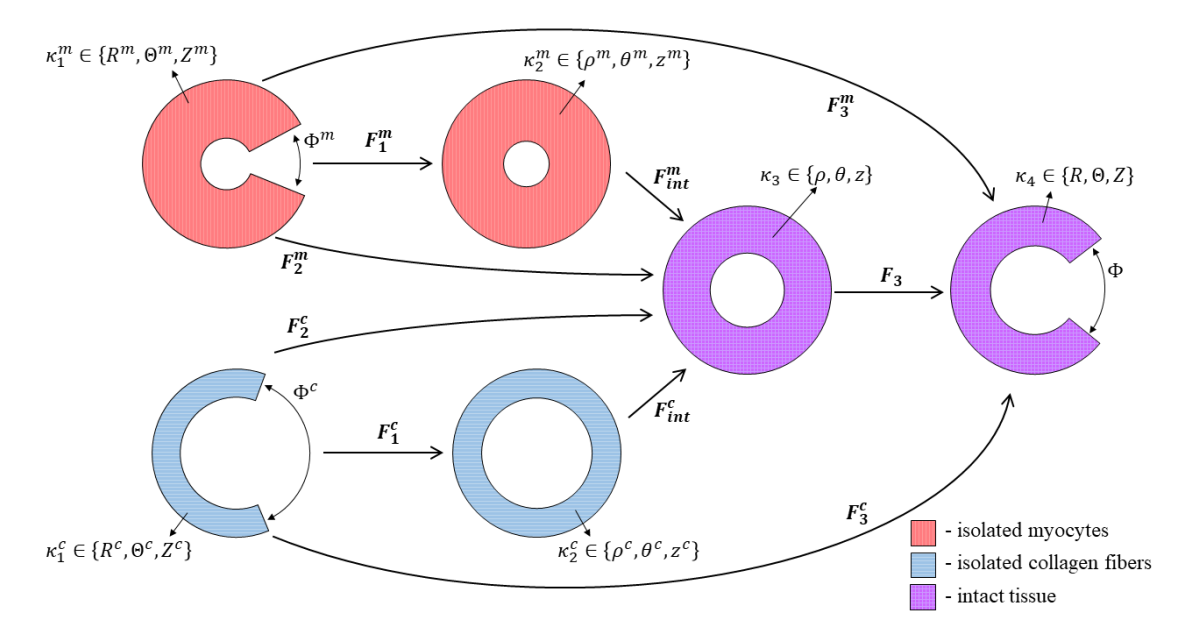


Figure .6: Configurations of interest for part 3 of the opening angle inter-constituent interaction model.

Again we define our deformation gradient,

$$\boldsymbol{F_{3}^{\xi}} = \boldsymbol{F_{3}F_{int}^{\xi}F_{1}^{\xi}} = \begin{bmatrix} \frac{\partial R}{\partial \rho} & 0 & 0\\ 0 & \frac{R}{\rho} \frac{2\pi - \Theta}{2\pi} & 0\\ 0 & 0 & \lambda_{3} \end{bmatrix} \alpha^{\xi} \begin{bmatrix} \frac{\partial \rho}{\partial \rho^{\xi}} & 0 & 0\\ 0 & \frac{\rho}{\rho^{\xi}} & 0\\ 0 & 0 & \lambda_{2}^{\xi} \end{bmatrix} \begin{bmatrix} \frac{\partial \rho^{\xi}}{\partial R^{\xi}} & 0 & 0\\ 0 & \frac{\rho^{\xi}}{R^{\xi}} \frac{2\pi}{2\pi - \Theta^{\xi}} & 0\\ 0 & 0 & \lambda_{1}^{\xi} \end{bmatrix}$$

$$= \alpha^{\xi} \begin{bmatrix} \frac{\partial R}{\partial R^{\xi}} & 0 & 0\\ 0 & \frac{R}{R^{\xi}} \frac{2\pi - \Theta}{2\pi - \Theta^{\xi}} & 0\\ 0 & 0 & \lambda_{1}^{\xi} \lambda_{2}^{\xi} \lambda_{3} \end{bmatrix}.$$

$$(18)$$

Our incompressibility equations again connect the open, isolated constituents to our newest configuration,

$$R = \sqrt{R_i^2 + \frac{2\pi - \Theta^{\xi}}{2\pi - \Theta}} \frac{1}{(\alpha^{\xi})^3 \lambda_1^{\xi} \lambda_2^{\xi} \lambda_3} (R_o^{\xi} - R_i^{\xi})^2, \tag{19}$$

and, again, provide us with a definition of the partial derivative in our deformation gradient,

$$\frac{\partial R}{\partial R^{\xi}} = \frac{2\pi - \Theta^{\xi}}{2\pi - \Theta} \frac{1}{(\alpha^{\xi})^3 \lambda_1^{\xi} \lambda_2^{\xi} \lambda_3} \frac{R^{\xi}}{R}.$$
 (20)

In this final part, our configuration, κ_3 , is now in radial, axial, and bending moment equilibrium,

$$\int_{R_i}^{R_O} \frac{1}{R} (t_{\Theta\Theta} - t_{RR}) dR = 0$$
 (21)

$$\int_{R_i}^{R_O} R[2t_{ZZ} - (t_{\Theta\Theta} + t_{RR})] dR = 0$$
 (22)

$$\int_{R_i}^{R_O} Rt_{\Theta\Theta} dR = 0. \tag{23}$$

We can use these three equations to solve for the unknown variables, R_i , λ_3 , and Θ , then use incompressibility to find R_o . However, this new equilibrium equation for bending moment, equation 23, is the first in this problem that does not allow for cancellation of the Lagrange multiplier included in the definition of Cauchy stress, Eq. 3. Therefore, we must define it here. First, we start with the basic radial equilibrium equation (prior to the integration that provides us with equation 21)

$$\frac{\partial t_{RR}}{\partial R} - \frac{t_{\Theta\Theta} - t_{RR}}{R} = 0. \tag{24}$$

Here, we can separate the first stress term from its LaGrange multiplier, p, to obtain

$$\frac{\partial(-p+\bar{t}_{RR})}{\partial R} - \frac{t_{\Theta\Theta} - t_{RR}}{R} = 0. \tag{25}$$

where we can define \bar{t}_{RR} as the radial stress without its associated LaGrange multiplier. Then, we can split p from the rest of the equations and integrate both sides,

$$\int \frac{\partial p}{\partial R} dR = \int \left[\frac{\partial \bar{t}_{RR}}{\partial R} - \frac{t_{\Theta\Theta} - t_{RR}}{R} \right] dR, \tag{26}$$

which can be simplified to

$$p(R) = \bar{t}_{RR} - \int \frac{t_{\Theta\Theta} - t_{RR}}{R} dR.$$
 (27)

This can be added into equation 23, and finally we can solve for the unknowns using the equilibrium and incompressibility equations.

BIBLIOGRAPHY

BIBLIOGRAPHY

- [1] Kibrom M Alula, Rebecca Biltz, Hui Xu, Hannah Garver, Erinn L Laimon-Thomson, Gregory D Fink, and James J Galligan. Effects of high-fat diet on sympathetic neurotransmission in mesenteric arteries from dahl salt-sensitive rat. *Autonomic Neuroscience*, 222:102599, 2019.
- [2] Reza Avazmohammadi, Michael R Hill, Marc A Simon, Will Zhang, and Michael S Sacks. A novel constitutive model for passive right ventricular myocardium: evidence for myofiber–collagen fiber mechanical coupling. *Biomechanics and modeling in mechanobiology*, 16(2):561–581, 2017.
- [3] Anna L Beale, Shane Nanayakkara, Louise Segan, Justin A Mariani, Micha T Maeder, Vanessa van Empel, Donna Vizi, Shona Evans, Carolyn SP Lam, and David M Kaye. Sex differences in heart failure with preserved ejection fraction pathophysiology: a detailed invasive hemodynamic and echocardiographic analysis. *JACC: Heart Failure*, 7(3):239–249, 2019.
- [4] C Bellini, J Ferruzzi, S Roccabianca, ES Di Martino, and JD Humphrey. A microstructurally motivated model of arterial wall mechanics with mechanobiological implications. *Annals of biomedical engineering*, 42(3):488–502, 2014.
- [5] MR Bersi, MJ Collins, E Wilson, and JD Humphrey. Disparate changes in the mechanical properties of murine carotid arteries and aorta in response to chronic infusion of angiotensinii. *International journal of advances in engineering sciences and applied mathematics*, 4(4):228–240, 2012.
- [6] Aroj Bhattarai, Ralf Frotscher, M-C Sora, and Manfred Staat. A 3d finite element model of the female pelvic floor for the reconstruction of urinary incontinence. 2014.
- [7] Stephanie LK Bowers, Thomas K Borg, and Troy A Baudino. The dynamics of fibroblast–myocyte–capillary interactions in the heart. *Annals of the New York Academy of Sciences*, 1188:143, 2010.
- [8] AJ Brady. Passive stiffness of rat cardiac myocytes. *Journal of biomechanical engineering*, 1984.
- [9] Valentine Brussee, GuiFang Guo, YingYing Dong, Chu Cheng, José A Martinez, Darrell Smith, Gordon W Glazner, Paul Fernyhough, and Douglas W Zochodne. Distal degenerative sensory neuropathy in a long-term type 2 diabetes rat model. *Diabetes*, 57(6):1664–1673, 2008.
- [10] Grégory Chagnon, Marie Rebouah, and Denis Favier. Hyperelastic energy densities for soft biological tissues: a review. *Journal of Elasticity*, 120(2):129–160, 2015.

- [11] Xiangfei Chai, Marcel van Herk, Jeroen B van de Kamer, Maarten CCM Hulshof, Peter Remeijer, Heidi T Lotz, and Arjan Bel. Finite element based bladder modeling for imageguided radiotherapy of bladder cancer. *Medical physics*, 38(1):142–150, 2011.
- [12] Sheng Chen, Aisling Ní Annaidh, and Sara Roccabianca. A microstructurally inspired constitutive model for skin mechanics. *Biomechanics and Modeling in Mechanobiology*, 19(1):275–289, 2020.
- [13] Zhuo-Wei Chen, Pierre Joli, Zhi-Qiang Feng, Mehdi Rahim, Nicolas Pirró, and Marc-Emmanuel Bellemare. Female patient-specific finite element modeling of pelvic organ prolapse (pop). *Journal of biomechanics*, 48(2):238–245, 2015.
- [14] Fangzhou Cheng, Lori A Birder, F Aura Kullmann, Jack Hornsby, Paul N Watton, Simon Watkins, Mark Thompson, and Anne M Robertson. Layer-dependent role of collagen recruitment during loading of the rat bladder wall. *Biomechanics and modeling in mechanobiology*, 17(2):403–417, 2018.
- [15] Shaokoon Cheng, Elizabeth C Clarke, and Lynne E Bilston. The effects of preconditioning strain on measured tissue properties. *Journal of biomechanics*, 42(9):1360–1362, 2009.
- [16] George J Christ, Yi Hsieh, Weixin Zhao, Gregory Schenk, Karicheti Venkateswarlu, HONG-ZHAN WANG, Moses T Tar, and Arnold Melman. Effects of streptozotocin-induced diabetes on bladder and erectile (dys) function in the same rat in vivo. *BJU international*, 97(5):1076–1082, 2006.
- [17] Cheng-Jen Chuong and Yuan-Cheng Fung. *Residual stress in arteries*, pages 117–129. Springer, 1986.
- [18] Centers for Disease Control and Prevention. National diabetes statistics report, 2017. *Atlanta, GA: Centers for Disease Control and Prevention, US Department of Health and Human Services*, 20, 2017.
- [19] R Cortivo, F Pagano, G Passerini, G Abatangelo, and I Castellani. Elastin and collagen in the normal and obstructed urinary bladder. *British Journal of Urology*, 53(2):134–137, 1981.
- [20] Kevin D Costa, Jeffrey W Holmes, and Andrew D McCulloch. Modelling cardiac mechanical properties in three dimensions. *Philosophical transactions of the Royal Society of London. Series A: Mathematical, physical and engineering sciences*, 359(1783):1233–1250, 2001.
- [21] Kevin D Costa, Karen May-Newman, Dyan Farr, Walter G O'Dell, Andrew D McCulloch, and Jeffrey H Omens. Three-dimensional residual strain in midanterior canine left ventricle. *American Journal of Physiology-Heart and Circulatory Physiology*, 273(4):H1968–H1976, 1997.
- [22] Firouz Daneshgari, Guiming Liu, and Peter B Imrey. Time dependent changes in diabetic cystopathy in rats include compensated and decompensated bladder function. *The Journal of urology*, 176(1):380–386, 2006.

- [23] Pieter P de Tombe and Henk EDJ ter Keurs. Cardiac muscle mechanics: sarcomere length matters. *Journal of molecular and cellular cardiology*, 91:148–150, 2016.
- [24] A Delfino, N Stergiopulos, JE Moore Jr, and J-J Meister. Residual strain effects on the stress field in a thick wall finite element model of the human carotid bifurcation. *Journal of biomechanics*, 30(8):777–786, 1997.
- [25] Linda L Demer and FC Yin. Passive biaxial mechanical properties of isolated canine myocardium. *The Journal of physiology*, 339(1):615–630, 1983.
- [26] Hilmi Demiray. A note on the elasticity of soft biological tissues. *Journal of biomechanics*, 5(3):309–311, 1972.
- [27] Hilmi Demiray, Hans W Weizsäcker, Karin Pascale, and HüsnüA Erbay. A stress-strain relation for a rat abdominal aorta. *Journal of biomechanics*, 21(5):369–374, 1988.
- [28] Franz Duca, Caroline Zotter-Tufaro, Andreas A Kammerlander, Stefan Aschauer, Christina Binder, Julia Mascherbauer, and Diana Bonderman. Gender-related differences in heart failure with preserved ejection fraction. *Scientific reports*, 8(1):1–9, 2018.
- [29] Krista M Durney, Ricky Martinez, and Hai-Chao Han. The effect of collagenase on arterial opening angle. In 2009 IEEE 35th Annual Northeast Bioengineering Conference, pages 1–2. IEEE, 2009.
- [30] Alexander E Ehret and Mikhail Itskov. Modeling of anisotropic softening phenomena: application to soft biological tissues. *International Journal of Plasticity*, 25(5):901–919, 2009.
- [31] JEFF L Emery, JEFFREY H Omens, and ANDREW D McCULLOCH. Biaxial mechanics of the passively overstretched left ventricle. *American Journal of Physiology-Heart and Circulatory Physiology*, 272(5):H2299–H2305, 1997.
- [32] Roxanne Fernandes, Hannah Garver, Jack R Harkema, James J Galligan, Gregory D Fink, and Hui Xu. Sex differences in renal inflammation and injury in high-fat diet–fed dahl salt-sensitive rats. *Hypertension*, 72(5):e43–e52, 2018.
- [33] MP Fitzgerald, U Stablein, and L Brubaker. Urinary habits among asymptomatic women. *American journal of obstetrics and gynecology*, 187(5):1384–1388, 2002.
- [34] Luigi Fontana, J Christopher Eagon, Maria E Trujillo, Philipp E Scherer, and Samuel Klein. Visceral fat adipokine secretion is associated with systemic inflammation in obese humans. *Diabetes*, 56(4):1010–1013, 2007.
- [35] John R Fozard, Hans-Jürgen Pfannkuche, and Henk-Jan Schuurman. Mast cell degranulation following adenosine a3 receptor activation in rats. *European journal of pharmacology*, 298(3):293–297, 1996.
- [36] C Frimodt-Møller and S Mortensen. Treatment of diabetic cystopathy. *Annals of Internal Medicine*, 92(2.2):327–328, 1980.

- [37] CH Fry. Role of the bladder in storage and micturition. *Surgery (Oxford)*, 23(3):93–96, 2005.
- [38] H Gao, WG Li, L Cai, C Berry, and XY Luo. Parameter estimation in a holzapfel–ogden law for healthy myocardium. *Journal of engineering mathematics*, 95(1):231–248, 2015.
- [39] Gregory Gasbarro, Dan Li Lin, Drina Vurbic, Amanda Quisno, Bruce Kinley, Firouz Daneshgari, and Margot S Damaser. Voiding function in obese and type 2 diabetic female rats. *American Journal of Physiology-Renal Physiology*, 298(1):F72–F77, 2010.
- [40] T Christian Gasser, Ray W Ogden, and Gerhard A Holzapfel. Hyperelastic modelling of arterial layers with distributed collagen fibre orientations. *Journal of the royal society interface*, 3(6):15–35, 2006.
- [41] Martin Genet, Lik Chuan Lee, Rebecca Nguyen, Henrik Haraldsson, Gabriel Acevedo-Bolton, Zhihong Zhang, Liang Ge, Karen Ordovas, Sebastian Kozerke, and Julius M Guccione. Distribution of normal human left ventricular myofiber stress at end diastole and end systole: a target for in silico design of heart failure treatments. *Journal of applied physiology*, 117(2):142–152, 2014.
- [42] Martin Genet, MK Rausch, Lik Chuan Lee, S Choy, X Zhao, Ghassan S Kassab, Sebastian Kozerke, Julius M Guccione, and Ellen Kuhl. Heterogeneous growth-induced prestrain in the heart. *Journal of biomechanics*, 48(10):2080–2089, 2015.
- [43] Martin Genet, Christian T Stoeck, C Von Deuster, Lik Chuan Lee, and Sebastian Kozerke. Equilibrated warping: Finite element image registration with finite strain equilibrium gap regularization. *Medical image analysis*, 50:1–22, 2018.
- [44] Thomas W Gilbert, Silvia Wognum, Erinn M Joyce, Donald O Freytes, Michael S Sacks, and Stephen F Badylak. Collagen fiber alignment and biaxial mechanical behavior of porcine urinary bladder derived extracellular matrix. *Biomaterials*, 29(36):4775–4782, 2008.
- [45] Ellen E Gillis, Jan M Williams, Michael R Garrett, Jennifer N Mooney, and Jennifer M Sasser. The dahl salt-sensitive rat is a spontaneous model of superimposed preeclampsia. *American Journal of Physiology-Regulatory, Integrative and Comparative Physiology*, 309(1):R62–R70, 2015.
- [46] D Claire Gloeckner, Michael S Sacks, Matthew O Fraser, George T Somogyi, WILLIAM C de GROAT, and Michael B Chancellor. Passive biaxial mechanical properties of the rat bladder wall after spinal cord injury. *The Journal of urology*, 167(5):2247–2252, 2002.
- [47] Mauro Gori, Carolyn SP Lam, Deepak K Gupta, Angela BS Santos, Susan Cheng, Amil M Shah, Brian Claggett, Michael R Zile, Elisabeth Kraigher-Krainer, and Burkert Pieske. Sex-specific cardiovascular structure and function in heart failure with preserved ejection fraction. *European journal of heart failure*, 16(5):535–542, 2014.
- [48] YOSHI GOTO, Masaei Kakizaki, and Naoyoshi Masaki. Production of spontaneous diabetic rats by repetition of selective breeding. *The Tohoku journal of experimental medicine*, 119(1):85–90, 1976.

- [49] Margaret A Gray, Chung-Cheng Wang, Michael S Sacks, Naoki Yoshimura, Michael B Chancellor, and Jiro Nagatomi. Time-dependent alterations of select genes in streptozotocin-induced diabetic rat bladder. *Urology*, 71(6):1214–1219, 2008.
- [50] ANDREW S Greene, Z Yuan Yu, RJ Roman, and AW Cowley Jr. Role of blood volume expansion in dahl rat model of hypertension. *American Journal of Physiology-Heart and Circulatory Physiology*, 258(2):H508–H514, 1990.
- [51] Marissa R Grobbel, Sheikh Mohammad Shavik, Emma Darios, Stephanie W Watts, Lik Chuan Lee, and Sara Roccabianca. Contribution of left ventricular residual stress by myocytes and collagen: existence of inter-constituent mechanical interaction. *Biomechanics and modeling in mechanobiology*, 17(4):985–999, 2018.
- [52] MR Grobbel, LC Lee, SW Watts, GD Fink, and S Roccabianca. Left ventricular geometry, tissue composition, and residual stress in high fat diet dahl-salt sensitive rats. *Experimental Mechanics*, pages 1–11, 2020.
- [53] Julius M Guccione, Andrew D McCulloch, and LK Waldman. Passive material properties of intact ventricular myocardium determined from a cylindrical model. *Journal of biomechanical engineering*, 1991.
- [54] ROGER J Hajjar, JOANNE S Ingwall, and JUDITH K Gwathmey. Mechanism of action of 2, 3-butanedione monoxime on contracture during metabolic inhibition. *American Journal of Physiology-Heart and Circulatory Physiology*, 267(1):H100–H108, 1994.
- [55] David M Hamby. A review of techniques for parameter sensitivity analysis of environmental models. *Environmental monitoring and assessment*, 32(2):135–154, 1994.
- [56] Hai-Chao Han and Yuan-Cheng Fung. Longitudinal strain of canine and porcine aortas. *Journal of biomechanics*, 28(5):637–641, 1995.
- [57] Peter J Hanley, Alistair A Young, Ian J LeGrice, Stephen G Edgar, and Denis S Loiselle. 3-dimensional configuration of perimysial collagen fibres in rat cardiac muscle at resting and extended sarcomere lengths. *The Journal of physiology*, 517(Pt 3):831, 1999.
- [58] Paul A Heidenreich, Justin G Trogdon, Olga A Khavjou, Javed Butler, Kathleen Dracup, Michael D Ezekowitz, Eric Andrew Finkelstein, Yuling Hong, S Claiborne Johnston, Amit Khera, et al. Forecasting the future of cardiovascular disease in the united states: a policy statement from the american heart association. *Circulation*, 123(8):933–944, 2011.
- [59] OTTO M Hess, JOERG Grimm, and HANS P Krayenbuehl. Diastolic simple elastic and viscoelastic properties of the left ventricle in man. *Circulation*, 59(6):1178–1187, 1979.
- [60] SO Hietala and B Winblad. Vascular changes in the urinary bladder wall after irradiation. *International Urology and Nephrology*, 8(2):121–128, 1976.
- [61] GA Holzapfel, G Sommer, C Gasser, and P Regitnig. Determination of the layer-specific mechanical properties of human coronary arteries with intimal thickening, and related constitutive modelling. *Am J Physiol Heart Circ Physiol*, 289:H2048–H2058, 2005.

- [62] Gerhard A Holzapfel, Thomas C Gasser, and Ray W Ogden. A new constitutive framework for arterial wall mechanics and a comparative study of material models. *Journal of elasticity and the physical science of solids*, 61(1-3):1–48, 2000.
- [63] Gerhard A Holzapfel and Ray W Ogden. Constitutive modelling of passive myocardium: a structurally based framework for material characterization. *Philosophical Transactions of the Royal Society A: Mathematical, Physical and Engineering Sciences*, 367(1902):3445–3475, 2009.
- [64] A Horowitz, Y Lanir, FCP Yin, M Perl, I Sheinman, and RK Strumpf. Structural three-dimensional constitutive law for the passive myocardium. *Journal of biomechanical engineering*, 1988.
- [65] Sayyed Mohsen Hosseini, Wouter Wilson, Keita Ito, and Corrinus C van Donkelaar. How preconditioning affects the measurement of poro-viscoelastic mechanical properties in biological tissues. *Biomechanics and modeling in mechanobiology*, 13(3):503–513, 2014.
- [66] Jay D Humphrey. Continuum biomechanics of soft biological tissues. *Proceedings of the Royal Society of London. Series A: Mathematical, Physical and Engineering Sciences*, 459(2029):3–46, 2003.
- [67] Jay D Humphrey. Cardiovascular solid mechanics: cells, tissues, and organs. Springer Science & Business Media, 2013.
- [68] Jana Jaal and Wolfgang Dörr. Radiation-induced damage to mouse urothelial barrier. *Radiotherapy and Oncology*, 80(2):250–256, 2006.
- [69] Jana Jaal and Wolfgang Dörr. Radiation induced inflammatory changes in the mouse bladder: the role of cyclooxygenase-2. *The Journal of urology*, 175(4):1529–1533, 2006.
- [70] Jana Jaal and Wolfgang Dörr. Radiation induced late damage to the barrier function of small blood vessels in mouse bladder. *The Journal of urology*, 176(6):2696–2700, 2006.
- [71] Steven A Kaplan and Jerry G Blaivas. Diabetic cystopathy. *Journal of Diabetic Complications*, 2(3):133–139, 1988.
- [72] Steven A Kaplan, Alexis E Te, Jerry G Blaivas, and Edward J McGuire. Urodynamic findings in patients with diabetic cystopathy. *The Journal of urology*, 153(2):342–344, 1995.
- [73] Derek M Kendig, Hillevi K Ets, and Robert S Moreland. Effect of type ii diabetes on male rat bladder contractility. *American Journal of Physiology-Renal Physiology*, 310(9):F909–F922, 2016.
- [74] Mieke MJF Koenders, Lanti Yang, Ronnie G Wismans, Kees O van der Werf, Dieter P Reinhardt, Willeke Daamen, Martin L Bennink, Pieter J Dijkstra, Toin H van Kuppevelt, and Jan Feijen. Microscale mechanical properties of single elastic fibers: the role of fibrillin–microfibrils. *Biomaterials*, 30(13):2425–2432, 2009.

- [75] Markus Kohler, Christian Michel, and Arthur Zimmermann. Histological changes after fractionated whole or partial irradiation of the rabbit urinary bladder. *Acta Oncologica*, 34(2):199–204, 1995.
- [76] M Kraft, Y Oussoren, FA Stewart, W Dörr, and S Schultz-Hector. Radiation-induced changes in transforming growth factor β and collagen expression in the murine bladder wall and its correlation with bladder function. *Radiation research*, 146(6):619–627, 1996.
- [77] Martina Kruger, Sebastian Kotter, Anika Grutzner, Patrick Lang, Christian Andresen, Margaret M Redfield, Elke Butt, Cris G Dos Remedios, and Wolfgang A Linke. Protein kinase g modulates human myocardial passive stiffness by phosphorylation of the titin springs. *Circulation research*, 104(1):87–94, 2009.
- [78] Géry Lamblin, Olivier Mayeur, Géraldine Giraudet, Estelle Jean dit Gautier, Gautier Chene, Mathias Brieu, Chrystèle Rubod, and Michel Cosson. Pathophysiological aspects of cystocele with a 3d finite elements model. *Archives of gynecology and obstetrics*, 294(5):983–989, 2016.
- [79] Jerilyn M Latini, Elizabeth Mueller, Matthew M Lux, Mary Pat Fitzgerald, and Karl J Kreder. Voiding frequency in a sample of asymptomatic american men. *The Journal of urology*, 172(3):980–984, 2004.
- [80] Lik Chuan Lee, Jonathan F Wenk, Liang Zhong, Doron Klepach, Zhihong Zhang, Liang Ge, Mark B Ratcliffe, Tarek I Zohdi, Edward Hsu, and Jose L Navia. Analysis of patient-specific surgical ventricular restoration: importance of an ellipsoidal left ventricular geometry for diastolic and systolic function. *Journal of applied physiology*, 115(1):136–144, 2013.
- [81] Matthew T Lewis, Jonathan D Kasper, Jason N Bazil, Jefferson C Frisbee, and Robert W Wiseman. Skeletal muscle energetics are compromised only during high-intensity contractions in the goto-kakizaki rat model of type 2 diabetes. *American Journal of Physiology-Regulatory, Integrative and Comparative Physiology*, 317(2):R356–R368, 2019.
- [82] Matthew T Lewis, Heidi L Lujan, Anne Tonson, Robert W Wiseman, and Stephen E DiCarlo. Obesity and inactivity, not hyperglycemia, cause exercise intolerance in individuals with type 2 diabetes: Solving the obesity and inactivity versus hyperglycemia causality dilemma. *Medical Hypotheses*, 123:110–114, 2019.
- [83] Guiming Liu and Firouz Daneshgari. Alterations in neurogenically mediated contractile responses of urinary bladder in rats with diabetes. *American Journal of Physiology-Renal Physiology*, 288(6):F1220–F1226, 2005.
- [84] Guiming Liu and Firouz Daneshgari. Temporal diabetes-and diuresis-induced remodeling of the urinary bladder in the rat. *American Journal of Physiology-Regulatory, Integrative and Comparative Physiology*, 291(3):R837–R843, 2006.
- [85] SQ Liu and YC Fung. Relationship between hypertension, hypertrophy, and opening angle of zero-stress state of arteries following aortic constriction. *Journal of biomechanical engineering*, 1989.

- [86] ES Lukacz, C Sampselle, M Gray, S Macdiarmid, M Rosenberg, P Ellsworth, and MH Palmer. A healthy bladder: a consensus statement. *International journal of clinical practice*, 65(10):1026–1036, 2011.
- [87] FINN LUNDBECK, KARSTEN NIELSEN, and FIONA STEWART. Late changes in the normal mouse bladder after irradiation alone or in combination with cis-ddp or cyclophosphamide, assessed by stereological analysis. *APMIS*, 101(1-6):275–280, 1993.
- [88] Guido Macchiarelli, O Ohtani, Stefania A Nottola, T Stallone, A Camboni, IM Prado, and PM Motta. A micro-anatomical model of the distribution of myocardial endomysial collagen. *Histology and histopathology*, 2002.
- [89] Deidre A MacKenna, Jeffrey H Omens, AD McCulloch, and James W Covell. Contribution of collagen matrix to passive left ventricular mechanics in isolated rat hearts. *American Journal of Physiology-Heart and Circulatory Physiology*, 266(3):H1007–H1018, 1994.
- [90] Megan L McCain, Hyungsuk Lee, Yvonne Aratyn-Schaus, André G Kléber, and Kevin Kit Parker. Cooperative coupling of cell-matrix and cell-cell adhesions in cardiac muscle. *Proceedings of the National Academy of Sciences*, 109(25):9881–9886, 2012.
- [91] Andrew D McCulloch. Cardiac biomechanics. *The Biomedical Engineering Handbook*, 2:503–512, 1995.
- [92] IVAN Medugorac and RUTHARD Jacob. Characterisation of left ventricular collagen in the rat. *Cardiovascular research*, 17(1):15–21, 1983.
- [93] Arnold Melman, Elena Zotova, Mimi Kim, Joseph Arezzo, Kelvin Davies, Michael DiSanto, and Moses Tar. Longitudinal studies of time-dependent changes in both bladder and erectile function after streptozotocin-induced diabetes in fischer 344 male rats. *BJU international*, 104(9):1292–1300, 2009.
- [94] Martin Metz, Michele A Grimbaldeston, Susumu Nakae, Adrian M Piliponsky, Mindy Tsai, and Stephen J Galli. Mast cells in the promotion and limitation of chronic inflammation. *Immunological reviews*, 217(1):304–328, 2007.
- [95] Louis A Mulieri, Gerd Hasenfuss, Frank Ittleman, Edward M Blanchard, and Norman R Alpert. Protection of human left ventricular myocardium from cutting injury with 2, 3-butanedione monoxime. *Circulation Research*, 65(5):1441–1449, 1989.
- [96] Jiro Nagatomi, D Claire Gloeckner, Michael B Chancellor, William C Degroat, and Michael S Sacks. Changes in the biaxial viscoelastic response of the urinary bladder following spinal cord injury. *Annals of biomedical engineering*, 32(10):1409–1419, 2004.
- [97] Jiro Nagatomi, Kevin K Toosi, Michael B Chancellor, and Michael S Sacks. Contribution of the extracellular matrix to the viscoelastic behavior of the urinary bladder wall. *Biomechanics and modeling in mechanobiology*, 7(5):395–404, 2008.
- [98] AN Natali, AL Audenino, W Artibani, CG Fontanella, EL Carniel, and EM Zanetti. Bladder tissue biomechanical behavior: experimental tests and constitutive formulation. *Journal of Biomechanics*, 48(12):3088–3096, 2015.

- [99] Erez Nevo and Yoram Lanir. The effect of residual strain on the diastolic function of the left ventricle as predicted by a structural model. *Journal of biomechanics*, 27(12):1433–1446, 1994.
- [100] Amir Nikou, Shauna M Dorsey, Jeremy R McGarvey, Joseph H Gorman, Jason A Burdick, James J Pilla, Robert C Gorman, and Jonathan F Wenk. Computational modeling of healthy myocardium in diastole. *Annals of biomedical engineering*, 44(4):980–992, 2016.
- [101] Jayabalan Nirmal, Pradeep Tyagi, Yao-Chi Chuang, Wei-Chia Lee, Naoki Yoshimura, Chao-Cheng Huang, Bharathi Rajaganapathy, and Michael B Chancellor. Functional and molecular characterization of hyposensitive underactive bladder tissue and urine in streptozotocin-induced diabetic rat. *PloS one*, 9(7), 2014.
- [102] A Afşin Oktay and Sanjiv J Shah. Current perspectives on systemic hypertension in heart failure with preserved ejection fraction. *Current cardiology reports*, 16(12):545, 2014.
- [103] Jeffrey H Omens and Yuan-Cheng Fung. Residual strain in rat left ventricle. *Circulation research*, 66(1):37–45, 1990.
- [104] Jeffrey H Omens, Deidre A MacKenna, and Andrew D McCulloch. Measurement of strain and analysis of stress in resting rat left ventricular myocardium. *Journal of biomechanics*, 26(6):665–676, 1993.
- [105] Jeffrey H Omens, David E Milkes, and James W Covell. Effects of pressure overload on the passive mechanics of the rat left ventricle. *Annals of biomedical engineering*, 23(2):152–163, 1995.
- [106] Jeffrey H Omens, Timothy R Miller, and James W Covell. Relationship between passive tissue strain and collagen uncoiling during healing of infarcted myocardium. *Cardiovascular research*, 33(2):351–358, 1997.
- [107] Jeffrey H Omens, Edward K Rodriguez, and Andrew D McCulloch. Transmural changes in stress-free myocyte morphology during pressure overload hypertrophy in the rat. *Journal of molecular and cellular cardiology*, 28(9):1975–1983, 1996.
- [108] JH Omens, AD McCulloch, and JC Criscione. Complex distributions of residual stress and strain in the mouse left ventricle: experimental and theoretical models. *Biomechanics and modeling in mechanobiology*, 1(4):267–277, 2003.
- [109] JH Omens, SM Vaplon, B Fazeli, and AD McCulloch. Left ventricular geometric remodeling and residual stress in the rat heart. *Journal of biomechanical engineering*, 1998.
- [110] Harald C Ott, Thomas S Matthiesen, Saik-Kia Goh, Lauren D Black, Stefan M Kren, Theoden I Netoff, and Doris A Taylor. Perfusion-decellularized matrix: using nature's platform to engineer a bioartificial heart. *Nature medicine*, 14(2):213–221, 2008.
- [111] Jehill D Parikh, Kieren G Hollingsworth, Dorothy Wallace, Andrew M Blamire, and Guy A MacGowan. Left ventricular functional, structural and energetic effects of normal aging: Comparison with hypertension. *PloS one*, 12(5):e0177404, 2017.

- [112] Richard G Peterson, Walter N Shaw, Mary-Ann Neel, Leah A Little, and J Eichberg. Zucker diabetic fatty rat as a model for non-insulin-dependent diabetes mellitus. *Ilar Journal*, 32(3):16–19, 1990.
- [113] QC Pham, FCPCP Vincent, P Clarysse, P Croisille, and IE Magnin. A fem-based deformable model for the 3d segmentation and tracking of the heart in cardiac mri. In ISPA 2001. Proceedings of the 2nd International Symposium on Image and Signal Processing and Analysis. In conjunction with 23rd International Conference on Information Technology Interfaces (IEEE Cat., pages 250–254. IEEE, 2001.
- [114] Christian Pinna, Rossella Zanardo, and Lina Puglisi. Prostaglandin-release impairment in the bladder epithelium of streptozotocin-induced diabetic rats. *European journal of pharmacology*, 388(3):267–273, 2000.
- [115] M Pisarska and S Sajdak. Lower urinary tract function after postoperative radiotherapy in the treatment of cervical cancer. *European journal of gynaecological oncology*, 24(6):490–494, 2003.
- [116] DA Pitre, T Ma, LJ Wallace, and JA Bauer. Time-dependent urinary bladder remodeling in the streptozotocin-induces diabetic rat model. *Acta diabetologica*, 39(1):23–27, 2002.
- [117] ML Raghavan and David A Vorp. Toward a biomechanical tool to evaluate rupture potential of abdominal aortic aneurysm: identification of a finite strain constitutive model and evaluation of its applicability. *Journal of biomechanics*, 33(4):475–482, 2000.
- [118] Lindsey A Ramirez and Jennifer C Sullivan. Sex differences in hypertension: where we have been and where we are going. *American journal of hypertension*, 31(12):1247–1254, 2018.
- [119] Lindsey A Ramirez and Jennifer C Sullivan. Sex differences in hypertension: where we have been and where we are going. *American journal of hypertension*, 31(12):1247–1254, 2018.
- [120] J SCOTT Rankin, CARL E Arentzen, PHILIP A McHale, DAVID Ling, and ROBERT W Anderson. Viscoelastic properties of the diastolic left ventricle in the conscious dog. *Circulation research*, 41(1):37–45, 1977.
- [121] Kavitha N Rao and Melissa A Brown. Mast cells: multifaceted immune cells with diverse roles in health and disease. *Annals of the New York Academy of Sciences*, 1143(1):83–104, 2008.
- [122] Claude H Regnier, Herbert Kolsky, Peter D Richardson, Gamal M Ghoniem, and Jacques G Susset. The elastic behavior of the urinary bladder for large deformations. *Journal of biomechanics*, 16(11):915–922, 1983.
- [123] Devinder Rehal, Xiaomei Guo, Xiao Lu, and Ghassan S Kassab. Duration of no-load state affects opening angle of porcine coronary arteries. *American Journal of Physiology-Heart and Circulatory Physiology*, 290(5):H1871–H1878, 2006.

- [124] Diaa EE Rizk, Rengasamy K Padmanabhan, Saeed Tariq, Mohamed Shafiullah, and Ijaz Ahmed. Ultra-structural morphological abnormalities of the urinary bladder in streptozotocin-induced diabetic female rats. *International Urogynecology Journal*, 17(2):143–154, 2006.
- [125] EDWARD K Rodriguez, JEFFREY H Omens, LK Waldman, and AD McCulloch. Effect of residual stress on transmural sarcomere length distributions in rat left ventricle. *American Journal of Physiology-Heart and Circulatory Physiology*, 264(4):H1048–H1056, 1993.
- [126] Marcos A Rossi. Pathologic fibrosis and connective tissue matrix in left ventricular hypertrophy due to chronic arterial hypertension in humans. *Journal of hypertension*, 16(7):1031–1041, 1998.
- [127] Hannah Ruetten, Kyle A Wegner, Helen L Zhang, Peiqing Wang, Jaskiran Sandhu, Simran Sandhu, Brett Mueller, Zunyi Wang, Jill Macoska, Richard E Peterson, et al. Factors driving unique urination phenotypes of male and female 9-week-old c57bl/6j mice. *bioRxiv*, page 641167, 2019.
- [128] Michael S Sacks. Biaxial mechanical evaluation of planar biological materials. *Journal of elasticity and the physical science of solids*, 61(1):199–246, 2000.
- [129] Yusuke Sano, Shogo Ito, Mamoru Yoneda, Kai Nagasawa, Natsumi Matsuura, Yuichiro Yamada, Ayako Uchinaka, Yasuko K Bando, Toyoaki Murohara, and Kohzo Nagata. Effects of various types of anesthesia on hemodynamics, cardiac function, and glucose and lipid metabolism in rats. *American Journal of Physiology-Heart and Circulatory Physiology*, 311(6):H1360–H1366, 2016.
- [130] Caroline A Schneider, Wayne S Rasband, and Kevin W Eliceiri. Nih image to imagej: 25 years of image analysis. *Nature methods*, 9(7):671–675, 2012.
- [131] Zhilei L Shen, Mohammad Reza Dodge, Harold Kahn, Roberto Ballarini, and Steven J Eppell. Stress-strain experiments on individual collagen fibrils. *Biophysical journal*, 95(8):3956–3963, 2008.
- [132] Masakazu Shiota and Richard L Printz. *Diabetes in Zucker diabetic fatty rat*, pages 103–123. Springer, 2012.
- [133] Shaun G Smit and Chris F Heyns. Management of radiation cystitis. *Nature Reviews Urology*, 7(4):206, 2010.
- [134] John P Sundberg, Douglas Taylor, Gwendolen Lorch, Jim Miller, Kathleen A Silva, Beth A Sundberg, Derry Roopenian, Leonard Sperling, David Ong, Lloyd E King, et al. Primary follicular dystrophy with scarring dermatitis in c57bl/6 mouse substrains resembles central centrifugal cicatricial alopecia in humans. *Veterinary pathology*, 48(2):513–524, 2011.
- [135] LA Taber and S Chabert. Theoretical and experimental study of growth and remodeling in the developing heart. *Biomechanics and modeling in mechanobiology*, 1(1):29–43, 2002.

- [136] Larry A Taber, Norman Hu, Tomas Pexieder, Edward B Clark, and BB Keller. Residual strain in the ventricle of the stage 16-24 chick embryo. *Circulation research*, 72(2):455–462, 1993.
- [137] Marty C Tam, Ran Lee, Thomas M Cascino, Matthew C Konerman, and Scott L Hummel. Current perspectives on systemic hypertension in heart failure with preserved ejection fraction. *Current hypertension reports*, 19(2):12, 2017.
- [138] Teuvo LJ Tammela, Robert E Leggett, Robert M Levin, and Penelope A Longhurst. Temporal changes in micturition and bladder contractility after sucrose diuresis and streptozotocin-induced diabetes mellitus in rats. *The Journal of urology*, 153(6):2014–2021, 1995.
- [139] Loon Yee Louis Teo, Laura Lihua Chan, and Carolyn Su Ping Lam. Heart failure with preserved ejection fraction in hypertension. *Current opinion in cardiology*, 31(4):410–416, 2016.
- [140] Pin Tong and Yuang-Cheng Fung. The stress-strain relationship for the skin. *Journal of Biomechanics*, 9(10):649–657, 1976.
- [141] Kevin K Toosi, Jiro Nagatomi, Michael B Chancellor, and Michael S Sacks. The effects of long-term spinal cord injury on mechanical properties of the rat urinary bladder. *Annals of biomedical engineering*, 36(9):1470–1480, 2008.
- [142] Ron van Mastrigt, BLRA Coolsaet, and WA Van Duyl. Passive properties of the urinary bladder in the collection phase. *Medical and Biological Engineering and Computing*, 16(5):471–482, 1978.
- [143] I Vlastelica, D Veljkovic, V Rankovic, B Stojanovic, M Rosic, and M Kojic. Modeling of urinary bladder deformation within passive and active regimes. *Journ. of the Serbian Society for Computational Mechanics*, 1(1):129–134, 2007.
- [144] Chung Cheng Wang, Jiro Nagatomi, K Khashayar Toosi, Naoki Yoshimura, Jui Hsiang Hsieh, Michael B Chancellor, and Michael S Sacks. Diabetes-induced alternations in biomechanical properties of urinary bladder wall in rats. *Urology*, 73(4):911–915, 2009.
- [145] HM Wang, H Gao, XY Luo, C Berry, BE Griffith, RW Ogden, and TJ Wang. Structure-based finite strain modelling of the human left ventricle in diastole. *International journal for numerical methods in biomedical engineering*, 29(1):83–103, 2013.
- [146] Zhu Wang, Yuexin Yang, Xuesong Xiang, Yuming Zhu, Jianhua Men, and Mei He. Estimation of the normal range of blood glucose in rats. *Wei sheng yan jiu= Journal of hygiene research*, 39(2):133–142, 2010.
- [147] Karl T Weber. Cardiac interstitium in health and disease: the fibrillar collagen network. *Journal of the American College of Cardiology*, 13(7):1637–1652, 1989.
- [148] Silvia Wognum, Claudio E Lagoa, Jiro Nagatomi, Michael S Sacks, and Yoram Vodovotz. An exploratory pathways analysis of temporal changes induced by spinal cord injury in the rat bladder wall: insights on remodeling and inflammation. *PloS one*, 4(6), 2009.

- [149] Silvia Wognum, David E Schmidt, and Michael S Sacks. On the mechanical role of de novo synthesized elastin in the urinary bladder wall. *Journal of biomechanical engineering*, 131(10), 2009.
- [150] Frank CP Yin, Robert K Strumpf, Paul H Chew, and Scott L Zeger. Quantification of the mechanical properties of noncontracting canine myocardium under simultaneous biaxial loading. *Journal of biomechanics*, 20(6):577–589, 1987.
- [151] Z Yuan, Z Tang, C He, and W Tang. Diabetic cystopathy: A review. *Journal of diabetes*, 7(4):442, 2015.
- [152] Haiyang Zhang, Xuefeng Qiu, Alan W Shindel, Hongxiu Ning, Ludovic Ferretti, Xunbo Jin, Guiting Lin, Ching-Shwun Lin, and Tom F Lue. Adipose tissue-derived stem cells ameliorate diabetic bladder dysfunction in a type ii diabetic rat model. *Stem cells and development*, 21(9):1391–1400, 2012.
- [153] W Zhang, X Guo, and GS Kassab. A generalized maxwell model for creep behavior of artery opening angle. *Journal of biomechanical engineering*, 130(5), 2008.
- [154] Hua Zou, Ce Xi, Xiaodan Zhao, Angela S Koh, Fei Gao, Yi Su, Ru-San Tan, John Allen, Lik Chuan Lee, and Martin Genet. Quantification of biventricular strains in heart failure with preserved ejection fraction patient using hyperelastic warping method. *Frontiers in Physiology*, 9:1295, 2018.
- [155] Fouad A Zouein, Lisandra E de Castro Brás, Danielle V Da Costa, Merry L Lindsey, Mazen Kurdi, and George W Booz. Heart failure with preserved ejection fraction: emerging drug strategies. *Journal of cardiovascular pharmacology*, 62(1):13, 2013.
- [156] Bernadette MM Zwaans, Sarah Krueger, Sarah N Bartolone, Michael B Chancellor, Brian Marples, and Laura E Lamb. Modeling of chronic radiation-induced cystitis in mice. *Advances in radiation oncology*, 1(4):333–343, 2016.
- [157] Bernadette MM Zwaans, Heinz E Nicolai, Michael B Chancellor, and Laura E Lamb. Prostate cancer survivors with symptoms of radiation cystitis have elevated fibrotic and vascular proteins in urine. *PloS one*, 15(10):e0241388, 2020.
- [158] Bernadette MM Zwaans, Heinz G Nicolai, Michael B Chancellor, and Laura E Lamb. Challenges and opportunities in radiation-induced hemorrhagic cystitis. *Reviews in urology*, 18(2):57, 2016.
- [159] Bernadette MM Zwaans, Kyle A Wegner, Sarah N Bartolone, Chad M Vezina, Michael B Chancellor, and Laura E Lamb. Radiation cystitis modeling: A comparative study of bladder fibrosis radio-sensitivity in c57bl/6, c3h, and balb/c mice. *Physiological Reports*, 8(4):e14377, 2020.